The Dissertation Committee for Yongxi Hou Certifies that this is the approved version of the following dissertation:

Particle Image Velocimetry Study of Shock Induced Turbulent Boundary Layer Separation

Committee:

Clemens, Noel T., Supervisor

Bogard, David G.

Dolling, David S.

Raja, Laxminarayan L.

Varghese, Philip L.

Particle Image Velocimetry Study of Shock-Induced Turbulent Boundary Layer Separation

by

Yongxi Hou, B.S.; M.S.

Dissertation

Presented to the Faculty of the Graduate School of
The University of Texas at Austin
in Partial Fulfillment
of the Requirements
for the Degree of

Doctor of Philosophy

The University of Texas at Austin
December 2003

Acknowledgements

This work would never have been possible without the advice, help, and encouragement of many talented individuals. I, as a foreign-student, who has needed to learn and adapt to many things, would like to thank my advisor, Dr. Noel Clemens, who patiently supported me in every aspect through every success and disaster. I would like to thank Dr. David Dolling, who taught me a lot, both in the classroom and through our research discussions. I would also like to thank Drs. David Bogard, Laxminarayan Raja, and Philip Varghese, for serving on my dissertation committee and challenging me through their classes; Dr. M. Mungal for the use of the Matlab-based PIV processing software used in this work; Mrs. Donna Soward, for her invaluable help with ordering parts and equipment; my fellow graduate student Pablo Bueno, who was directly involved and helped a lot in the current study; my other fellow graduate students and colleagues, Roderick Austin, Isaac Boxx, Cherian Idicheria, Michael Ryan, Dr. Michael S. Tsurikov, Dr. Haldun Unalmis, Guanghua Wang, and Mr. Edward Zihlman, for many intellectual and practical contributions to this work. This work was sponsored by the Army Research Office under the supervision of Dr. Tom Doligalski and I gratefully acknowledge this financial support.

Particle Image Velocimetry Study of Shock-Induced Turbulent Boundary Layer Separation

Publication No._____________

Yongxi Hou, Ph.D.
The University of Texas at Austin, 2003

Supervisor: Noel T. Clemens

An experimental study was conducted to investigate the characteristics of a Mach 2 shock wave / boundary layer interaction, by using particle image velocimetry (PIV). The objective was to investigate how the global flow structure is related to the shock-foot dynamics. A major component of this work was the development of a new multi-camera, multi-laser PIV system, which enables the acquisition of wide-field and time-sequenced velocity fields. The wide-field images are obtained by placing four cameras side-by-side giving an effective resolution of 4k×1k pixels. Four-image time sequences can be acquired where the time between frames is 30 to 200 μs. The PIV system was used to characterize the upstream Mach 2 boundary layer. The measured mean and RMS velocity profiles agreed well with previous measurements in compressible boundary layers and this provided important validation of the PIV system.

The wide-field PIV system was used to image the entire interaction, spanning the upstream boundary layer, intermittent region, separated flow and the reattachment region on the ramp face. The separation shock wave location inferred from the PIV images agreed well with the shock-foot position inferred from the pressure data. The instantaneous vector fields reveal that boundary layer separation is not immediately induced by the shock foot, but sometimes develops substantially farther downstream. Significant reverse-flow velocities are seen in the instantaneous images, but on average no reverse-flow was observed.

The global structure of the interaction was found to depend strongly on the location of the separation shock foot. Ensemble averages, conditioned upon the shock-foot position, showed that when the shock is upstream, the scale of the separated flow, the velocity fluctuations, and the domain of perturbed flow, are all substantially larger than when the shock-foot is downstream. Perhaps most importantly, the conditional upstream boundary layer profiles, conditioned on the shock position, showed that the boundary layer is thicker when the shock is upstream and *vice versa*. Furthermore, the conditional measurements confirmed the results of a previous study that reported a correlation between velocity fluctuations in the upstream boundary layer and shock foot motion. A preliminary study was used to test the hypothesis that acceleration fluctuations in the upstream boundary layer correlate with shock foot motion. These results showed no meaningful relationship between upstream acceleration with the shock motion, but given certain limitations of the experiment this conclusion cannot be considered definitive.

Table of Contents

List of Tables

List of Figures

Nomenclature

a	acceleration (velocity change in a time period)
$\mathrm{d_p}$	particle diameter
C_f	skin friction
f	frequency
k	Boltzmann constant
Kn	Knudsen number
p	pressure
Re	Reynolds number
St	Stokes number
t	time
T	temperature or threshold
u	streamwise velocity
u'	streamwise velocity fluctuation
U	freestream streamwise velocity
U^*	transformed velocity
x (X)	streamwise distance from the compression ramp corner
y (Y)	vertical distance from the wall
δ_0	boundary layer thickness
δ_{99}	99%-velocity boundary layer thickness
δ_{999}	99.9%-velocity boundary layer thickness
γ	shock foot intermittency
λ	mean free path
μ	fluid coefficient of viscosity
ρ	fluid density
ρ_p	density of a particle
σ	standard deviation
τ	time constant

Superscripts and Subscripts

0	stagnation condition
f	flow
p	particle
w	wall condition

∞	freestream

Abbreviations

A/D	analog-to-digital converter
CCD	charge coupled device
CFD	computational fluid dynamics
FLC	ferroelectric liquid crystal
LDV	laser Doppler velocimetry (or LDA)
PIV	particle image velocimetry
PLS	planar laser scattering
RMS	root-mean-square
SNR	signal-to-noise ratio
SRS	Stanford research systems (timing boxes)
SWTBLI	shock wave turbulent boundary layer interaction
TTL	transistor-transistor logic

Chapter 1

Introduction

1.1 MOTIVATION

Shock-induced turbulent boundary layer separation is a critical issue in the design of nearly all supersonic/hypersonic aircraft, missiles and projectiles. For example, Fig. 1.1 shows several locations where shock wave turbulent boundary layer interactions (SWTBLI) would exist on a hypothetical hypersonic vehicle. In many cases, the interaction consists of a strongly separated flow, which is highly unsteady and exhibits fluctuations at a wide range of length and time scales. The unsteadiness causes large fluctuating pressure loads and heat fluxes, which can lead to structure fatigue and thermal management problems. Furthermore, it is the unsteady properties that have proven to be the most difficult to model with even the most advanced numerical simulations. It is for this reason that the aim of the current work is to improve upon our basic knowledge of unsteady shock-induced turbulent separated flows by the application of advanced particle image velocimetry (PIV) techniques. PIV has seen only limited use in such complex flows, but it provides a powerful tool for investigating these flows because it enables the acquisition of global flow field information that is difficult to obtain by any other means. The objective of this work is to obtain an improved understanding of the nature of the unsteadiness, which can be critical to the development of new techniques for controlling the deleterious effects associated with SWTBLIs.

A great deal of work has been directed at investigating the characteristics of SWTBLI over the past 50 years. Much of this work is discussed in a number of review papers that have been written over the past few decades: Adamson & Messiter (1980), Viswanath, (1988), Settles & Dolling (1992), Dolling (1993 a,b), Smits & Dussauge (1996), Andreopoulos et al. (2000) and Dolling (2000). Owing to the breadth of work that has been done in SWTBLIs, in this chapter, the author will only touch on those concepts that are most important and/or closely related to the current study.

1.2 CLASSIFICATION OF SWTBLI

As suggested by Fig. 1.1, there are several types of SWTBLIs, which can vary substantially in their mean and fluctuating characteristics. Settles and Dolling (1992) discuss several “canonical” geometries that have been used in the study of SWTBLI. They term interactions as "semi-infinite" if the overall dimensions of the shock-wave generator are large enough that further increase in those dimensions will not change the interaction properties. Whenever the shock generator cannot produce a semi-infinite interaction, then it can be considered to be "non-semi-infinite" or a "protuberance" interaction. They termed interactions "dimensionless" if a semi-infinite shock generator imposes no characteristic length scale on the interaction; otherwise, it is termed "dimensional." The models that produce dimensionless interactions include sharp swept/unswept fins, swept compression ramps, semicones, ogive-cylinder/inclined flares, and many others.

Models typically used to generate dimensional interactions include circular cylinders, swept/unswept blunt fins, swept forward-facing steps and unswept 2-D compression ramps.

1.3 LITERATURE REVIEW

The current study focuses on the unsteady structure of a SWTBLI generated by an unswept compression ramp. An unswept compression ramp is a ramp with its leading edge perpendicular to the incoming flow and the streamwise angle is the same at any spanwise location. The drawing of an unswept compression ramp is shown in Fig. 3.3. Because of this, the following literature review will focus on previous studies of compression ramp interactions.

1.3.1 Mean Structure of SWTBLI Generated by Compression Ramps

SWTBLIs generated by unswept compression ramps have been studied extensively. Settles et al. (1976) used static and pitot pressure measurements, and surface streakline visualization to investigate the mean flow field for a 24^o compression ramp in Mach 2.85 flow. The mean flow structure inferred from their measurements is similar to that shown in Fig. 1.2a (from Müller, 2001). The shock system originates well upstream of the ramp corner, starting with the "separation shock" that induces boundary layer separation immediately downstream. The separation shock strengthens with downstream location due to the coalescence of compression waves until it reaches the theoretical inviscid shock strength well downstream of the ramp corner. The coalescence of the compression waves near reattachment may form a shock wave before they merge with the leading separation shock at the triple point. In this case a familiar λ-shock system will be present. The separated flow reattaches on the ramp face at about ½δ downstream of the corner. Figure 1.2b is a close-up view of the streamlines in the vicinity of the 24° compression corner, and shows a relatively straight zero-velocity line connecting the separation and reattachment points. The peak reverse velocities were estimated to be up to 16% of the freestream velocity U_∞. The separation "bubble" was shallow near the separation point but full and rounded near reattachment. The figure also shows that the mean zero velocity line starts at $x/\delta \sim -1.5$ and ends at $y/\delta \sim 0.2$. Figure 1.2c shows the mean velocity contours for a 24° ramp in Mach 2.5 obtained by Müller (2001) with LDA measurements. The reverse flow region in Fig. 1.2c is very shallow and extends only to about 1 mm from the wall. The maximum mean reverse flow was less than 5% of the freestream velocity U, which was much smaller than the 16% measured with pitot probes by Settles et al. (1976).

Settles et al. (1979) studied 8°, 16°, 20° and 24° compression ramps in Mach 2.85 flow by both experiments and computations. Their microsecond spark shadowgraphs are shown in Fig. 1.3. The 8° ramp was observed to have an attached shock with a sharp shock "foot". The shock foot is defined as the point on the separation shock that contacts the wall. The 16° ramp showed incipient separation, the shock foot was not as distinct as in the previous case, and it presented only a small amount of upstream influence. However, for the 20° and 24° ramps, the shock foot was even less distinct and exhibited greater upstream influence. Ardonceau (1984) studied SWTBLIs experimentally with attached, incipient separated, and separated flows. The SWTBLIs were generated by ramps with angles of 8^o, 13^o and 18^o respectively in a Mach 2.25 flow. The studies by Ardonceau (1984) and Settles et al. (1979) also showed that whether a ramp of a particular angle generates a separated flow is Mach number dependent.

The surface streak patterns for the 16^o and 24^o ramps obtained by Settles et al. (1979) are shown in Fig. 1.4. This figure shows clearly that while incipient separation was two-dimensional, the separated flow was not strictly two-dimensional as some ripples were observed along the separation line. The surface streak patterns for the attached flow, which is not shown in Fig. 1.4, showed that the attached flow was effectively two-dimensional. However, pressure measurements, by Marshall and Dolling (1992), for a 28^o ramp in a Mach 5 flow showed that the rippling in the instantaneous separation shock foot typically had an amplitude of less than 0.17δ and a wavelength of at least 1.5δ.

Settles et al. (1979) used both surface pressure and skin friction distributions, reproduced in Fig. 1.5, to determine the extent to which interactions contain regions of separated flow. For example, the mean pressure distribution for an interaction with significant upstream influence is exemplified by the 24^o ramp distribution shown in Fig. 1.5a. The mean pressure is seen to exhibit an abrupt increase near $x/\delta=-2$, which marks the location of upstream influence. This abrupt rise in pressure ends at the mean separation line 'S' and is followed by a more gradual increase in pressure, until reattachment 'R', where the pressure once again increases more rapidly. Far downstream on the ramp face the pressure reaches its asymptotic inviscid state appropriate to an oblique shock formed by a

24^{o} wedge. The skin friction distributions, shown in Fig. 1.5b, show that for incipient separation, the skin friction coefficient is zero at the ramp corner and positive everywhere else. The larger ramp angles exhibited extended regions of zero (or even negative) values of the skin friction coefficient, indicating the presence of a strongly separated flow.

Disimile and Scaggs (1989) studied the effect of Reynolds number on 2D compression ramp interactions. They concluded that the upstream location of the separation line reached an asymptotic state and was relatively unaffected by the increase of Reynolds number for unit Reynolds numbers between 2.3×10^{7} m^{-1} and 9.8×10^{7} m^{-1}.

1.3.2 Characteristics of SWTBLI Unsteadiness

Studies by Bogdonoff (1955) with high-speed cinematography and Kistler (1964) with fluctuating wall pressure measurements provided the earliest observations of SWTBLIs unsteadiness. Since that time a large number of researchers have investigated the unsteadiness of shock-induced turbulent separation. Those studies that are most relevant to the current work will be reviewed below.

Dolling and Murphy (1983) studied the SWTBLI generated by a 24^{o} unswept compression ramp in Mach 3 flow using high frequency response pressure transducers. They defined the intermittency factor γ, which is the fraction of time that the separation shock foot spends upstream of a given transducer, as a measure of the separation shock unsteadiness. The streamwise distribution of the intermittency factor γ from their study is shown in Fig. 1.6. The size of the intermittent region inferred from these measurements was about 0.5δ, which spanned the range from $\gamma = 0$ to $\gamma = 1.0$.

Ardonceau (1984) used LDV and hot-wire anemometry to study Mach 2.25 compression ramp interactions and found that much of the turbulence kinetic energy throughout the interaction is contained in large-scale structures of order 2δ in scale. Furthermore, they concluded that these energy containing eddies were not destroyed as they passed through the interaction. They additionally observed that low-frequency unsteadiness was associated with the separation bubble, but this low-frequency motion did not seem to affect other parts of the interaction. Furthermore, it was found that $\overline{u'v'}$ increased more rapidly than $\overline{u'}^2$ and $\overline{v'}^2$ in the first part of the interaction and decreased more rapidly farther downstream.

Kuntz et al. (1987) conducted LDA measurement of SWTBLIs generated by ramps with different angles. The interactions were found to decelerate the inner region of the mean velocity profiles more than the outer region. Downstream of the interaction, the inner region was accelerated more than the outer region. The mean streamwise profiles downstream of the compression corner were more wake-like. Significant increases of turbulence intensity and Reynolds stresses through the interaction were also found. Smits and Muck (1987) also showed that all turbulent stresses increase steeply upon encountering the shock. The maximum amplification of the RMS quantities were found to be approximately proportional to the overall static pressure rise. They concluded that the turbulence amplification for a weak shock was caused directly by the inviscid amplification across the shock and the adverse pressure gradient. The turbulence amplification for strong shocks, however, was mainly caused by the shock oscillation.

Selig (1988) and Selig & Smits (1991) attempted to control the SWTBLI generated by a 24^o ramp in Mach 2.84 flow with pulsed injection in the separation region. The injection mass flux rate was 9% or 2.5% of the free stream mass flux, and the injection frequency was 1.0 or 2.5 kHz. The injection effectively controlled the shock frequencies but had no strong effect on the speed of shock motion. They concluded that the oscillating shock was not the principal cause for the turbulence amplification. Instead, they suggested that large-scale coherent structures, such as Taylor-Görtler vortices and lateral vortices, might cause the turbulence amplification. Selig & Smits (1991) proposed two mechanisms that amplify the turbulence in SWTBLIs: “inviscid compression” of existing turbulence, and large-scale mixing processes associated with the separated flow and reattaching shear layer.

Andreopoulos and Muck (1987) studied ramp-generated shock unsteadiness by making fast-response pressure measurements. They concluded that the frequency of the shock oscillation was essentially independent of the downstream separated flow. Furthermore, because of the similarity in the upstream boundary layer bursting frequency and shock motion frequency, they suggested that the upstream boundary layer is most likely the cause of separation shock oscillation. They also developed a conditional-sampling technique to separate effects of shock-wave oscillation from those of turbulent transport.

Muck et al. (1988) studied the interactions generated by 2-D ramps with flush mounted, miniature, high frequency pressure transducers. Two distinct phenomena that might affect the interaction were proposed: (*i*) flapping motions of the shock wave that dominate the region just upstream of the mean separation line, and (*ii*) convective turbulence effects that dominate the separated region. The spanwise rippling, which was typically found in strong 2D ramp SWTBLIs and made the flow not strictly two-dimensional, was believed to be caused by the incoming turbulent eddies convected into the interaction.

Selig et al. (1989) used hot-wire anemometry to study the turbulence properties in SWTBLIs generated by a 24^{o} ramp in Mach 2.84 flow. The shock oscillation frequencies were found to be broadband and centered at 1.5-2 kHz. They further noted that the shock foot unsteadiness and reattached boundary layer seemed to be essentially decoupled from the dynamics of the separated flow. The mean and maximum mass-flux turbulence intensities through the interaction were amplified by a factor of 2 and 5, respectively. The mass-flux probability density functions (PDF) profiles, measured by Selig et al. 1989 and Selig & Smits 1991 at locations that were upstream and downstream of the interaction, are shown in Fig. 1.7. The PDFs measured upstream of the interaction exhibit a Gaussian-like distribution typical of a fully turbulent boundary layer. In contrast, some of the PDFs measured downstream of the interaction (e.g. at y=14.87 mm) exhibit a bimodal distribution with the two peaks representing typical mass-flux values corresponding to the freestream and closer to the wall. The bimodal distribution suggests that the reattached boundary layer is highly intermittent. They suggested that two different turbulence models, appropriate to the upstream and downstream locations, may be needed in numerical simulations.

Gramann and Dolling (1990) developed a technique to detect the shock-induced separation using fast response pressure transducers. They tested the technique in the interaction generated by semi-infinite cylinders in Mach 5 flow. The instantaneous separation point was found to be at, or close to, the instantaneous shock foot in the intermittent region. Furthermore, the separation point was found to exhibit large-scale streamwise motion.

Dolling and Brusniak (1989) conducted an analysis of surface pressure fluctuations underneath the intermittent region of SWTBLIs generated by a fin, cylinder and compression ramp in Mach 5 flow. They demonstrated that the dominant frequencies of the shock foot motion were in the range of 0.4 kHz to 2 kHz. Using similar fast response pressure measurements under the intermittent region, Erengil and Dolling (1991a) studied a 28^{o} compression ramp generated interaction in Mach 5 flow. The streamwise profile of the RMS wall pressure is shown in Fig. 1.8a, where the subscript 'o' refers to the undisturbed conditions just upstream of the interaction. There is a local peak in the RMS pressure just upstream of the separation point, whereas the standard deviation is relatively low in the separation region and rises sharply after reattachment. Sample power spectral density (PSD) functions at different locations underneath the intermittent region are shown in Fig. 1.8b. Location 1 is essentially upstream of the intermittent region where the pressure fluctuations are dominated by the undisturbed boundary layer turbulence. At locations 2 & 3, which are located underneath the region of shock motion, the PSDs exhibit two peaks. The low frequency peak is due to the separation shock foot motion and the high frequency peak is due to boundary layer turbulence. They concluded that the shock foot motion occurs at frequencies of less than 3-4 kHz. This frequency range is substantially less than the characteristic frequencies in the boundary layer, which was of order 10-50 kHz. Figure 1.9 shows a sample time-history of the streamwise shock foot position as inferred from wall pressure measurements (Dolling 1993). This figure clearly shows the wide range of frequencies and scales of motion exhibited by the shock foot.

1.3.3 Sources Of The SWTBLI Unsteadiness

Although the characteristics of the SWTBLI unsteadiness have been relatively well documented, the underlying mechanisms that drive the unsteadiness are currently not well understood. The driving mechanism(s) of the unsteadiness may be the upstream turbulent boundary layer, an instability associated with the separation/reattachment process, or a combination of both. Most attention to date has been directed at investigating the role of the upstream boundary layer on the shock foot unsteadiness.

As discussed above, Andreopoulos and Muck (1987) concluded that the characteristic frequencies of shock oscillation were largely independent of the downstream separated flow. Furthermore, the similarity of the shock frequencies and upstream boundary layer bursting frequency suggested that the upstream boundary layer drives the shock unsteadiness. However, these frequencies may not have been as well matched as they thought because Dolling & Brusniak (1989) suggest that the shock frequencies measured by Andreopoulos and Muck may have been significantly overestimated. The reason for this is that their “single-threshold” shock detection algorithm, may have interpreted turbulent boundary layer pressure fluctuations as shock passage events. Dolling & Brusniak (1989) developed a two-threshold algorithm and showed that it was less likely to detect false shock events and this resulted in significantly lower estimates of the characteristic shock frequencies.

Erengil and Dolling (1991b) developed conditional sampling algorithms for SWTBLI generated by a compression ramp in Mach 5 flow. They specifically investigated the possibility of a correlation between pressure fluctuations in the incoming flow and the separation shock motion. Weak or no correlation between the incoming pressure fluctuations and the shock wave's large-scale motion was found. In contrast, a clear correlation was found between the upstream pressure fluctuations and the changes of the shock's direction. In particular, downstream-to-upstream shock turnarounds corresponded to a rise-fall-rise pressure signature, whereas upstream-to-downstream turnarounds corresponded to a fall-rise-fall pressure signature. They proposed that large-scale turbulent structures, which are convected into the interaction, are responsible for the shock's high-frequency jitter; however, a different, but unknown, mechanism is responsible for the shock's large-scale oscillations.

Erengil and Dolling (1993b) used fast-response wall pressure measurements to study Mach 5 compression ramp interactions and found strong correlations between the shock foot velocity and the instantaneous pressure ratio across the shock. Sample correlations taken from their study are shown in Fig.1.10. The negative time delay in Fig. 1.10 means that fluctuations in shock velocity $V_s(t)$ are preceded by those in the pressure ratio $R_s(t)$. Their study was the first to provide experimental evidence of a cause-and-effect relationship between wall pressure fluctuations and the separation shock foot unsteadiness. They proposed that fluctuations in the static pressure ratio across the shock induce fluctuations in the shock velocity, which in turn causes a change in the separation shock position. They concluded that the small-scale motion of the shock was caused by its response to the convection of turbulent fluctuations through the interaction. They further argued that the large-scale motion was a result of the shock's displacement due to the expansion and contraction of the separation bubble; however, no mechanism was identified for the cause of the separation bubble's low frequency, large-scale pulsating motion. It is the large-scale motion that is of greatest interest because it has proven to be the most difficult to model computational. Ünalmis and Dolling (1998) made measurements in the same wind tunnel as used by Erengil and Dolling (1993b) and showed that there was a stationary spanwise vortex structure in the incoming boundary layer, which they suggested might be one of the causes of the low-frequency pulsation of the separated flow. The source of the stationary vortices was not clear at that time but it is possible that Göertler vortices, generated by the concave curvature of the nozzle, were the cause.

Brusniak and Dolling (1994) studied the wall pressure fluctuations for blunt fin in Mach 5 flow. They introduced the global pressure distribution hypothesis. Under this hypothesis, the stretching and contraction of a single, universal pressure profile, is responsible for the fluctuating pressure profile measured under the intermittent region. An illustration of this profile, stretched by different amounts, is shown in Fig. 1.11. The global pressure distribution stretches and flattens while the shock moves upstream, whereas it compresses and sharpens while the shock moves downstream. A model based on this global pressure distribution was developed and it showed good agreement with low-frequency shock-foot position history data.

Beresh et al. (1998) used planar flow visualization and fast response pressure measurements to monitor the shock foot location in a Mach 5 compression ramp interaction. They visualized the flow by using planar laser scattering (PLS) from a seeded alcohol fog. In that study the seeding density was sufficiently high that the shock foot could be seen in most of the images. Double-pulsed image pairs, separated in time by 15 to 30 μs, showed that large-scale structures in the upstream boundary layer would greatly distort the outer region of the separation shock, but the shock *foot* did not move appreciably on this time scale. This result was consistent with the previous studies using wall pressure measurements, which reported that the shock frequencies did not exceed 10 kHz. They concluded from this that large-scale structures in the outer part of the upstream boundary layer were not primarily responsible for the motion of the separation shock. This observation seems to differ from the observations of Wu et al. (2000) and Wu & Miles (2000) who obtained 500 kHz image sequences (30 images) of a Mach 2.5 compression ramp interaction using planar Rayleigh scattering. They found that the unsteadiness of the shock wave was in direct response to the passage of structures in the incoming boundary layer. Wu and Miles (2000) concluded: "Some large eddies in the boundary layer cause the shock to move in the streamwise direction for distances as large as the boundary layer thickness at a frequency as high as 100 kHz." It appears that this observation contradicts much of the earlier work based on surface pressure measurements.

McClure (1992) and Ünalmis & Dolling (1994, 1999) used pitot-pressure measurements in the upstream boundary layer together with fast-response static pressure measurements underneath the intermittent region to locate the shock foot position. They ensemble averaged the pitot-pressure data conditioned upon the shock foot position and motion, and found that a lower pitot pressure was correlated with an upstream shock location whereas a higher pitot pressure was correlated with a downstream shock location. These results led them to suggest that a relatively low frequency (<4 kHz) thickening and thinning of the upstream boundary layer drives the large-scale shock motion, i.e., when the boundary layer is thick, the shock is upstream, whereas when the boundary layer is thin, the shock is downstream. Chan (1996) and Beresh et al. (1998) explored this possible mechanism by using planar laser imaging and simultaneous fluctuating wall pressure measurements in a Mach 5 compression ramp interaction. Beresh et al. (2002) also studied this with simultaneous Particle Image Velocimetry (PIV) and fluctuating wall pressure measurements. These studies suggested that there was no significant correlation between the upstream boundary layer thickness and the shock foot location.

Beresh et al. (1999 and 2002) used PIV and fast response pressure measurements to investigate the relationship between the turbulent velocity fluctuations in the upstream boundary layer and the shock foot motion. They studied an interaction generated by a 28^o two-dimensional ramp in Mach 5 flow. As discussed above, they did not find a correlation between boundary layer thickness and shock foot motion, but they did find a correlation between velocity fluctuations in the upstream boundary layer and shock motion. In particular, they showed that positive velocity fluctuations in the lower part of the boundary layer were correlated with downstream motions of the separation shock, whereas negative velocity fluctuations were correlated with upstream shock motion. Figure 1.12a shows their conditional ensemble average profiles of the streamwise fluctuations in the incoming boundary layer conditioned on the separation shock foot motion within a time period of 250 µs. They argued that these results were consistent with the physical principle that downstream motion of the shock is associated with fuller instantaneous velocity profiles that are more resistant to separation and therefore are more likely to be associated with a downstream shock location. Figure 1.12b shows an illustration of the relationship. Their results are in general agreement with the large-eddy simulations of Hunt and Nixon (1995) that showed an approximately one-to-one relationship between the shock velocity and the incoming turbulent velocity fluctuations. Ünalmis et al. (2000) studied Mach 5 blunt fin interactions using measurements that were similar to those made by

Beresh et al. (2002). They found that the blunt fin interactions exhibited a similar correlation between the shock foot motion and the upstream turbulent velocity fluctuations.

1.3.4 Numerical Simulations of SWTBLIs

One of the earliest attempts to study SWTBLIs by numerical simulations, which was stated as "a computational solution of the Navier-Stokes equations" without further explanation, was done by Settles et al. (1979) and successfully simulated attached flows but not separated flows. Hung and Buning (1984) studied the mean characteristics of blunt-fin generated SWTBLI with a Reynolds-averaged Navier-Stokes (RANS) simulation and obtained good agreement with experiments. The success of the mass averaged Navier-Stokes simulation study by Ong and Knight (1987), which used MacCormack explicit-implicit predictor-corrector and Beam-Warming fully implicit algorithms, was also limited to comparisons of mean surface pressure with experimental data.

Adams (1998, 2000) conducted Direct Numerical Simulation (DNS) studies of 18^{o} compression ramp in a low Reynolds number ($Re_{\theta}=1685$) Mach 3 flow. Adams (1998) concluded that quantitative comparison with available experimental results was not possible for the foreseeable future because DNS could not achieve the same high Reynolds numbers as experiments do. Adams (2000) pointed out the limitations of the DNS simulations such as small Reynolds number and small spanwise simulation domain due to the limited computational power. The small Reynolds number flow has small mean-streamline curvature. The shock will not penetrate deeply into the boundary layer due to the small mean-streamline curvature because the shock's origin is the compression waves generated from the sonic layer, which is closely related to the mean-streamline curvature. However, it is important to be able to simulate the deep shock penetration in high-Re flow because the magnitude of the near-wall pressure gradient is different from that in low-Re flow, as a result, the separation sizes will be different. The small spanwise simulation domain, which was on the order of one boundary layer thickness in the DNS simulation and was much smaller than that in experiments (typically 10 times the boundary layer thickness), makes it impossible for DNS to detect large spanwise structures such as Görtler vortices. Adams (2000) suggested two reasons why RANS codes would have trouble computing separated SWTBLIs. First, the meaning of a time-averaged RANS solution becomes unclear in a flow with large-scale shock motion. Second, RANS cannot predict the compressibility effects at the shock foot region for high Reynolds number flow because the density increase around the shock foot is induced by the unsteady shock but not the turbulent structures.

Large-eddy simulation (LES), as an intermediate method between expensive DNS and perhaps less accurate RANS simulations, has been frequently applied to SWTBLI in recent years (Urbin et al., 1999; Rizzetta et al. 2001; Garnier et al., 2002; Rizzetta and Visbal, 2002). For example, the LES results for a Mach 3 compression corner by Urbin et al. (1999) showed good agreement of surface pressure, mean velocity, and static temperature with those from low Reynolds number experiments. Furthermore, Rizzetta and Visbal (2002) conducted LES of a Mach 3.0 flow with different compression ramp models. The success of their results, again, was confined to matching mean surface pressure distribution with that of the experiments.

In summary, present numerical simulations in SWTBLI studies are relatively successful at predicting some mean quantities of separated SWTBLIs, such as the mean and RMS pressure distribution. However, some basic aspects of the flow unsteadiness, such as the characteristics of the large-scale pulsations of the separated flow, have not been adequately captured to date, even with the most advanced LES computations (Dolling, 2000). Clearly, continued development of advanced simulation tools is warranted, but it is likely that experimentation will remain the source of new understanding of these complex flows, at least for the foreseeable future.

1.3.5 Control of SWTBLI Unsteadiness

The ultimate goal of studying SWTBLIs is to be able to mitigate their deleterious effects by improved structural design or even to control them by active means. Attempts to control SWTBLIs date back to the 1950s, and most of this work has been directed at controlling or modifying the mean characteristics of the interactions. The most commonly used techniques to control unsteadiness are suction, tangential blowing, and natural bleed. Natural bleed is the combination of suction and blowing by ventilating the high-pressure air in the separation region to a low- pressure region. Suction removes low momentum flow close to the wall so that high momentum flow away from the wall will come down to the wall. Blowing provides high momentum flow directly to the flow close to the wall.

Both methods increase the momentum of the flow close to the wall, which enables the boundary layer to resist separation better.

Early studies showed that tangential blowing can be effective in reducing the scale of the separated flow in both 2-D and axisymmetric interactions, but many of the general features and important parameters that governed the process were not clear to the researchers (Viswanath, 1988). Some important parameters for blowing-control are the jet-velocity, density, physical scale, and location. Based on studies in the 1970s, Viswanath (1988) summarized two types of blowing classified by the blowing locations: U-type and D-type injections. In U-type injection, the blowing location is upstream of the location where the separation point would be without the injection; otherwise, it is called D-type injection. For U-type injection, the injection was found to be most effective if it was located about 6δ upstream of the separation point. Furthermore, the optimal injection pressure depends on injection location and compression angle, and the wrong injection pressure can cause an increase of the separation size. Viswanath (1988) concluded, based on his previous studies, that D-type injection was better than U-type injection. The speculated reasons for the superiority of D-type injection were that the injection entrains recirculating fluid and removes the reattachment point.

Gefroh et al. (2002) and Doerffer & Bohning (2003) studied the effectiveness of passive cavity recirculation, which is a type of natural bleed. Gefroh et al. (2002) used mesoflaps, which involve a matrix of small flaps covering a passive cavity, to study an oblique shock impinging on a boundary layer in a Mach 2.41 flow. The flaps were deflected by the local gas dynamic pressure loads so that proper mass bleed or injection could be obtained. Some improvement from thin mesoflaps has been observed, such as reduced boundary layer thickness and better stagnation pressure recovery downstream of the interaction. However, as they pointed out, further study of three-dimensional effects were needed to evaluate the overall performance. Doerffer & Bohning (2003) concluded, from the study of a normal shock impinging on a boundary layer, that passive cavity recirculation should not be used because it increased drag and pressure losses. They also suggested that active control should be added to passive control for better performance.

1.4 SUMMARY

The mean flow structure of SWTBLIs has been well documented over the past 50 years. There are many different types of interactions and the nature of the flow field tends to be highly dependent on the geometry and scale of the device that generates it. Strong interactions are associated with substantial upstream influence, boundary layer separation, followed by shear layer reattachment. Furthermore, the interaction flow field exhibits a high degree of unsteadiness, and it is the unsteadiness that poses the greatest challenge to computational models. Interestingly, the dominant frequencies that characterize the interaction unsteadiness tend to be an order of magnitude or so lower than the characteristic frequencies in the upstream boundary layer. Nevertheless, several studies have suggested that it is indeed the upstream boundary layer that drives the shock foot motion, although this is by no means definitive. Furthermore, some studies have suggested that the interaction unsteadiness may be driven by low-frequency fluctuations in upstream boundary layer, such as Göertler vortices, which may be wind tunnel dependent and perhaps not even present under flight conditions. Control of SWTBLIs is in a large sense, the primary goal of SWTBLI research, and several studies have shown that the mean flow field structure can be greatly modified by various techniques. However, typically high flow rates for suction and blowing were required, and it is not known if better, perhaps closed-loop, control techniques may give equivalent performance but at a lower cost. It is likely that improved control strategies will only be possible with improved understanding of the physics of SWTBLI. Finally, since current numerical simulations either have trouble being able to capture the relevant physics or cannot achieve the Reynolds numbers of interest, an improved understanding of the physics of SWTBLIs is not likely to come soon from modeling efforts. This emphasizes the importance of conducting new experiments on SWTBLIs that are explicitly directed at improving our understanding of the underlying physical mechanisms.

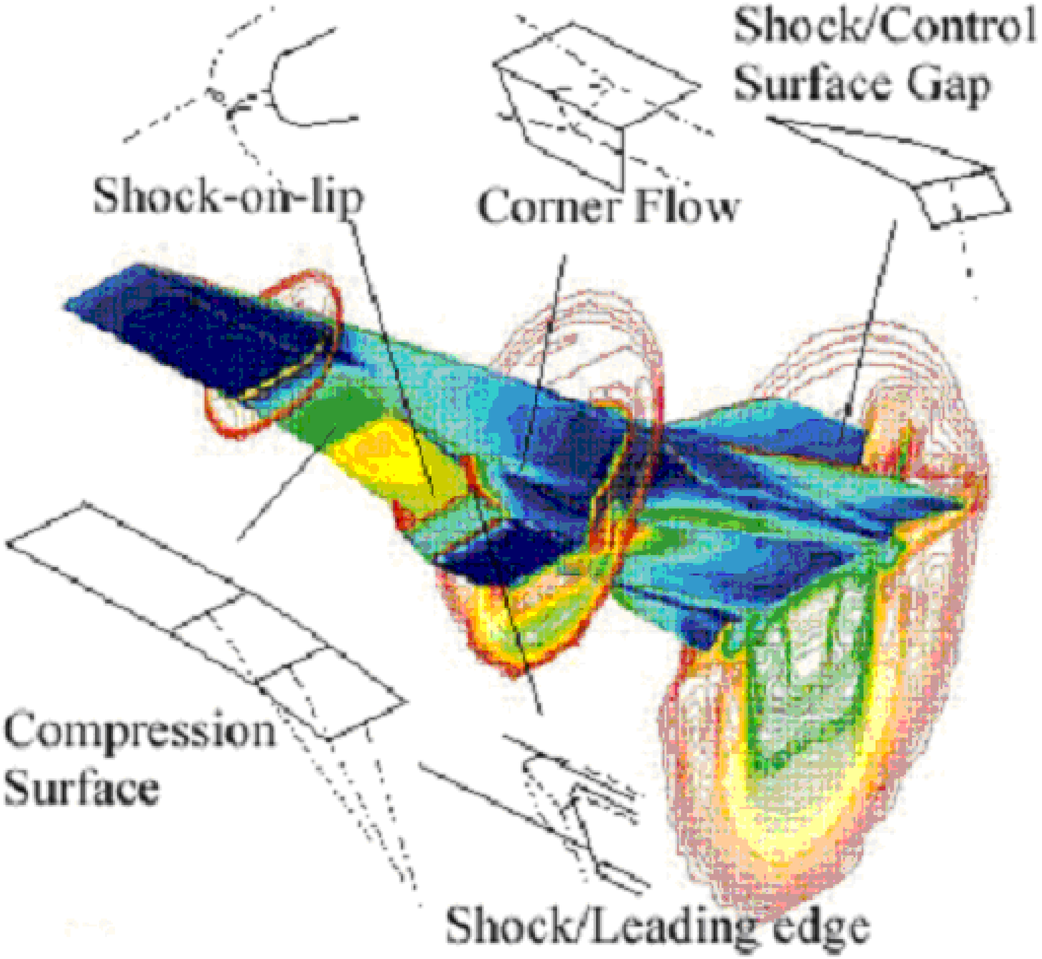

Courtesy: NASA/Langley Research Center (Vehicle)

Figure 1.1 Example SWTBLI on a hypothetical hypersonic vehicle.

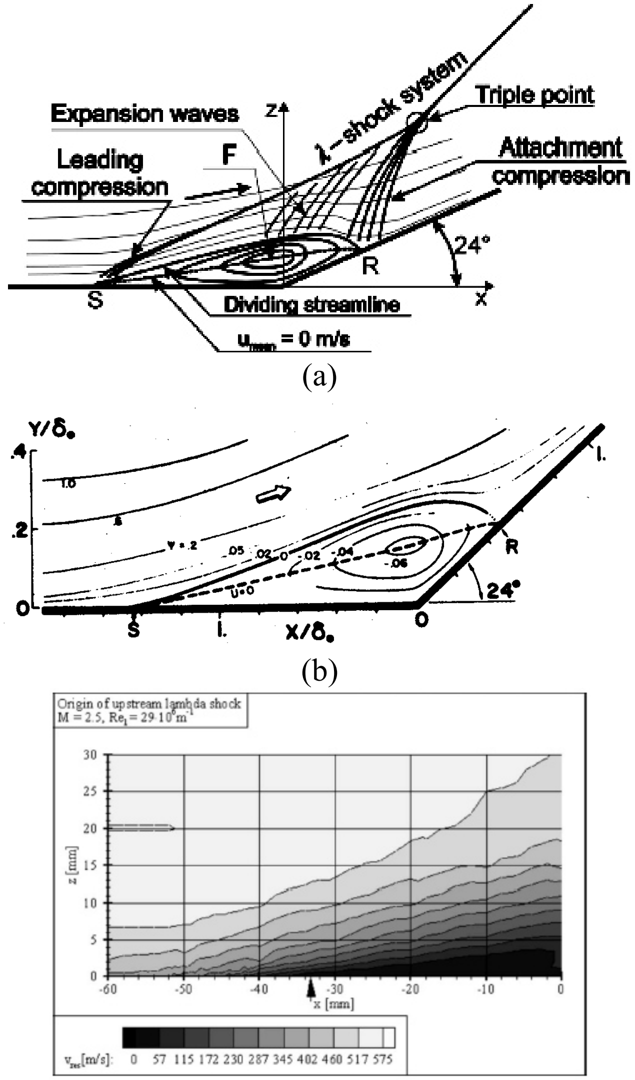

(a)

(b)

(c)

Figure 1.2 Structure of unswept compression ramp interactions. (a) Schematic diagram of the global flow field structures (Müller 2001); (b) Mean-flow streamlines in the vicinity of the corner of a 24^o compression ramp in a Mach 2.85 flow (Settles et al. 1976); (c) Mean velocity contours from LDA measurements for a 24^o compression ramp in a Mach 2.5 flow (Müller 2001).

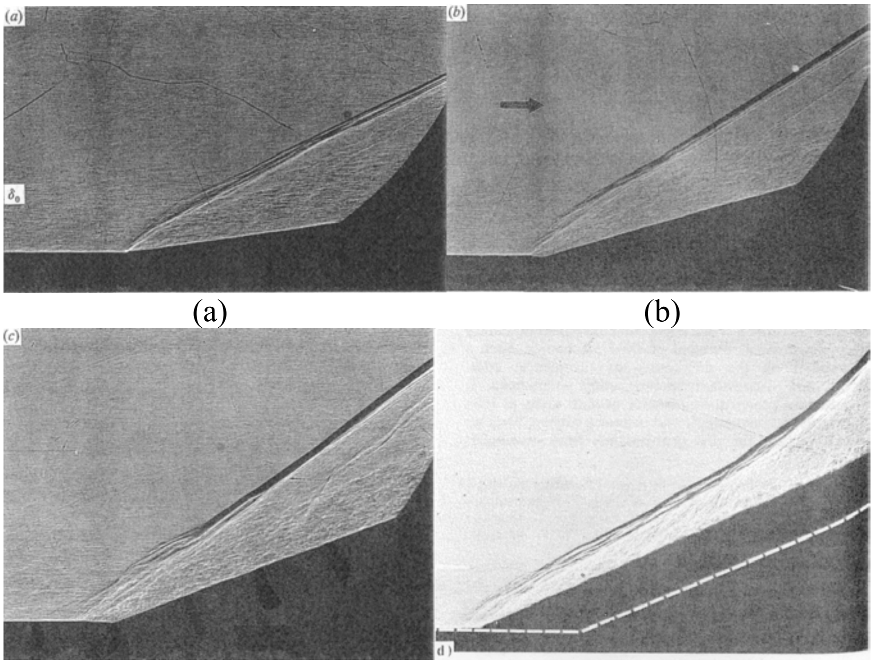

(a) (b)

(c) (d)

Figure 1.3 Microsecond spark shadowgraphs of a compression ramp interaction (Settles et al. 1979): (a) 8° ramp, attached shock; (b) 16° ramp, incipient separation; (c) 20° ramp, separation; (d) 24° ramp with side fences, separation.

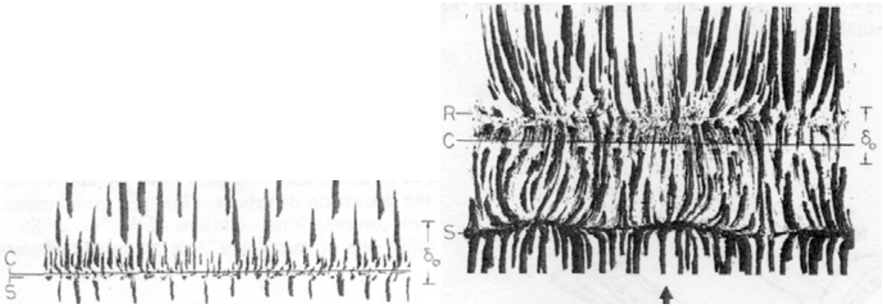

(a) (b)

Figure 1.4 Surface streak patterns measured in Mach 2.85 compression ramp interactions (Settles et al. 1979): (a) 16° ramp, incipient separation; (b) 24° ramp, separated.

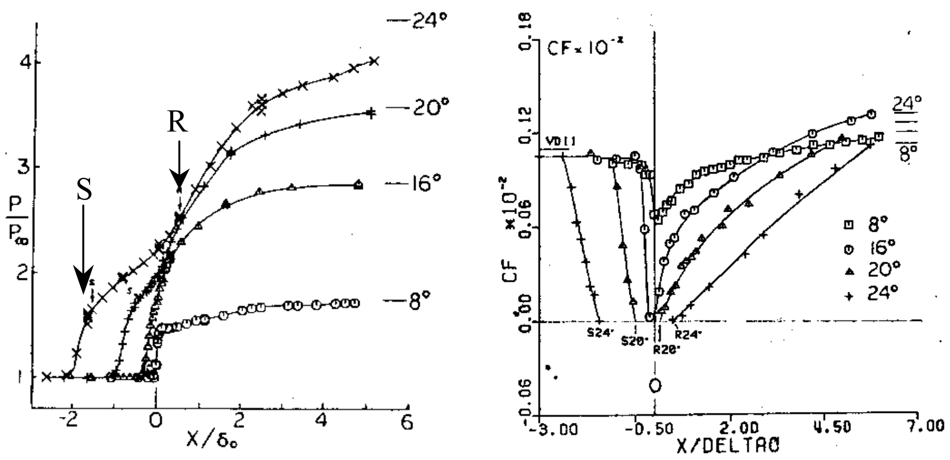

(a) (b)

Figure 1.5 Mean wall pressure and heat flux distributions taken along the centerline of Mach 2.85 compression ramp interactions (Settles et al. 1979). The data were taken for ramp angles of 8°, 16°, 20° and 24°. (a) surface pressure; (b) skin friction.

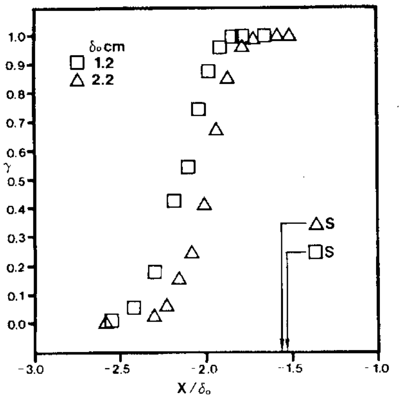

Figure 1.6 Streamwise distribution of intermittency γ for a Mach 3 compression ramp (24° with side fence) interaction (Dolling and Murphy 1983).

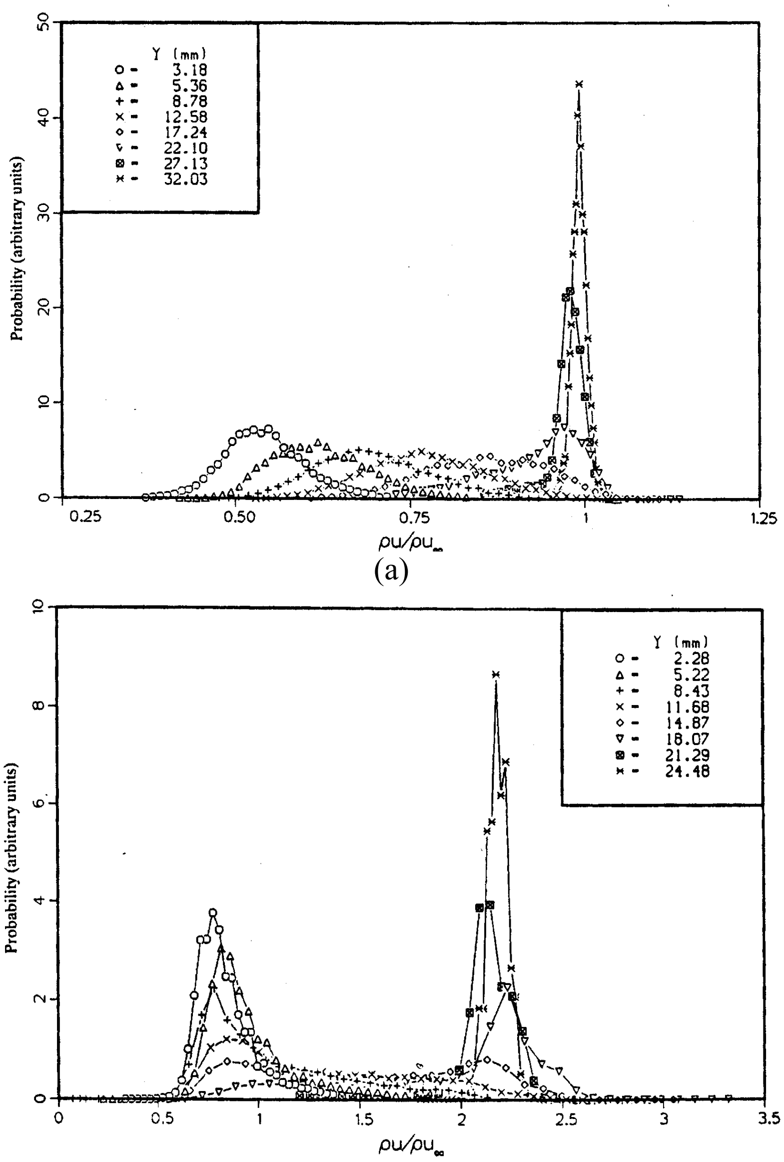

(a)

(b)

Figure 1.7 Probability density functions (PDF) of mass-flux acquired at several transverse locations (Y). The measurements were made upstream and downstream of a Mach 2.85 compression ramp interaction: (a) upstream, x= -95.4 mm; (b) downstream, x=91.4 mm. (Selig et al. 1989 and Selig & Smits 1991).

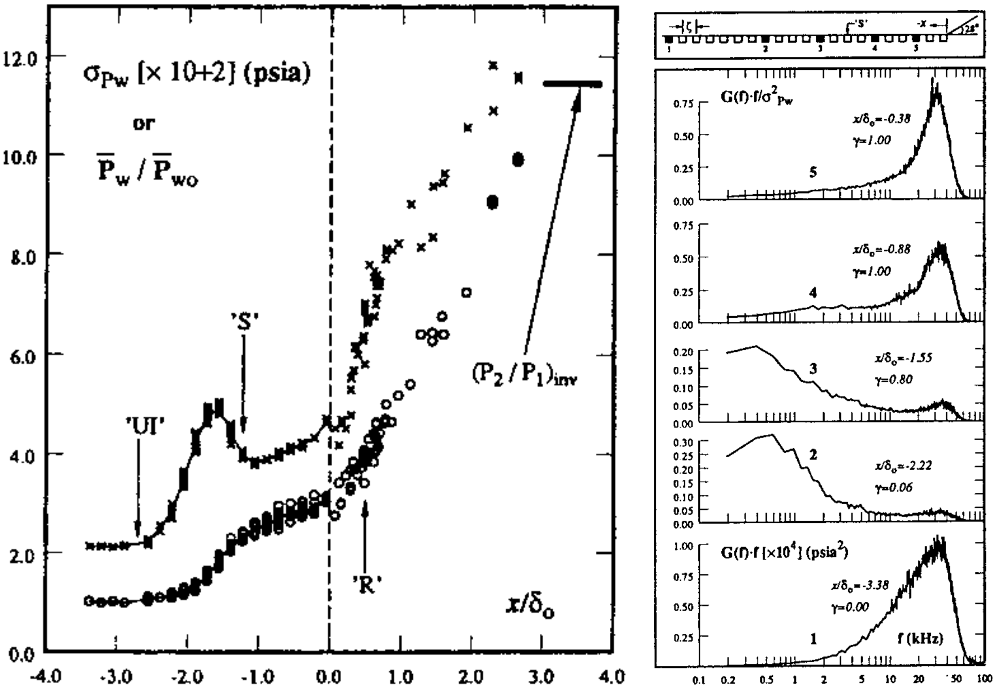

(a) (b)

Figure 1.8 Fluctuating pressure data measured by using flush mounted transducers underneath a Mach 5 compression ramp interaction. (a) mean and RMS pressure distributions; (b) power spectral densities measured at the 5 locations shown in the schematic at top. (from Erengil and Dolling 1991a).

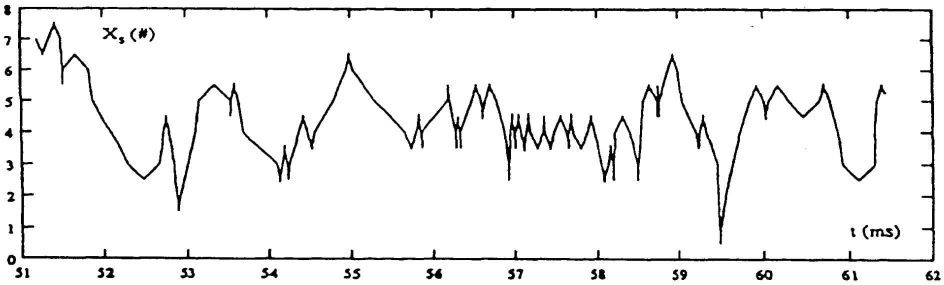

Figure 1.9 Sample history of the streamwise shock foot position for a 28° ramp in Mach 5 flow. The y-axis labels (1-8) represent the positions of the pressure transducers that are installed along streamwise direction in the intermittent region (Dolling 1993a).

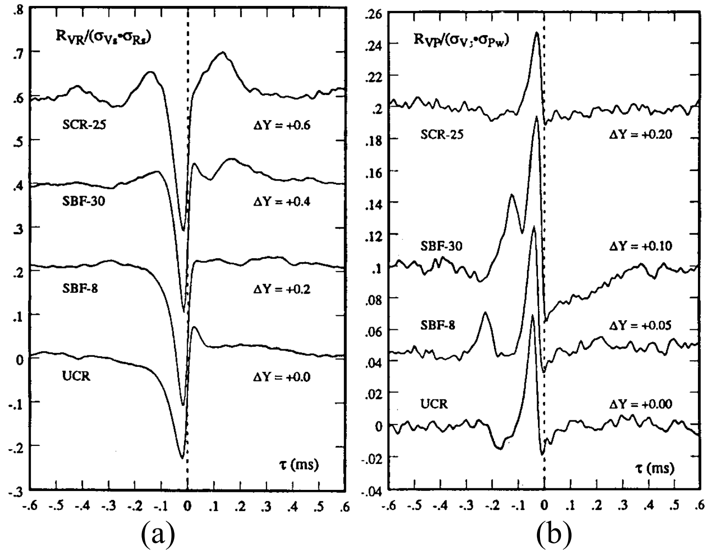

(a) (b)

Figure 1.10 Normalized cross correlation of shock velocity $V_s(t)$ and (a) pressure ratio $R_s(t)$, and (b) upstream pressure $P_w(t)$. UCR is an unswept 28° ramp; SCR-25 is a 28° ramp with 25° sweep angle; SBF-30 is 30° swept blunt fin; SBF-8 is 8° swept blunt fin. (Erengil and Dolling 1993b).

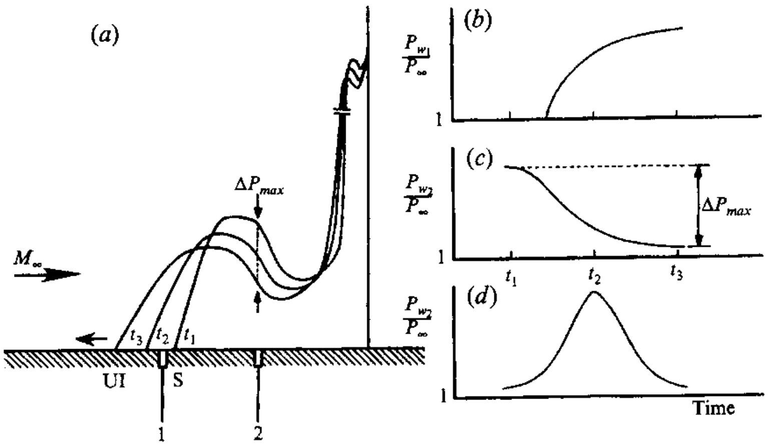

Figure 1.11 Global pressure distribution and its effects on unsteady pressure measurements (Brusniak and Dolling 1994): (a) global pressure distribution for shock sweep upstream; (b) pressure-time variation at station 1; (c) pressure-time variation at station 2; (d) pressure-time variation for shock downstream-to-upstream turnaround.

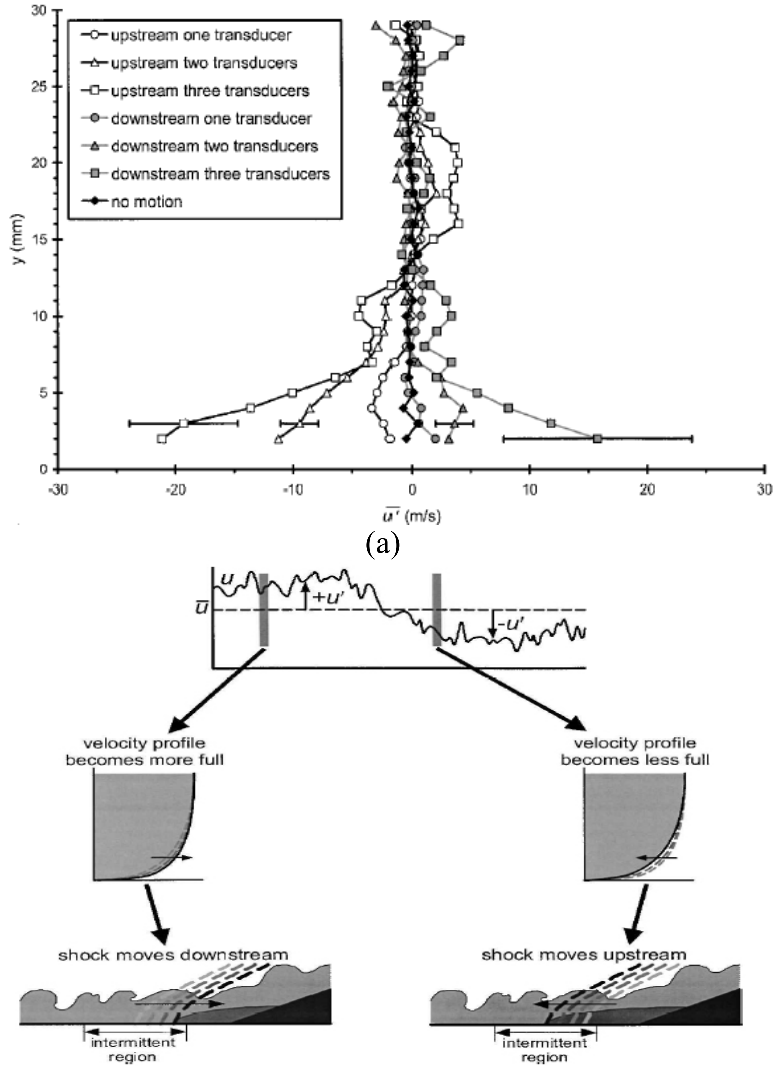

(a)

(b)

Figure 1.12 Correlation of velocity fluctuations in the upstream boundary layer with shock foot movement: (a) conditional ensemble average profiles of the streamwise fluctuations in the incoming boundary layer conditioned on the separation shock foot motion within a time period of 250 μs; (b) illustration of the effect of the instantaneous velocity profile on the shock foot motion. (Beresh et al. 2002).

Chapter 2

Objectives

The previous discussion indicates that a great deal is currently known about the unsteadiness of SWTBLIs, but many fundamental issues remain unresolved. For example, Beresh et al. (2002) identified a correlation between velocity fluctuations in the lower part of the upstream boundary layer and shock foot motion, but it is not known if this is the sole mechanism that drives shock motion. Furthermore, Beresh et al. (2002) suggest that the shock motion is probably more likely to be correlated with the rate of change of the upstream velocity profile (i.e. the acceleration) and not simply the velocity fluctuations. Their results also indicate that a thickening/thinning mechanism is not valid, but this is not consistent with the results of McClure (1992) and Ünalmis and Dolling (1999) who proposed such a mechanism based on fluctuating pitot pressure measurements. Finally, since most measurements that have been made to date have relied on either surface pressure measurements or point measurements with intrusive probes, or have been restricted to measurements in the upstream boundary layer, virtually nothing is known about the global flow field dynamics. For example, it has been inferred from surface pressure measurements that the separation bubble exhibits a large-scale expansion and contraction (Erengil & Dolling, 1993), but it is not known how these pulsations relate to the dynamics of other flow features, such as the separation shock foot and the reattachment region. Furthermore, reattachment is known to occur in the mean, but the dynamics of reattachment are not known, despite the possibility that a reattachment instability may play an important role in driving the interaction unsteadiness.

To enable the investigation of some of the issues raised above, a major objective of this research was to develop a new multi-laser, multi-camera PIV system for studies of shock-induced turbulent separation. This PIV system provides a powerful tool for investigating shock-induced separation because it enables the acquisition of wide field-of-view measurements of the velocity field that cover the undisturbed upstream boundary layer, intermittent region, separated flow and the region of reattachment. Furthermore, this PIV system can be used to capture time-sequenced PIV data with smaller fields of view, and this feature was used to investigate the dynamics of the flow structure.

The PIV system was used to make measurements in a Mach 2 compression ramp interaction in order to accomplish the following scientific objectives:

1. Determine the role of the upstream boundary layer in driving the unsteadiness of the separation shock foot. In particular, to determine whether the correlation between upstream boundary layer velocity fluctuations and shock-foot motion – observed previously in Mach 5 interactions – also applies in Mach 2 interactions. In addition, the upstream acceleration mechanism proposed by Beresh et al. (2002) was investigated briefly.

2. Investigate the global dynamics of the interaction by the application of wide-field PIV together with fluctuating surface pressure data to monitor the shock-foot location. Of primary interest is the relationship among the major flow features – i.e., the upstream boundary layer, separation shock, separated flow and reattachment region – as the separated flow undergoes its low-frequency pulsations. This type of information is important for understanding the global structure of the flow and for providing the type of data that are necessary to validate computational models such as large-eddy simulations, which are seeing increasing use to model high-speed turbulent flows.

Chapter 3

Experimental Facilities

3.1 MACH 2 WIND TUNNEL

All experiments were conducted in a Mach 2 blowdown wind tunnel located at the University of Texas at Austin. The constant-area test section is 6 inches (15.2 cm) wide by 6.3 inches (16 cm) high and has a length of 30 inches (76.2 cm). Removable side doors allowed access to an instrumented floor section. The wind tunnel supply air was compressed to a pressure of 1.7582×10^4 kPa (2550 psia) by a Worthington HB4 four-stage compressor and stored in external tanks with a total volume of about 140 ft^3 (4 m^3). The stagnation chamber pressure and temperature for the present experiments were approximately 261 ± 7 kPa and 292 ± 5 K, respectively. For these stagnation conditions, stable run times of up to 40 seconds could be obtained. The incoming turbulent boundary layer underwent natural transition and developed under approximately adiabatic wall temperature conditions. The freestream velocity and unit Reynolds number were 491 m/s and 3.3×10^7 m^{-1}, respectively. More information about the Mach 2 boundary layer can be found in chapter 5.

Figure 3.1 shows the test section with the compression ramp installed on the floor. On the front and the back sides of the test section, fused-silica windows of dimensions 6 × 2 × 0.75 inches were used for optical access into the tunnel. The ceiling of the test section had a fused-silica window of dimensions 6 × 0.5 ×

1.0 inches, which enabled access for the laser sheet. The floor was also equipped with a fused-silica window to provide an exit for the laser sheet. The purpose of this was to reduce the reflections from the floor of the tunnel. Two configurations are used for the floor window inserts as shown in Fig. 3.2. The first one in Fig. 3.2a uses a small fused-silica window of dimensions 4 × 0.5 × 1.0 inches, which was located at the centerline of the tunnel floor. A row of pressure transducers were located downstream of the window. The distance between neighboring transducers was 0.115 inch (2.92 mm). The second configuration, shown in Fig. 3.2b, had a larger fused-silica window that was parallel to the pressure transducers. The window was 6 × 0.5 × 1.0 inches and was slightly offset from the floor centerline. The pressure transducers were located on the floor centerline and had the same spacing as those in Fig. 3.2a.

3.2 RAMP MODELS

Two compression ramps were used for the experiments, one with an angle of 14 degrees and the other with an angle of 20 degrees (Fig. 3.3). The 14-degree ramp produced a shock that remained attached to the ramp, and was used in experiments to determine the particle response-time across an oblique shock. The 20-degree ramp produced a separated flow and was used for all of the studies of SWTBLI. Both models were 0.9 inches high and 5.2 inches wide, which left a 0.4-inch gap on each side. The model was not made full span because the tunnel would not start in that configuration. Fences on the side of the ramp could not be used because they would obscure the field of view of the camera. Surface flow visualization of the 20-degree ramp with kerosene / lampblack method was used in earlier studies by Austin (2001) and a sample image is shown in Fig. 3.4. It indicated that the mean separation line exhibited some curvature, but this was acceptable for the purposes of this study.

3.3 FLUCTUATING WALL PRESSURE MEASUREMENTS

Fluctuating pressure measurements were made by using Kulite Semiconductor Products, Inc., Model XCQ-062-50A transducers. These transducers had a nominal outer diameter of 0.0625 inch (1.59 mm) and a pressure-sensitive diaphragm of 0.028 inch (0.71 mm) in diameter. Perforated screens above the diaphragm protected the transducer from being damaged by dust particles in the flow but limited the frequency response to about 50 kHz. The transducers were flush-mounted on a rectangular instrumentation plug and their locations relative to the floor window are shown in Fig. 3.2. For the parallel configuration, shown in Fig. 3.2(b), the spanwise distance between the pressure transducers and the PIV laser sheet was about 4 mm. Output from the Kulite pressure transducers was amplified by Dynamics (Model 7525) amplifiers and then filtered using Ithaco (Models 4032 or 4213) filters. The time delay for the signal coming through an amplifier and a filter was 12 μs (Chan, 1996). Typically, a sampling rate of 50 kHz was used in the experiments with a filter cut-off frequency of 25 kHz. Pressure data were acquired using two LeCroy analog-to-digital (A/D) converters with 12-bit resolution (Model 6810 waveform recorders). The two A/D converters could record up to 8 channels of signals simultaneously at a maximum rate of 5 MHz for each channel. Each A/D converter had 4 megabytes of memory. The A/D converters were pre-triggered:

once the A/D was triggered, the A/D assigned the triggering time as the center of the total data stream, i.e., 4096 data points for each channel, with 2048 data points acquired before and after the triggering time. This made it possible to avoid some synchronization problems due to the electronics and accurately match the timing of the image and pressure signals.

3.4 SHOCK FOOT LOCATION BY PRESSURE MEASUREMENTS

The pressure transducers were flush-mounted on the floor of the test section underneath the intermittent region. The intermittent region denotes the region of separation shock-foot motion. The transducers were placed in the streamwise direction with a spacing of 0.115 inches (2.92 mm). In the analysis of the pressure data the two-threshold method (Dolling and Brusniak, 1989) was used to detect the shock events. With the technique, when the pressure exceeded the upper threshold, the pressure rise was assumed to be due to the upstream passage of the separation shock foot over a given transducer. When the pressure fell below the lower threshold, the shock was assumed to move downstream of the transducer. The upper and the lower thresholds were chosen as $T_{hi} = \mathrm{P}_{\mathrm{bl}} + 6\sigma_{\mathrm{P}}$ and $T_{lo} = \mathrm{P}_{\mathrm{bl}} + 3\sigma_{\mathrm{P}}$ respectively, where P_{bl} was the mean wall pressure of the undisturbed turbulent boundary layer, and σ_{P} was the standard deviation of the pressure signal.

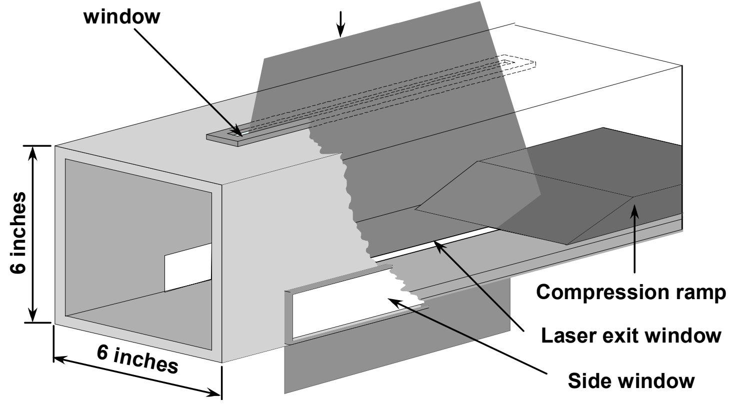

Figure 3.1 Schematic diagram of the test section with compression ramp.

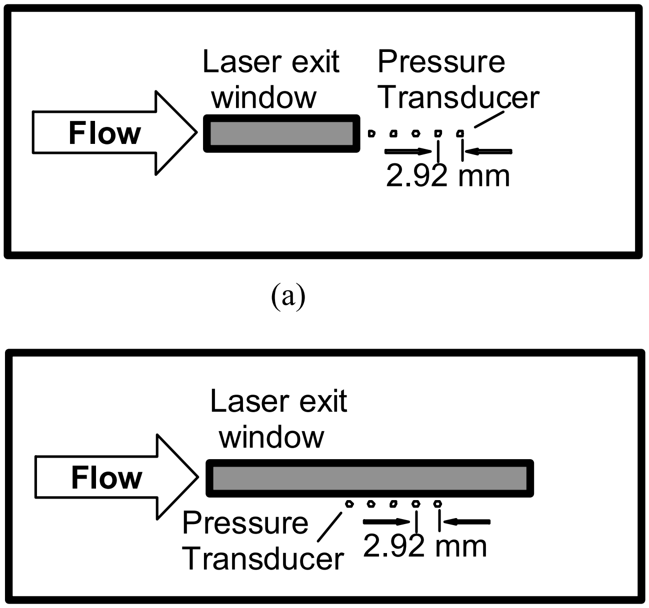

(a)

(b)

Figure 3.2 Schematic diagram of the floor of the wind tunnel showing the laser exit window and the transducer locations: (a) Window in line with transducers; (b) Window parallel to transducers.

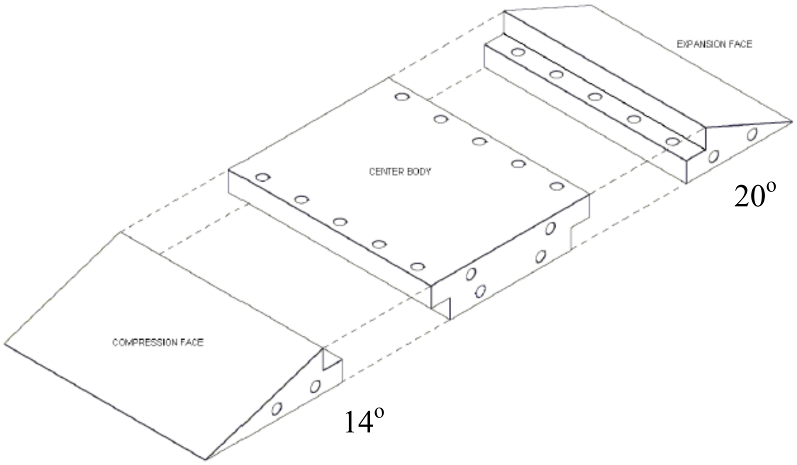

Figure 3.3 Assembly drawing of the 20° and 14° compression ramps.

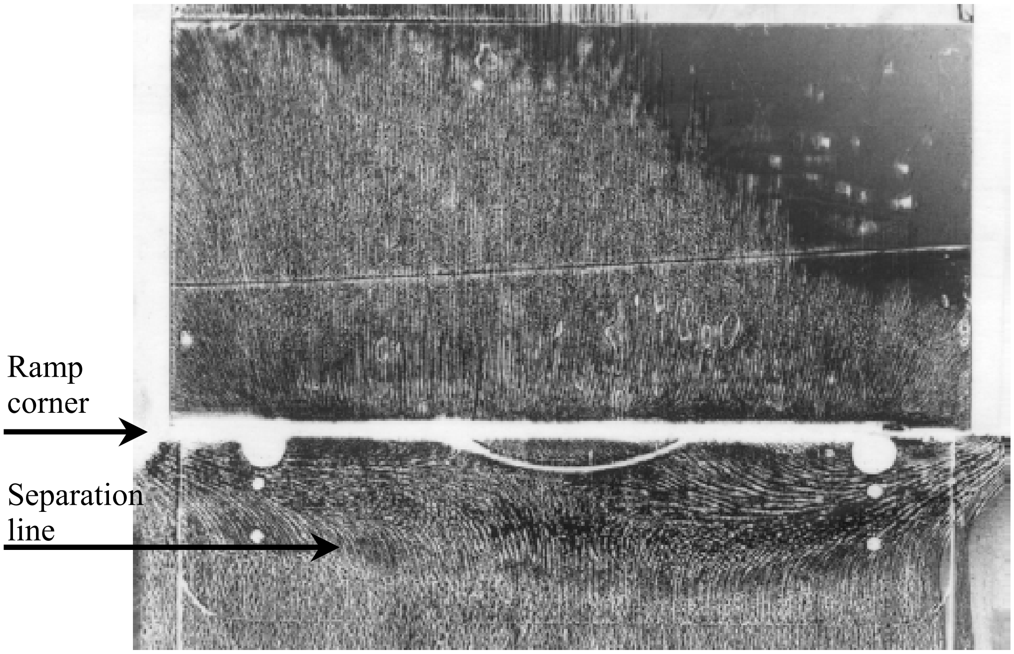

Figure 3.4 Kerosene-lampblack (surface streak line) image for 20°, non full-span, un-swept compression ramp at Mach 2 (Austin 2001).

Chapter 4

Development of a Multi-Camera, Multi-Laser PIV System for Applications in Mach 2 Flows

Modern laser diagnostic techniques have greatly improved our ability to study the physics of shock-induced turbulent separation. PIV is particularly promising because of its relative ease of implementation, high accuracy and good resolution. Although the use of PIV in supersonic flows (Kompenhans and Höcker 1988 and Samimy and Wernet 2000) has not been as pervasive as in subsonic flows, to date it has been applied in a range of complex supersonic flows that include separated base flows (Kompenhans and Höcker 1988 and Molezzi and Dutton 1993), supersonic jets (Alkislar et al. 2000 and Elavarasan et al. 2001), compressible mixing layers (Urban and Mungal 2001), delta wings/airfoils (Lang 1998 and Raffel and Kompenhans 1993), and in supersonic/hypersonic wind- and shock-tunnels (Humphreys et al. 1993 and Haertig et al. 2002). It has been used to study the physics of SWTBLIs, but this has been limited to measurements that were made in the upstream boundary layer, but not in the interaction itself (Beresh 1999, 2002 and Ünalmis 2000). SWTBLIs offer significant challenges to PIV (or any measurement technique) because they are characterized by a wide range of structure sizes, velocity gradients, and time scales. Furthermore, the presence of the shock wave is particularly problematic, because with techniques such as PIV, which require the seeding of particles, the response time of the particles to changes in velocity is a crucial issue. A major limitation of digital PIV is that the field of view is typically limited by the resolution of the imaging array, and this is why mega-pixel arrays (e.g. 1k×1k or 2k×2k) are used almost universally. In the current system, a large field of view is obtained by placing four cameras, each with a resolution of 1k×1k pixels, side-by-side to give an effective resolution of 4k×1k pixels. This large field of view enables PIV measurements to be made of the entire interaction at a single instant in time. The implementation of this PIV system in a Mach 2 SWTBLI is discussed below, with a particular emphasis on the difficulties that are peculiar to using PIV in high-speed flows.

4.1 PARTICLE SEEDING

PIV particles were seeded into the plenum section of the Mach 2 tunnel with the seeder with the fluidized-bed seeder that is shown schematically in Fig. 4.1. The seeder was driven by a flow of nitrogen supplied by a single compressed-gas cylinder connected to the seeder by a ¼ inch stainless steel tube. To enable higher seeding levels, two fluidized-beds were operated in parallel. The particle-laden flows issuing from the two seeders were combined and then passed through a single cyclone separator to separate out all but the smallest particles. The seeders and cyclone separator were constructed from 3 inch diameter, schedule 80 steel pipe that was 31 inches in length. The flow from the cyclone separator was then injected into the main wind tunnel flow at a location that was about 20 inches upstream of the stilling screens that were located just upstream of the stagnation chamber. The particle-laden flow was injected into the main flow by a 3/8 inch stainless steel tube that extended into the main flow. The seeding pressure was typically 180 to 210 psi. A check valve was placed between the seeder and the injection location to keep the main tunnel flow from pressurizing the seeders as this was found to lead to compaction of the particles during tunnel startup. The seeder needed to be cleaned every few runs to maintain good performance.

4.2 DATA REDUCTION AND VECTOR PROCESSING

The PIV processing software used was PivLab developed at Stanford University by Professor Mungal's group. PivLab is Matlab-based and uses a cross-correlation algorithm with adaptive window offset. The adaptive window offset (Westerweel et. al. 1997) greatly improved the accuracy of PIV when the velocities varied greatly across the image. This was expected in SWTBLI because strong boundary layer separation was present. The PIV processing was typically conducted with an initial correlation window size of 64×64 pixels, which was refined by the adaptive algorithm to 32×32 pixels. No overlap in the interrogation windows was used. Since the camera resolution was 1k×1k pixels, the PIV gave a vector resolution of 30×30 vectors for each camera. For wide-field PIV where four cameras are located side-by-side, the vector resolution was 120×30 vectors. Validation of the vectors was accomplished with conventional techniques, which included deleting vectors whose cross-correlations did not meet a sufficient signal-to-noise ratio, and deleting those whose magnitudes and directions varied too much from their nearest neighbors. Typically 95% of all vectors computed in an image were considered valid. After the validation, the holes left by the invalid vectors were filled using a standard linear interpolation scheme.

4.3 PARTICLE SELECTION

Applying PIV in supersonic flows can be challenging because of difficulties in obtaining adequate seeding density (because of the high flow rates required), adequate seeding uniformity, and sufficiently small particles that are able to track the velocity fluctuations of interest. To find suitable particles, a series of experiments was conducted to determine the performance of different types of seed particles. The particles tested were aluminum oxide (Al_2O_3), titanium dioxide (TiO_2) and fumed silica (SiO_2), as shown in Table 4.1. The manufacturers and nominal primary diameters are also given. These tests showed that the TiO_2 particles gave superior uniformity of the seed concentration and superior repeatability of the concentration from run to run. For this reason, the TiO_2 particles were chosen for use in all subsequent validation experiments.

4.3.1 Particle Response

The characteristic response time of the TiO_2 particles was determined by measuring the distribution of velocity downstream of a shock wave (Refell et al., 1998; Urban and Mungal, 2001). As the particles convect through the shock wave, they experience a step change in flow conditions, and the relaxation to the downstream conditions enables one to estimate the particle time constant. Two sets of experiments were conducted to determine the particle response time, one with an oblique shock from compression ramp and the other with the bow shock generated by cylinder.

Consider a particle of diameter d_p, mass m_p and density ρ_p, which is initially moving with a fluid at velocity u_1. The fluid velocity is then instantaneously changed from u_1 to u_2. If the particle experiences a Stokes drag, then the drag force on the particle is given by the relative velocity between the fluid and particle (Melling, 1997):

$$F_D(t) = \frac{3\pi\mu\, d_p^2 \rho_f}{\rho_p(1+Kn)}(u_p(t) - u_2)\,, \tag{4.1}$$

where u_p(t) is the particle velocity, μ and ρ_f are the dynamic viscosity and density of the fluid, respectively, and Kn ($= d_\mathrm{p}/\lambda$, with λ the mean free path) is the Knudsen number. Substituting Eq. 4.1 into the equation of motion, $F_D = m_p\, \mathrm{d}U_p/\mathrm{d}t$, followed by integration, gives the variation of particle velocity with time,

$$\frac{u_p(t) - u_2}{u_1 - u_2} = e^{-\frac{t}{\tau_p}} \tag{4.2}$$

where τ_p is the particle time constant given by (Melling 1997):

$$\tau_p = \frac{d_p^2 \rho_p}{18\mu}(1+Kn)\,. \tag{4.3}$$

The degree to which particles can track velocity fluctuations is quantified with the Stokes number, which is defined as $St=\tau_p/\tau_f$, where $\tau_f = \delta/\Delta U$ is the characteristic flow time scale, ΔU is the characteristic velocity difference and δ is the characteristic width of the flow. The τ_f here is the estimation of the characteristic time-scale of the outer-scale (equivalently, large-scale) structures only. Samimy and Lele (1991) suggested that for particles to faithfully track the velocity fluctuations in a turbulent shear layer, the Stokes number must be less than about 0.5.

4.3.2 Particle Response Measurement through an Oblique Shock

The relaxation of TiO_2 particles as they pass through an oblique shock was investigated with PIV. The oblique shock was generated by a 14^o ramp that was previously shown (with surface flow visualization by Austin 2001) to generate an attached shock. Figure 4.2 shows the experimental configuration that was used for these measurements. Figure 4.3a shows an image of the laser scattering from the TiO_2 particles. The shock can be seen by the increase in density across it, and by the blur induced by the index-of-refraction gradients along the line of sight of the scattered light. In a large ensemble of images, the shock position can be seen to vary from image to image. The reason for this is that the compression ramp was placed on the windtunnel floor, rather than in the freestream, and therefore it was influenced by structures in the thick turbulent boundary layer.

One sample velocity vector field obtained with the titanium dioxide seed particles is shown in Fig. 4.3b. Several streamlines have been included on the figure, from which the flow deflection across the shock can be seen clearly. The velocity vectors, which represent the particle velocity not necessarily the fluid velocity, can be seen to change their deflection angles across the shock and then reach an approximately constant value. The local deflection angle contours are shown in Fig. 4.3c, from which the shock can be seen quite clearly. The shock seems to be thicker at the bottom of the image and get thinner toward the top. The flow deflection angle downstream of the shock reaches an asymptotic value of about 12° rather than 14°, which is the angle of the ramp. The reason for this is that the boundary layer had a substantial effect on the shock at the region where the PIV measurements were made. It appears that the shock had not reached its asymptotic inviscid limit, but was still undergoing compression due to the presence of the boundary layer. One problem with this is that the measurement of the particle response time may be affected, although the effect will lead to the measurement of larger, and hence more conservative, particle response times. The boundary layer also has other effects on the shock, because viewing a large number of such images shows that the shock position and angle can change substantially from image to image.

To calculate the particle response time across the shock, the flow deflection angle along one of the streamlines was extracted, and these data are plotted in Fig. 4.4. An exponential function fit to these flow deflection data gives an e^{-1} length scale of 1.2 mm. In other words, it takes 1.2 mm for the particle to be turned by 63% of the total turning angle. Since the upstream velocity is 500 m/s and the equilibrium velocity downstream of the shock is 420 m/s, the average convection velocity is about 460 m/s, from which we can calculate the "particle time constant" or "response time" τ_p, of about 2.6 μs. (Note that although the deflection angle was used in this analysis for convenience, the relaxation of the *u*- or *v*-velocity would give equivalent results.) Once the particle response time is known, the nominal diameter can be estimated from Eq. 4.1, which gives $d_p \approx 0.26$ μm, if the conditions are taken to be those of the freestream. The particle size is about ten times larger than the manufacturer's specified primary particle size due to agglomeration.

4.3.3 Particle Response Measurement through a Normal Shock

Separate measurements were made by imaging the flow field generated by a Mach 2 normal-cylinder interaction as shown in Fig. 4.5. This was done to see how well the particles could track the flow downstream of a normal shock and to see if mean reverse-flow within the recirculation region could be observed. The cylinder was 0.5 inches in diameter and 2.25 inches in height. The cylinder length-to-diameter ratio was large enough that the interaction generated would be the same as that of a semi-infinite cylinder (Dolling and Bogdonoff 1982). The cylinder rested on a support as shown in Fig. 4.5, which had the same diameter as the cylinder and a height of 0.25 inches.

The structures of the SWTBLI generated by a cylinder and blunt fin are similar, especially along the symmetry centerline. Settles and Dolling (1992) made the following observations: the size of the interaction scales with D; the upstream influence distance is about 2 to 3 diameters; the primary separation occurs 0.5 to 1 diameter downstream of the upstream influence line; the scale of separation depends weakly on Reynolds number, incoming boundary layer thickness and Mach number; Mach number changes the level of the peak pressure but not the shape of the pressure distributions.

The structure of a blunt fin generated SWTBLI can be seen in Fig. 4.6, which shows several figures reproduced from Hung and Buning (1984), Degrez (1981) and Dolling and Bogdonoff (1982). The bow shock causes the boundary layer to separate and this forms a separation shock, which intersects the bow shock at the triple point, creating the familiar λ-shock pattern. Figure 4.6b shows four photographs along the symmetry plane (from Degrez, 1981). The λ-shock is clearly observed in the photographs. The difference among the four photographs demonstrates that the interaction is unsteady. The shock structures along the symmetry plane are further detailed in Fig. 4.6c. A slip line originates from the λ-shock's triple point, and has subsonic flow above it due to the inviscid bow shock and supersonic flow below it that forms a supersonic jet. The supersonic jet impinges on the fin's leading edge and causes severe pressure and heat transfer loads.

Figure 4.7 shows an image of the single-pulse laser scattering from the titanium dioxide particles. The typical λ-shock structure is obvious from the particle image. The bow shock can be identified by the sudden increase in particle density. The separation shock can be seen as the oblique shock originating just upstream of the separation and is represented by the familiar "blur" that was also seen in the oblique shock generated by the 14^o ramp. The blur is not very obvious here because the separation shock is not very strong; however, the shock front appears to be rippled. Little blur can be seen for the bow shock because the shock wraps around the cylinder and so light rays scattered from the particles pass through only a small portion of the flow where the shock is present.

Figure 4.8 shows the mean and two instantaneous PIV vector fields and streamwise velocity contours for the cylinder tests. The cylinder is located on the right side of the figure at x=0. Careful inspection of the vector fields shown in Fig. 4.8a shows the well-known λ-shock structure, which is drawn by hand in black solid lines. The separation shock enters the field of view from the left at about y=8-12 mm, and is detected by the locus of points where the vectors are abruptly deflected upward. Furthermore, Fig. 4 shows strong instantaneous recirculation in the separated flow region as seen at the bottom of the images in the range x=0 to -10 mm. The large differences between the two instantaneous vector fields indicate clearly that the SWTBLI generated by the cylinder is highly unsteady. The mean vector field, shown in Fig. 4.8c, has a relatively clear separated flow region and separation shock but the presence of a bow shock is not clear because the location of the triple point is highly variable due to the interaction unsteadiness. The mean separated flow region is seen to exhibit reverse-flow very close to the wall. This result is very encouraging because it demonstrates the ability of the PIV system to resolve flowfield with large velocity gradients in the same image, including the region of reverse flow.

The response time of the TiO_2 particles is estimated from the normal portion of the bow shock. Figure 4.9 shows three sample streamwise-velocity (u_p) profiles along a streamline passing through the bow shock. In this case the velocity changes substantially downstream of the shock and so in order to estimate the time constant, the temporal relaxation (given by Eq. 4.2) must be related to the relaxation based on the spatial coordinate. This is accomplished by rewriting Eq. 4.2 in terms of the time rate of change of the particle location (x_p) as follows:

$$\frac{dx_p}{dt} = u_2 + (u_1 - u_2)e^{-t/\tau_p} \qquad (4.4)$$

Upon integration of this equation, the time dependence can be removed by solving explicitly for *t* in Eq. 4.4 and substituting this into Eq. 4.2. The resulting formula gives the relationship between velocity and the location of the particle:

$$x_p = \tau_p \left[u_1 - u_p - u_2 \ln\left(\frac{u_p - u_2}{u_1 - u_2} \right) \right] \tag{4.5}$$

A best fit of the PIV data shown in Fig. 4.9 gives time constants that range from 2.6 to 3.2 μs. These values are in good agreement with the 2.6 μs time constant found from oblique shock analysis.

4.3.4 Stokes Number for Mach 2 Turbulent Boundary Layer

The Mach 2 freestream velocity is about 500 m/s and the 99% boundary layer thickness, determined from PIV measurements, is δ_{99}=12.5 mm. Taking the characteristic flow time to be the outer scale time, δ_{99}/U_∞=25 μs, then the Stokes number is about 0.12 (assuming τ_p=3 μs), which shows that the particles easily track the large-scale velocity fluctuations in the boundary layer. In fact, they should track fluctuations with time scales that are about 4 times smaller than this. However, note that there are many smaller scale structures that cannot be detected.

4.4 MULTI-LASER, MULTI-CAMERA PIV

The multi-laser, multi-camera PIV system is shown schematically in Fig. 4.10. This system uses two dual-cavity Nd:YAG lasers (Spectra-Physics PIV-400) that operate at a repetition rate of 10 Hz. Each of the four cavities can be double pulsed, and therefore a total of eight pulses can be generated for the two lasers. When used to deliver 8 pulses, the time between pulses can vary between 30 and 150 μs. At shorter or longer times than these, there is insufficient laser energy per pulse (less than about 20 mJ) for PIV.

The pulse train produced by the lasers, which can range from 2 to 8 pulses, depends on the camera configuration. The four CCD cameras used in the system (Kodak ES1.0) are of the frame-straddling type and have a resolution of 1k×1k pixels. The cameras are synchronized with the lasers at 10 Hz with two frames per cycle. The exposure time for the first frame can be controlled to any length from 1 to 255 μs. The exposure time for the second frame is fixed at 33 ms. The time needed to transfer the first frame and prepare the CCD for the second frame can be controlled at any length from 1 to 5 μs. One PC with one gigabyte of memory controls one camera. Since the image size for each frame is 1 megabyte, each camera can take up to 500 pairs of images, or 50 seconds of data.

This system can be used in three different configurations, which will be described as "wide-field" (4k × 1k pixels obtained by having 4 cameras side by side), "medium-field" (2k × 1k pixels obtained with 2 cameras side by side) and "narrow-field" (1k × 1k pixels, obtained with a single camera). Time sequences can be captured for the medium-field (two-image sequence) and narrow-field (four-image sequence) configurations. The camera setup shown in Fig. 4.10 can be used for medium-field or narrow-field time-sequenced PIV, in which two pairs of cameras are placed on opposite sides of the test section, and each pair of cameras image the flow through a cubic beam splitter.

For wide-field PIV, all cameras image the scattering from the same double-pulsed laser sheets. For the time-sequenced imaging, the lasers produced multiple pairs of laser pulses, and each camera detected a different pair of pulses. Because the ES1.0 camera's second frame exposure time is about 33 ms, the first camera's second frame will also detect the laser pulse that is intended for the second camera. To block the unwanted laser pulses, each camera was equipped with a ferroelectric liquid crystal (FLC) shutter (DisplayTech FLC Light Valve). The FLC shutters were 1 inch in diameter and custom-mounted into C-mount-to-Nikon lens adapters.

A series of experiments was conducted to characterize the temporal response of the FLC shutters. Figure 4.11a shows the experimental setup. The laser light was expanded by a concave lens and scattered from a white card. A camera imaged the scattered light through the FLC shutter. The temporal response was determined by firing the laser at varying delay times with respect to the FLC trigger signal. The FLC was switched either from on-to-off or off-to-on. At each delay-time, the integrated signal computed from the image was normalized by that of the fully open FLC. The resulting FLC shutter response is shown in Fig. 4.11b. The open/close time of the shutters inferred from Fig. 4.11b is about 30 μs and it is this time that sets the minimum time delay that can be used between multi-pair PIV images. Because the ES1.0 cameras are of the frame-transfer type, they offer partial shuttering, and therefore it is only necessary to switch the shutters from open to close. If it were necessary to completely shutter around a laser pulse (i.e. close-open-close) then the minimum time between PIV images would be about

100 μs. (Note that when using the FLC shutters the user should be aware that they can be damaged if they are triggered with uneven duty cycles, i.e., when the open-state period is longer than the close-state period or vice versa). Several pulse-delay generators (Stanford Research Systems DG535) were used to synchronize the system and to trigger the different components. The laser pulses were monitored using a fast photodiode (ThorLabs Inc. DET210) connected to a digital oscilloscope (Tektronix TDS 520C).

Figure 4.12 shows the sample timing-diagram for medium-field time-sequenced PIV. The same idea can be applied to extend the setting to narrow-field time-sequenced PIV.

4.5 ACCELERATION MEASUREMENT

As discussed in Chapter 1, Beresh et al. (2002) proposed that the shock-foot motion may correlate with low-frequency acceleration in the upstream boundary layer. Evaluation of this idea can be investigated by using medium-field or narrow-field time-sequenced PIV. In order to make an accurate measurement of acceleration, the two pairs of cameras must image the same field of view and take images at different times. Then the difference between the velocity fields from different cameras can be used to compute the acceleration. It is obvious that any spatial mismatch between the cameras will introduce a bias into the measurement.

In order to reduce this bias, the fields-of-view of both camera pairs must be matched to subpixel accuracy. This registration process was done by using Insight 3 software from TSI and Matlab's image processing functions. The basic idea was to conduct an *in situ* calibration of the cameras' fields-of-view and use this calibration to correct the PIV images in the post processing stage. The procedure is as follows. Two cameras captured images of the same grid target, a sample of which is shown in Fig. 4.13. The target was composed of equally spaced dots and a single cross in the lower part of the image. The cross served as the origin of the image coordinates. Insight 3 software processes the images of the same target from different cameras by generating equations to map the images to the same physical coordinates. These equations are then used to map the PIV particle images to the same physical coordinates. This procedure corrects for variations in translation, rotation and distortion between the two cameras. The corrected images are then processed by normal PIV processing algorithms.

Measurements in a Mach 2 boundary layer were made to validate the procedure described above. For the first set of experiments the two cameras imaged the particle scattering induced by the same double-pulse laser sheets. The resulting flow fields from the two cameras should be identical if there is no mismatch. A 40 μs time delay between the two cameras was used in the second set of experiments. The resulting acceleration profiles for the zero and 40 μs delay are shown in Fig. 4.14. The mean velocity profile change between 2 cameras with no delay is shown in Fig. 4.14a. This figure shows clearly that the variation in the mean acceleration is small. The range is from -0.25 to -0.1 pixels, while theoretically, the profile should be exactly zero. If we consider the fact that the accuracy of the PIV technique is of order 0.1 pixels, this result shows that the acceleration measurement is limited by the ability to measure velocity itself.

Transverse profiles of the mean rate of change in the velocity (ΔU/Δt) for a time delay of Δt=40 µs, is shown in Fig. 4.14b. Again, the variation is within the range of -0.25 to -0.1 pixels. Several sample instantaneous acceleration (ΔU/Δt) profiles for a 40 µs delay are shown in Fig. 4.14c. The instantaneous acceleration is of order ±1.5 pixels within the boundary layer and about -0.25 pixels in the freestream, which is zero within the precision of the measurement. The acceleration within the boundary layer is over 6 times larger than the system bias error. This indicates that the acceleration measurement is good enough for the purpose of this study.

4.6 EXPERIMENT SETUP

4.6.1 Wide-Field Measurement Setup

Wide field PIV measurements were made simultaneously with fast response pressure measurements under the intermittent region to simultaneously monitor the shock-foot position. The experimental setup is shown in Fig 4.15. For these studies the floor insert shown in Fig. 3.2b was used. Figure 4.16 shows the relative positions of the PIV fields-of-view, pressure transducers and the 20^{o} ramp model. The PIV laser sheet was oriented parallel to the row of pressure transducers, and was offset (in the spanwise direction) by about 4 mm. The laser was single pulsed at a repetition rate of 10 Hz with laser energy of about 40 mJ/pulse. The time delay for each pair of laser pulses was 1 μs. Four cameras captured the same laser sheet but with four adjacent fields-of view. Each camera imaged a region of an area of $21.6\times21.6\ mm^{2}$, to give a total field of view that was

86.4 *mm* long by 21.6 *mm* high. To aid the alignment process, each camera was mounted on an x-y translation stage and a micrometer positioned “tilt” stage.

In this experiment, six channels of the LeCroy analog-to-digital (A/D) converters were used: The first five channels recorded the fluctuating pressure signals and the last one recorded the laser Q-switch signal for the first PIV pulse. A segment of 4096 pressure data points per channel were acquired for each PIV image, corresponding to about 80 ms of data for each image. The A/D converters were pre-triggered.

4.6.2 Acceleration Measurement Setup

Measurements of acceleration were made simultaneously with fast response pressure measurements. In the rest of this dissertation, the term "acceleration" refers to the velocity change over a time period of 40 microseconds and the units are in m/s not m/s^2.

The setup for these experiments is shown in Fig 4.17 and the floor insert shown in Fig. 3.2b was used. Figure 4.18 shows the relative positions of the PIV fields-of-view, pressure transducers, and the 20-degree ramp model. The PIV laser sheet was oriented parallel to the row of pressure transducers. The spanwise distance between the laser sheet and the pressure transducers was about 4 mm. The laser was double pulsed to produce 4 laser pulses in each cycle, at a repetition rate of 10 Hz. The laser energy used was about 40 mJ/pulse. With this setup it was possible to obtain two velocity fields separated by 40 μs from 4 particle images. The timing of the laser pulses is shown in Fig. 4.19. Two cameras, one on each side of the test section, were used with one FLC shutter on each camera. A total of 2770 × 4 images were acquired, which represent 2770 acceleration fields.

In this experiment, seven channels of the LeCroy analog-to-digital (A/D) converters were used: six channels recording the fluctuating pressure signals and one channel recording the laser Q-switch signal for the first PIV pulse. A segment of 4096 pressure data points per channel was acquired for each acceleration field, corresponding to about 80 ms of data for each acceleration field. The A/D converters were pre-triggered.

Table 4.1 PIV seed particles tested.

Particles	Manufacturer (type)	Primary Particle Size	Comments
Titanium Dioxide (TiO_2)	Degussa (P25)	0.021 µm	Time constant was about 2-3 µs; good consistency in performance
Aluminum Oxide (Al_2O_3)	Microabrasives (GB300)	0.3 µm	The best case was similar to TiO_2, but the performance was not consistent
Aluminum Oxide (Al_2O_3)	Degussa (Type C)	0.013 µm	Could not get uniform seeding
Fused Silica (SiO_2)	Degussa (Aerosol 200)	0.012 µm	Could not get uniform seeding

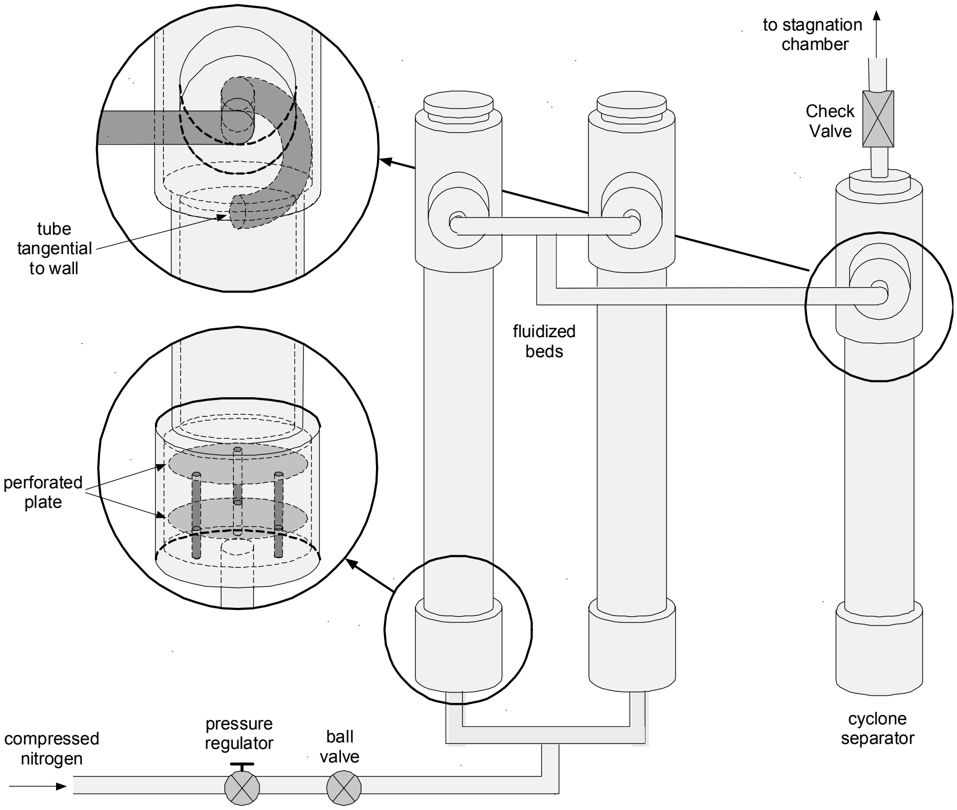

Figure 4.1 Particle seeder for the Mach 2 PIV system.

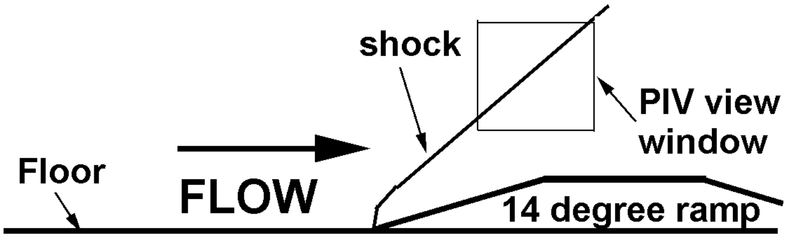

Figure 4.2 PIV field of view for experiments to determine particle response through an oblique shock wave.

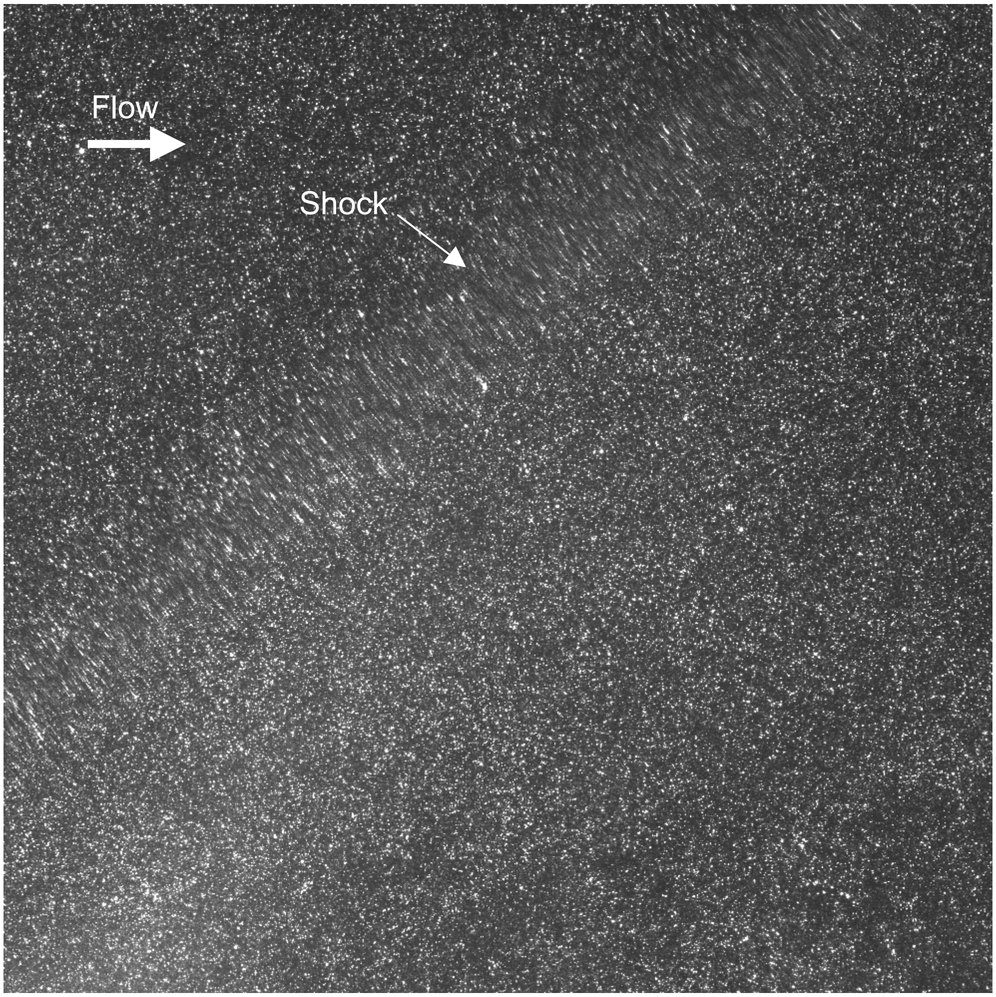

(a)

Figure 4.3 (See caption next page.)

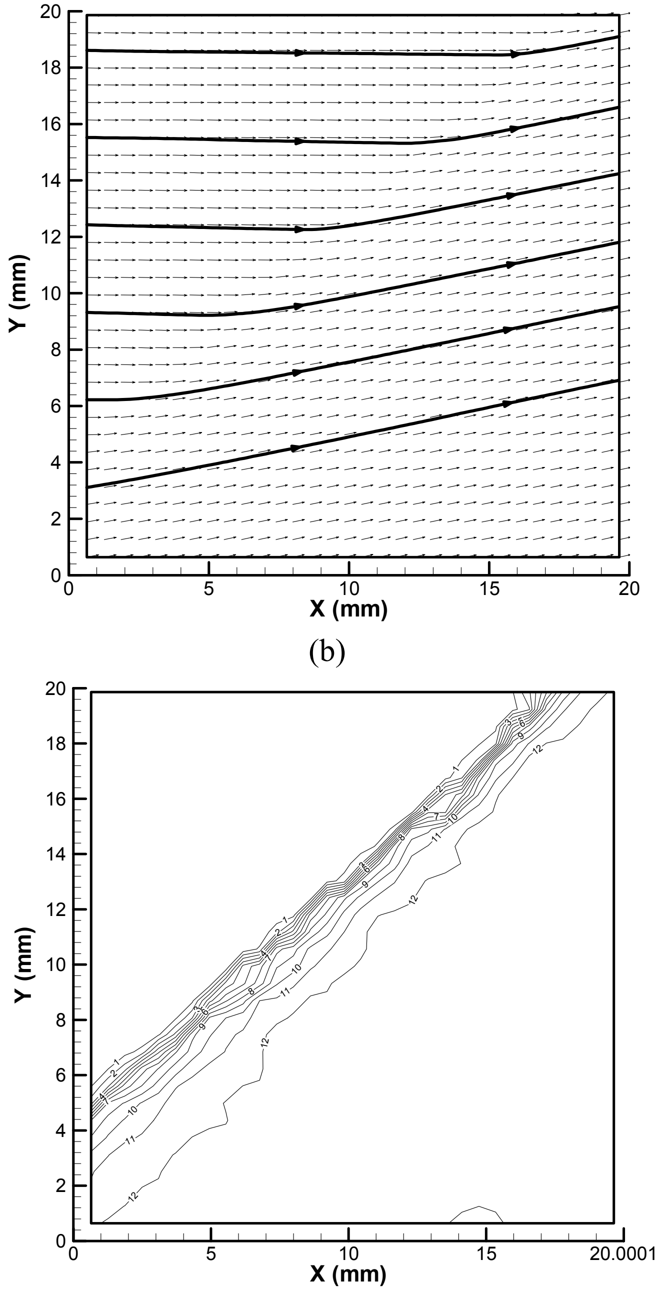

(b)

(c)

Figure 4.3 Sample PIV data for oblique shock tests: (a) single-pulse particle image; (b) PIV vector field with streamlines; (c) flow deflection angle contour plot.

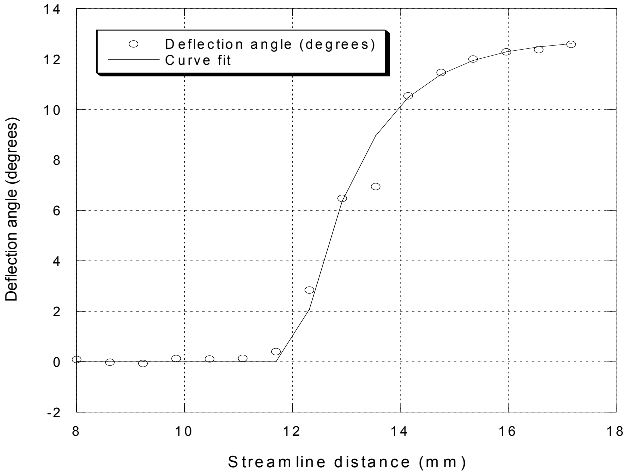

Figure 4.4 Flow deflection angle variations along a streamline near the center of the image shown in Fig. 4.3b.

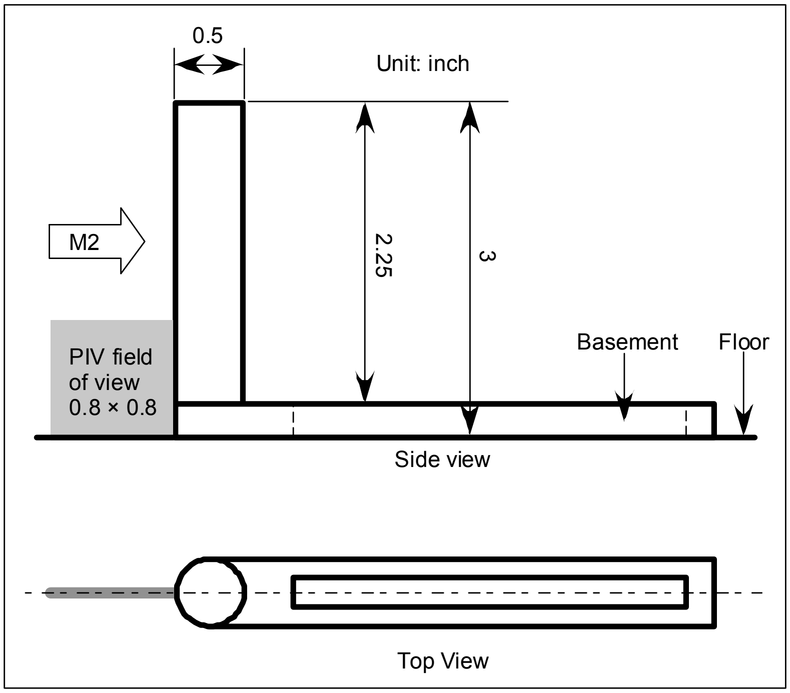

Figure 4.5 Schematic of the Mach 2 normal-cylinder set up.

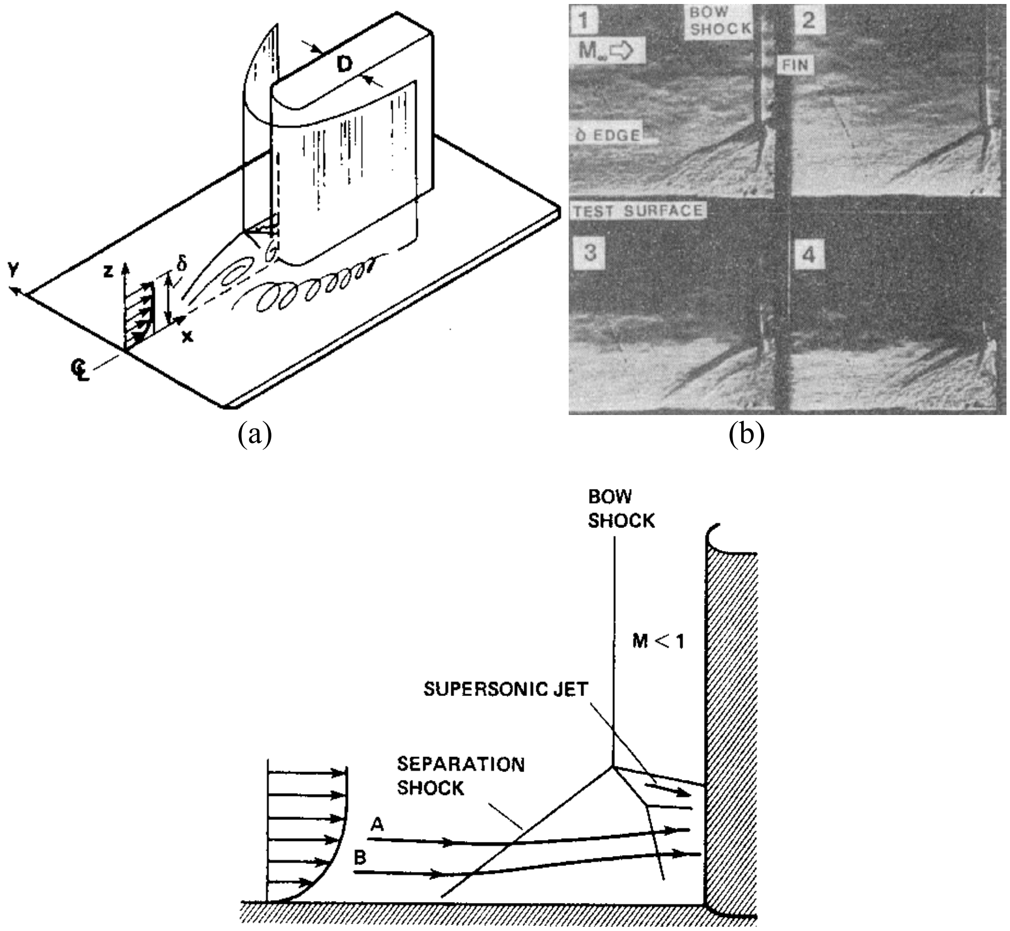

(a) (b)

(c)

Figure 4.6 Blunt fin generated SWTBLI structures: (a) 3-D Model (Hung and Buning 1984); (b) shadowgraph (Degrez 1981); (c) structures on centerline (Hung and Buning 1984).

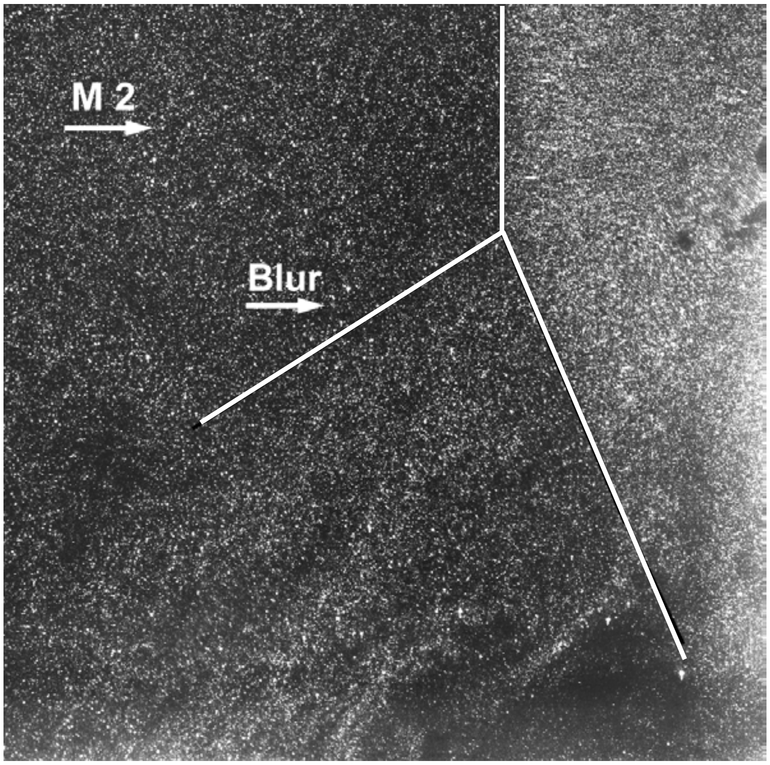

Figure 4.7 Single-pulse particle-image of the interaction generated by a 0.5 inch diameter circular cylinder. The black lines, which identify the presumed shock locations, were drawn by hand.

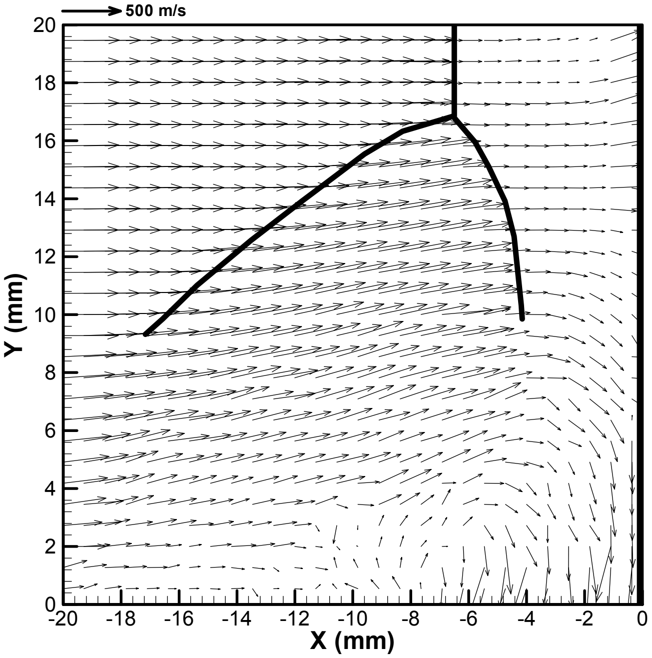
500 m/s
Y (mm)
X (mm)
20
18
16
14
12
10
8
6
4
2
0
-20
-18
-16
-14
-12
-10
-8
-6
-4
-2
0

(a)

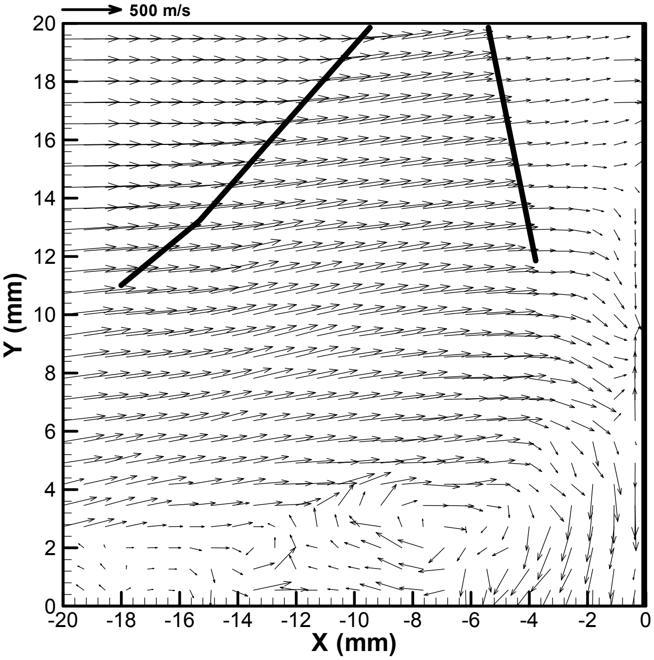
500 m/s
Y (mm)
X (mm)
20
18
16
14
12
10
8
6
4
2
0
-20
-18
-16
-14
-12
-10
-8
-6
-4
-2
0

(b)

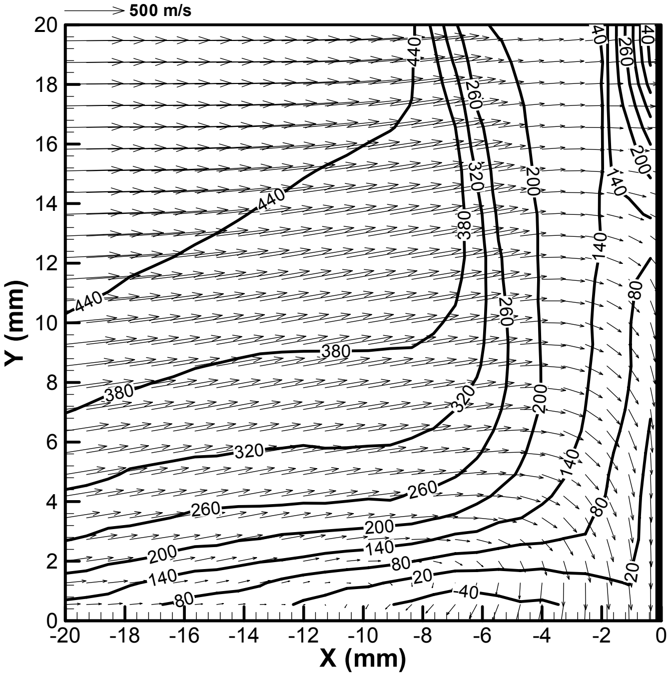

(c)

Figure 4.8 Sample PIV vector fields for the cylinder-interaction: (a), (b) instantaneous velocity-vector fields; (c) mean velocity vectors with superimposed velocity magnitude contour plot.

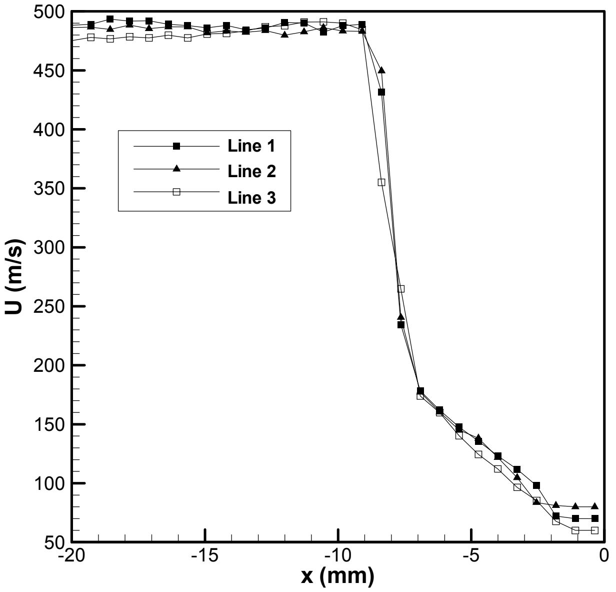

(a)

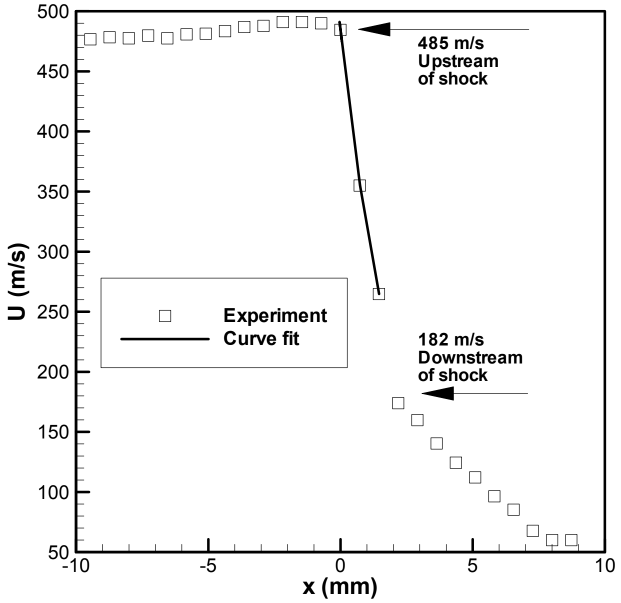

(b)

Figure 4.9 Distribution of U-velocity along a streamline across the normal bow shock generated by the cylinder: (a) three instantaneous cases; (b) curve fit line 3 in (a) to equation 4.5.

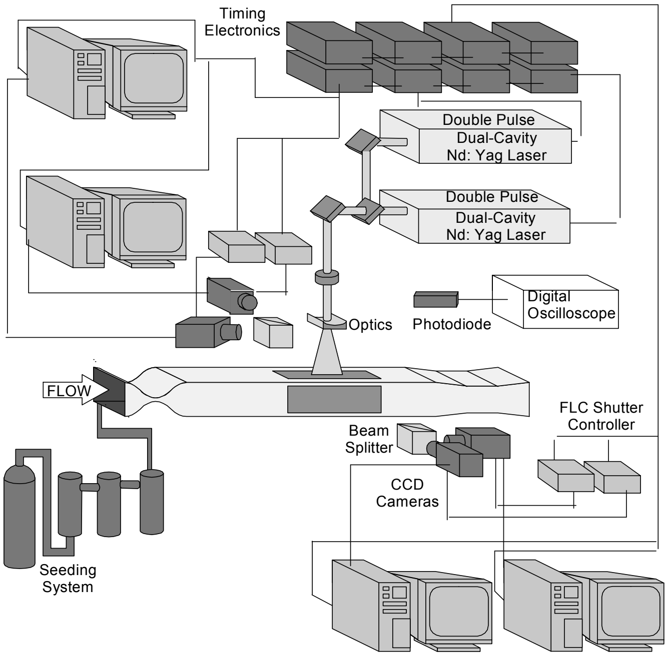

Figure 4.10 Schematic of multi-laser, multi-camera PIV system setup.

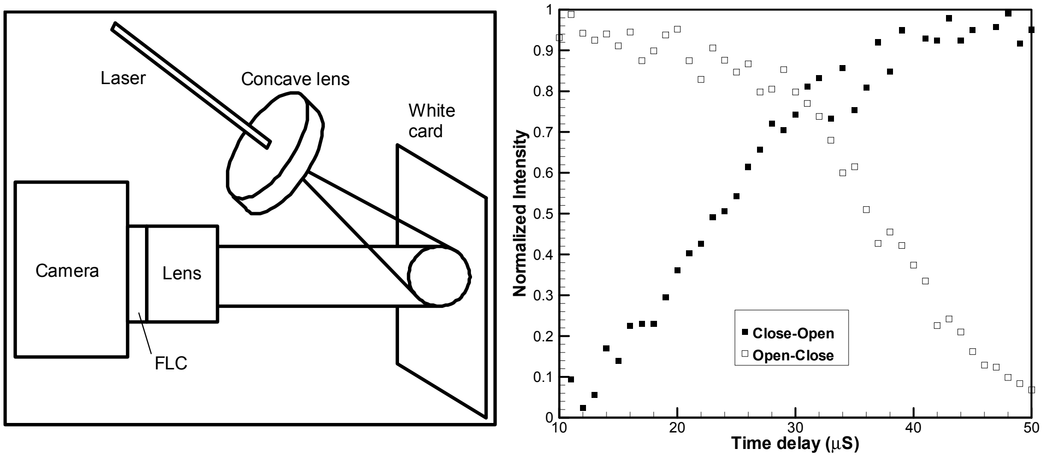

(a) (b)

Figure 4.11 Time response characteristics of the Ferroelectric Liquid Crystal (FLC) shutter: (a) Experiment setup; (b) Time response characteristics.

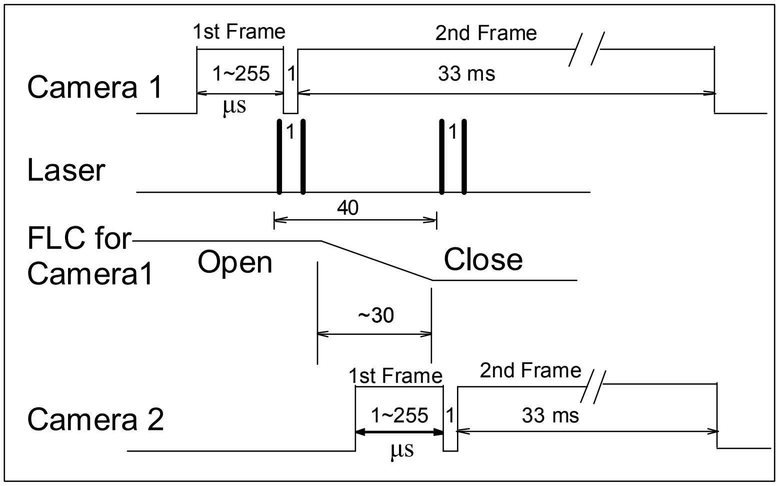

Figure 4.12 Sample timing diagram for time-sequenced PIV (2 PIV pairs).

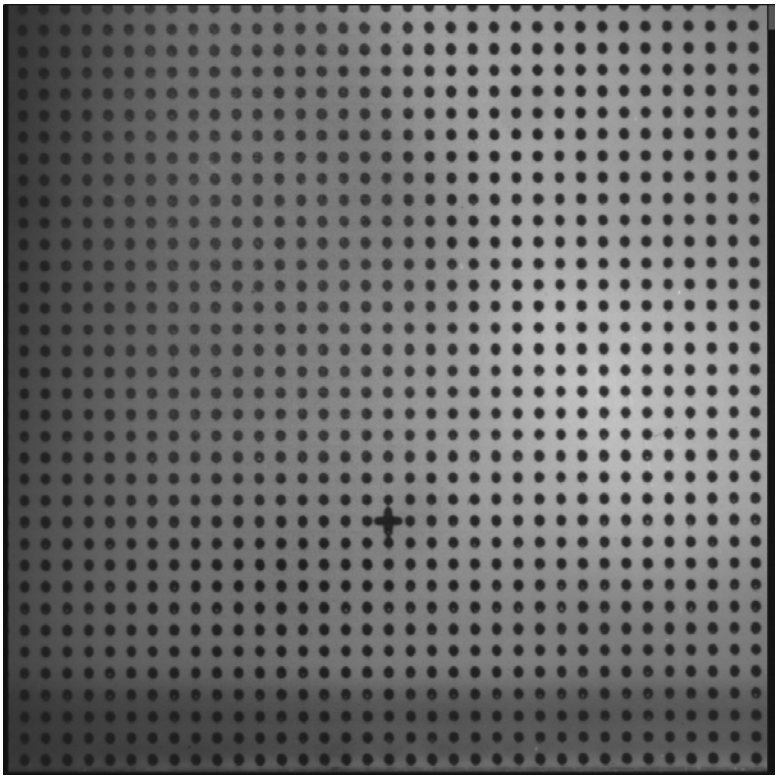

Figure 4.13 Sample "dot card" target image used in the registration of the two cameras in the acceleration measurements.

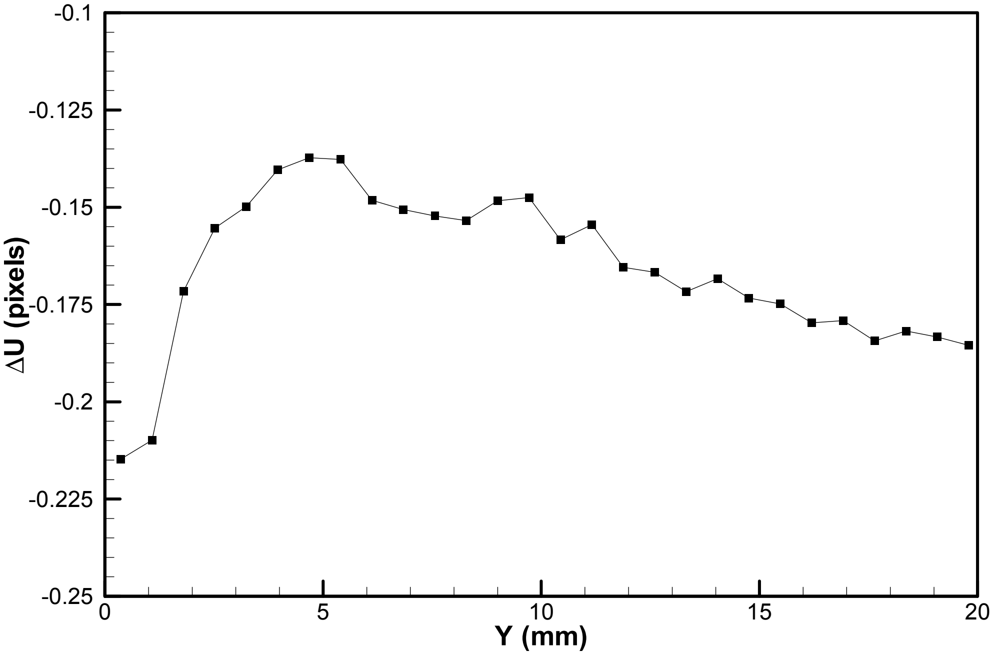

-0.1
-0.125
-0.15
-0.175
-0.2
-0.225
-0.25
ΔU (pixels)
0
5
10
15
20
Y (mm)

(a)

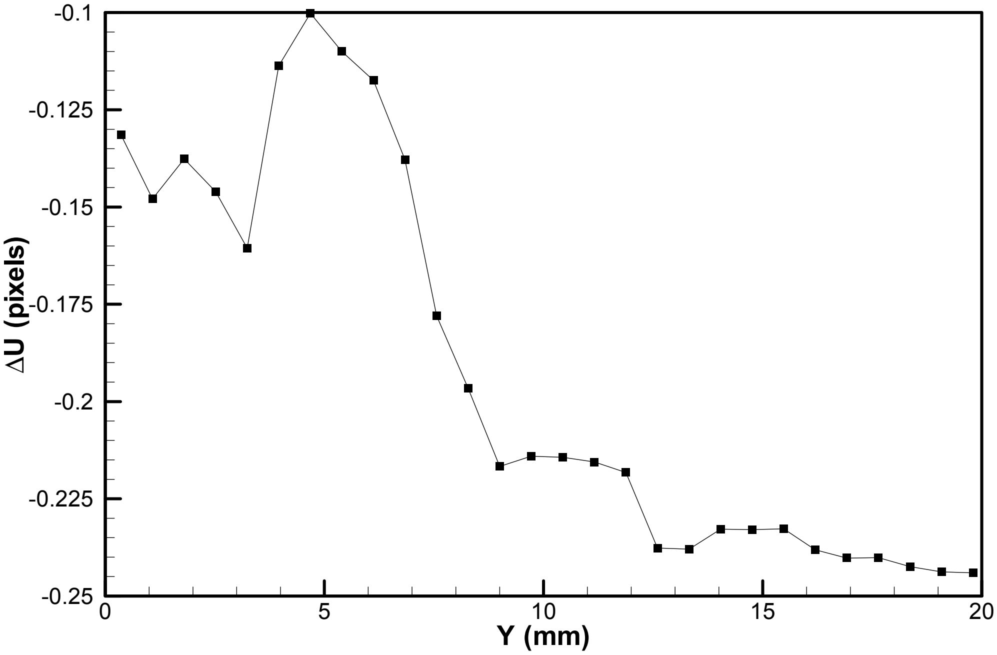

-0.1
-0.125
-0.15
-0.175
-0.2
-0.225
-0.25
ΔU (pixels)
0
5
10
15
20
Y (mm)

(b)

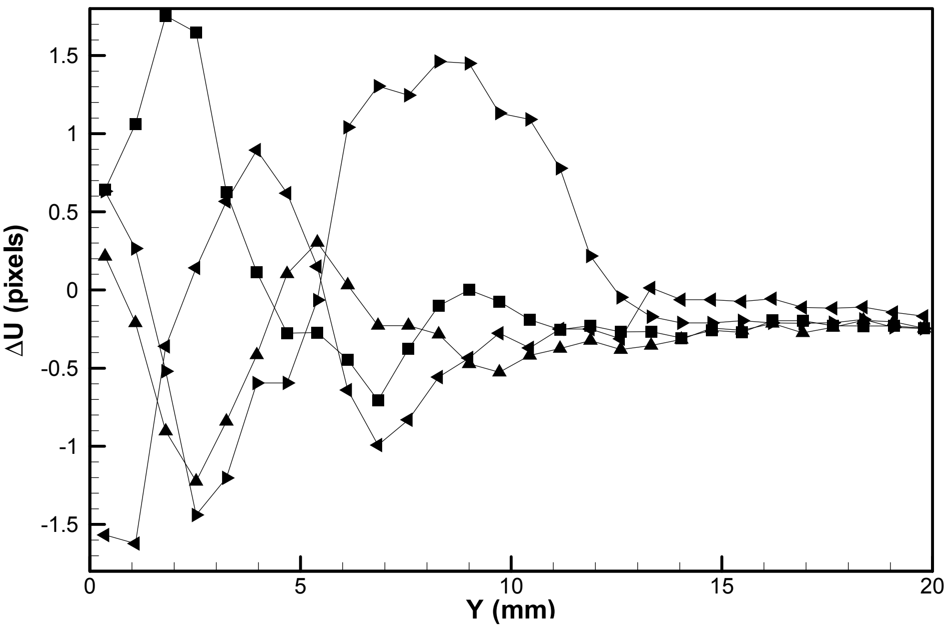

(c)

Figure 4.14 Acceleration profiles for Mach 2 flow: (a) Mean acceleration profiles with no time delay (ideally the profiles should be identically zero); (b) Mean acceleration profile for a 40 μS delay; (c) Sample instantaneous acceleration profiles for 40 μS delay.

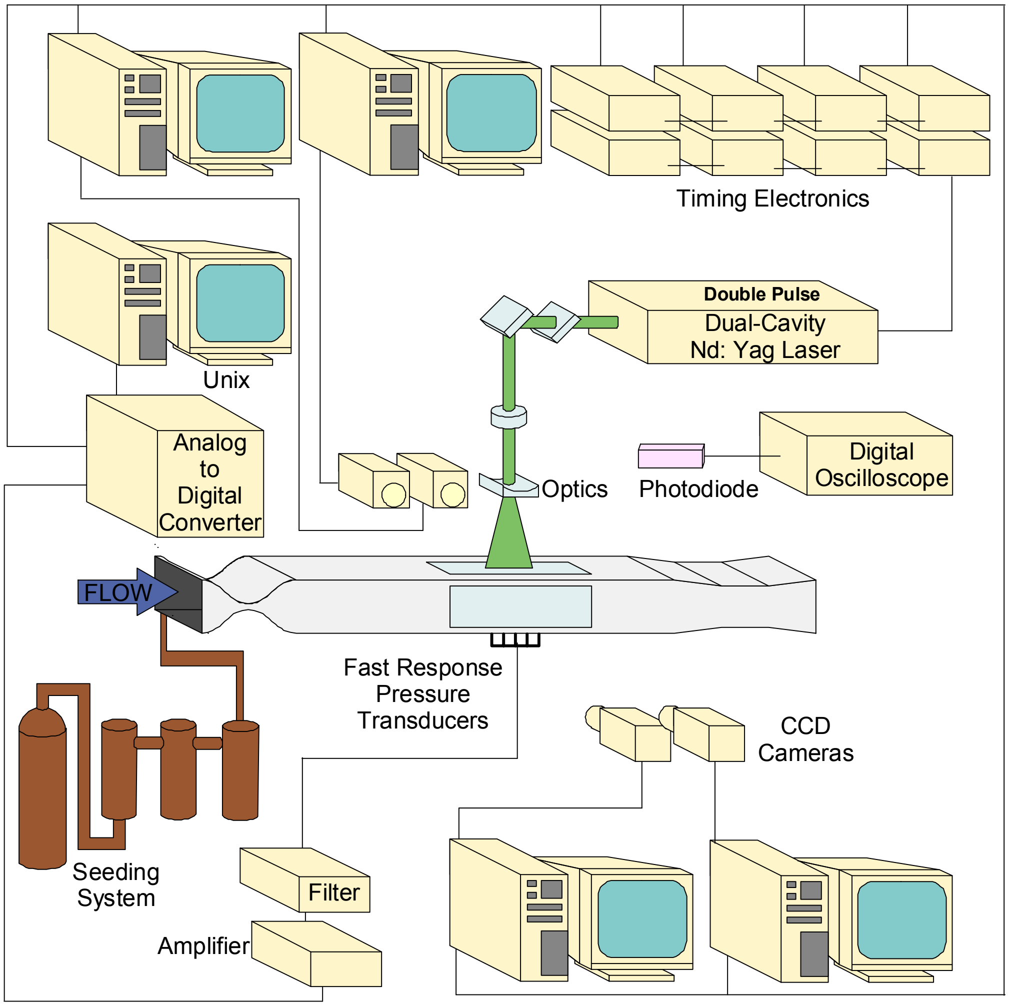

Figure 4.15 Schematic of the wide-field PIV and pressure data acquisition setups.

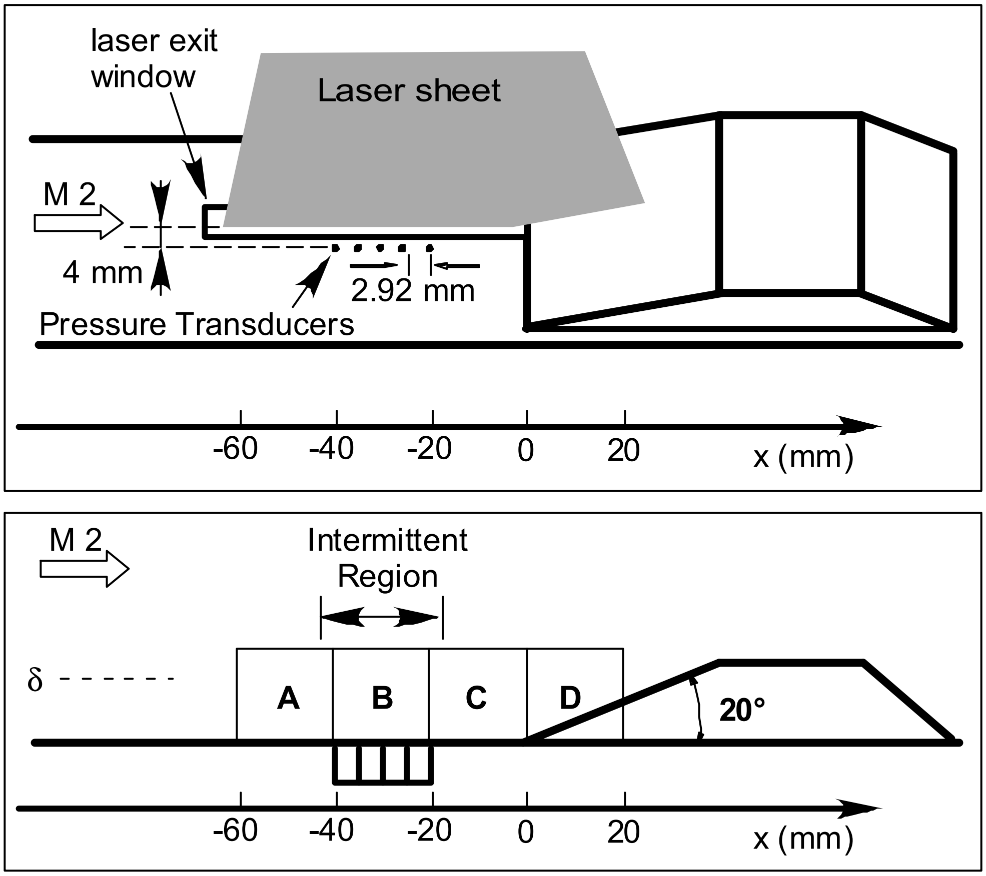

Figure 4.16 Field of view for the wide-field PIV imaging. Five flush-mounted pressure transducers are mounted underneath the intermittent region. The square boxes with letters 'A', 'B', 'C' and 'D' are the cameras' fields of views.

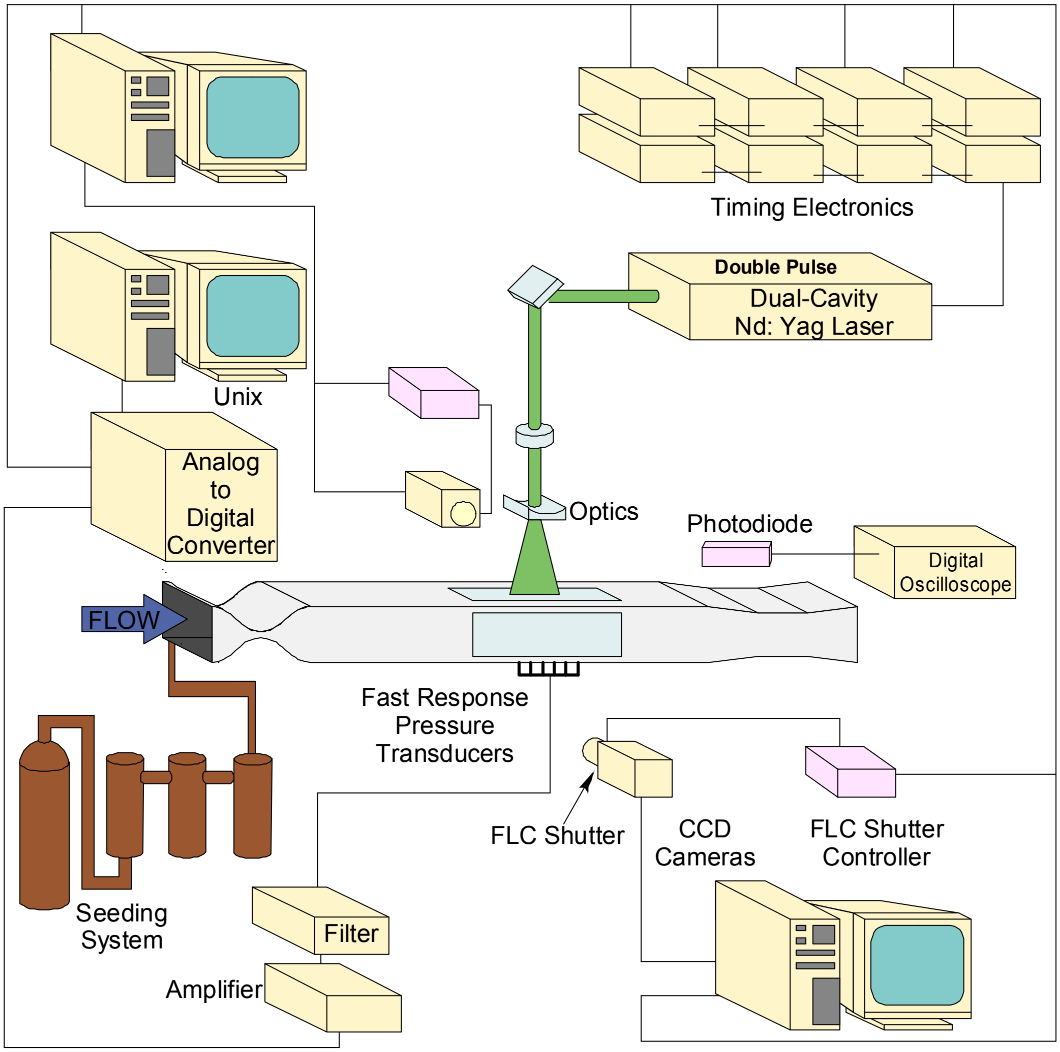

Figure 4.17 Schematic of the time-sequenced PIV and pressure data acquisition setups.

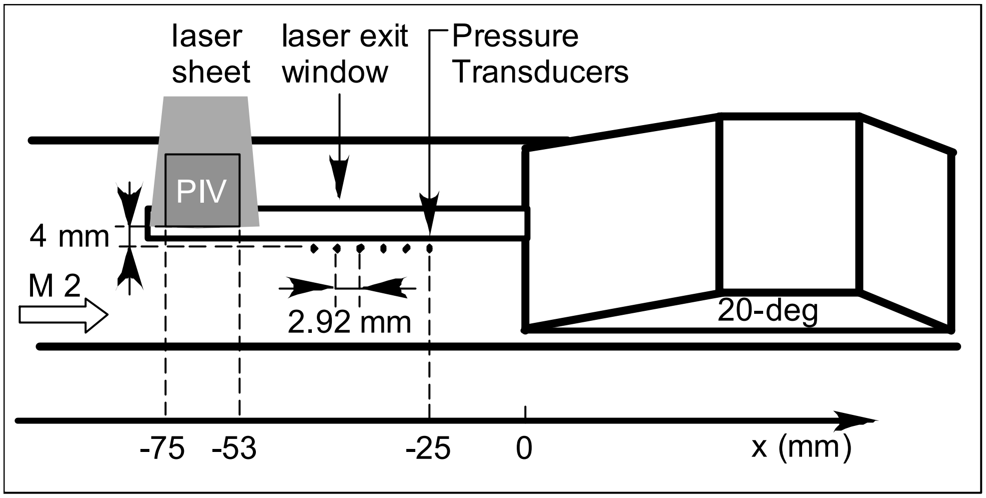

Figure 4.18 Test section setup for acceleration measurement. Six flush-mounted pressure transducers are mounted underneath the intermittent region.

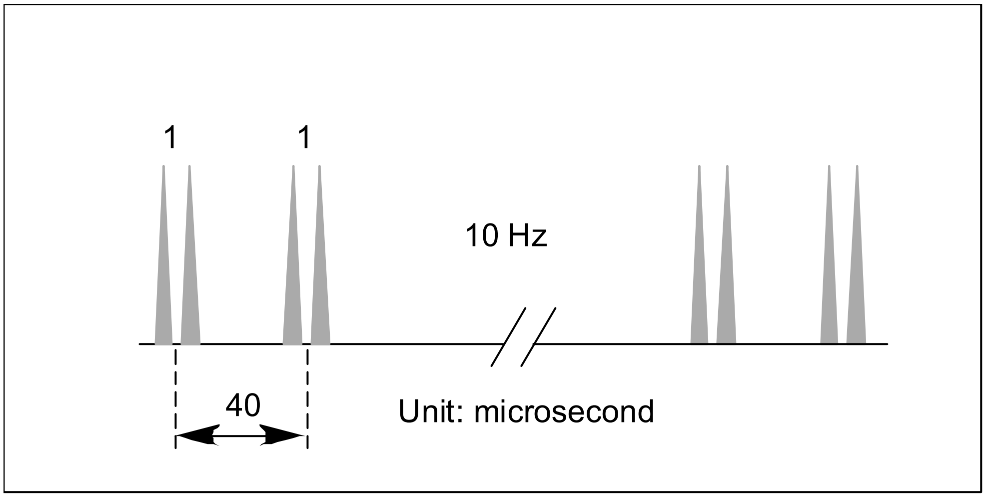

Figure 4.19 Laser pulses pattern for acceleration measurement.

Chapter 5

Mach 2 Boundary Layer Velocity Profile Measurement

The PIV system was used to characterize the undisturbed Mach 2 turbulent boundary layer on the test section floor upstream of the interaction. There were two reasons for this measurement. The first was to document the characteristics of the incoming boundary layer, because this had previously not been done with the current Mach 2 configuration. The second reason was to use the boundary layer measurements, particularly of the fluctuating quantities, as a validation test of the PIV technique in the Mach 2 wind tunnel.

5.1 COMPRESSIBLE TURBULENT BOUNDARY LAYER MEASUREMENT TECHNIQUES

Some of the most commonly used measurement techniques for obtaining the mean properties of compressible turbulent boundary layers include the Pitot tube (Hopkins, et. al., 1972; Horstman and Owen, 1972), hotwire (Spina and Smits, 1987; Smith and Smits, 1993), and laser Doppler anemometry (LDA) (Johnson, 1974; Johnson and Rose, 1975; Yanta and Lee, 1976; Elena and Lacharme, 1988). PIV, like other types of laser-based non-intrusive measurement techniques, has not been widely used in compressible turbulent boundary layer measurements.

Each technique has its own characteristics that need to be considered by the user. Pitot tubes enable the measurement of mean Mach number and combined with a measurement of the total temperature enable the inference of mean velocity. Hotwires can be used for fluctuating (turbulence) measurements however they are not sensitive to velocity alone, but to either mass flux or total temperature depending on how the hotwire is operated. Smith and Smits (1993) derived different equations for the two operation modes and used them to make simultaneous velocity and fluctuating temperature measurements. LDA has the major advantages that it is non-intrusive and sensitive to velocity only. Elena and Lacharme (1988) compared LDA and hotwire measurements in supersonic turbulent boundary layers and concluded that LDA was highly reliable in that environment. They pointed out that LDA should be used for establishing statistics for random fluctuations of velocity and hotwire should be used as a complementary means to obtain statistical information relative to fluctuations in temperature.

Pitot tube, hotwire, and LDA all enable point measurements to be made. The statistical information for each point is obtained by measuring a continuous time-correlated signal with bandwidths of kHz and above. PIV on the other hand gives multi-point, spatially-correlated data, but typically at very low rates (e.g. 10 Hz). The low acquisition rate of PIV is a drawback when computing statistical data because it can be a challenge to acquire sufficient data to produce converged statistics. To achieve large enough data sets for statistical analysis, PIV will typically require substantially longer run times than point measurements. This is particularly problematic for blowdown wind tunnels where data sets from different runs must be combined to produce large enough data sets.

In the current study, combining data from different runs had the additional problem that the total temperature and total pressure varied during each run and from run to run. The changing total temperature causes continuous changes in the sound speed and hence in the velocity (at constant Mach number). The result of this is that the velocity fluctuations calculated without considering this effect will be larger than the real values because the mean used to calculate them is not the real mean. It is easy to prove that a wrong mean value will always yield a larger RMS values. This effect will be further discussed later in this chapter.

Point measurement techniques are more resistant to this problem because the entire data set is usually acquired in a relatively short time, and so the variation in the stagnation conditions is not significant. However, since point measurement techniques need a finite time to move from one location to another, the values at different points are subject to the effects of changing stagnation conditions in blowdown wind tunnels. This effect has undoubtedly contributed to the scatter in the data that have been previously measured in compressible boundary layers.

5.2 MEAN VELOCITY PROFILE

In the current study, PIV measurements were made in the undisturbed Mach 2 boundary layer upstream of the compression ramp interaction. In total, 384 PIV vector fields were used. Each image has 30 x 30 velocity vectors. For each y location (y is the axis that is normal to the test section floor), there were 11520 (384 images × 30 vectors) samples. Only velocities were measured. The temperature profile was calculated from the Crocco-Busemann relation and the density profile was calculated from the temperature profile, assuming constant pressure across the boundary layer. The streamwise velocity profile is shown in Fig. 5.1.

The skin friction coefficient, C_f, is the key parameter to scale the mean and root mean square (RMS) velocities by the inner variables. Thus, attention was first focused on calculating skin friction from the mean velocity profile. White (1991) summarized two classic methods for skin friction calculations: van Driest II (1956) and White and Christoph (1972). Both methods use the same compressibility transformation concept. Bradshaw (1977) compared many such models and concluded that Van Driest II was one of the best methods.

The Van Driest II equations are as follows:

$$C_{fe} = \frac{1}{F_c} C_{f_{inc}} (\mathrm{Re}_{\theta e} F_{\mathrm{Re}_x} F_c) \tag{5.1}$$

where $C_{f_{inc}}$ is the value calculated from incompressible skin-friction formulas and:

$$F_c = \frac{T_{aw}/T_e - 1}{\left(\sin^{-1} A + \sin^{-1} B\right)^2}$$

$$F_{\mathrm{Re}_x} F_c = \mu_e / \mu_w$$

$$A = \frac{2a^2 - b}{\left(b^2 + ra^2\right)^{1/2}}$$

$$B = \frac{b}{\left(b^2 + ra^2\right)^{1/2}}$$

$$a = \left(\frac{\gamma - 1}{2} M_e{}^2 \frac{T_e}{T_w}\right)^{1/2}$$

$$b = T_{aw} / T_w - 1$$

White and Christoph (1972) proposed the following equation to calculate the turbulent skin friction on a flat plate:

$$C_{fe} \approx \frac{0.455}{S^2 \ln^2\left(\frac{0.06}{S}\mathrm{Re}_{xe}\frac{\mu_e}{\mu_w}\sqrt{\frac{T_e}{T_w}}\right)} \tag{5.2}$$

where,

$$S = \frac{\left({T_{aw}}/{T_e} - 1\right)^{1/2}}{\sin^{-1} A + \sin^{-1} B}$$

A and B are the same as those in the Van Driest II method.

One problem with the above formulas is that they depend on the Reynolds number, Re_{xe}, which is not known because the boundary layer develops on the windtunnel floor. For this reason, the model by Sun and Childs (1973, 1976) was used because the parameters required can be obtained from quantities that can be measured or readily inferred. Their model gives mean velocity profiles for compressible adiabatic / non-adiabatic boundary layers. Since there was a printing error in the non-adiabatic formula, the equations are repeated here:

$$\frac{u}{u_e} = \frac{\left(B_1{}^2 + 4A_1{}^2\right)^{1/2}}{2A_1{}^2}\sin\left\{\begin{array}{l}\left[\arcsin\frac{2A_1{}^2 - B_1}{\left(B_1{}^2 + 4A_1{}^2\right)^{1/2}}\right]\bullet \\ \left(\begin{array}{l} 1 \\ +\frac{1}{K}\frac{u_\tau}{u_e^{**}}\left\{\begin{array}{l}\log\eta \\ +\frac{2}{a}\left(1-\eta^a\right)^{1/2} \\ -\frac{2}{a}\log\left(1+\left(1-\eta^a\right)^{1/2}\right)\end{array}\right\} \\ -\frac{\Pi}{K}\frac{u_\tau}{u_e^{**}}\left(1+\cos(\eta\pi)\right)\end{array}\right)\end{array}\right\} + \frac{B_1}{2A_1{}^2}$$

$$C_f = \frac{2(1-\sigma)}{\sigma}\left(\frac{u_\tau}{u_e^{*}}\arcsin\sigma^{1/2}\right)^2$$

$$\frac{\Pi}{K} = \frac{1}{2}\left\{\frac{u_e^{**}}{u_\tau} + \frac{u_e^{**}}{u_\tau}\frac{u_e}{u_e^{**}}\frac{1}{A_1}\arcsin\frac{B_1}{\left(B_1^2 + 4A_1^2\right)^{1/2}} - \frac{1}{K}\log\frac{\delta u_\tau}{\nu_w} + 5.1 - \frac{0.614}{aK}\right\}$$

$$\sigma = \frac{\frac{r-1}{2}M_e^2}{1 + \frac{r-1}{2}M_e^2}$$

$$A_1 = \left(P_{rt}\right)^{1/2}\left\{\frac{\frac{r-1}{2}M_e^2}{T_w / T_e}\right\}^{1/2}$$

$$B_1 = \frac{1 + \left(P_{rt}\right)^{1/2}\frac{r-1}{2}M_e^2}{T_w / T_e} - 1$$

$$u^{**} = \frac{u_e}{A_1}\arcsin\frac{2A_1^{2}\frac{u}{u_e} - B_1}{\left(B_1^2 + 4A_1^2\right)^{1/2}} \tag{5.3}$$

The equations above were used in a least squares fit to the mean velocity data. This fit adjusted the two parameters, δ and u_τ. The equations by White and Christoph (1972) were then used, with the resulting C_f, to obtain Re_{xe}. The parameters for the Mach 2 boundary layer profile are listed in Table 5.1.

The skin friction obtained from the Sun and Childs (1973, 1976) curve fit was further validated by plotting the mean velocity profile scaled by inner variables and "transformed velocity", U^*. The transformed velocity is used because when compressible boundary layer profiles are plotted in classic inner or outer layer coordinates, the profiles do not follow the incompressible scaling laws. However, they do follow the incompressible trend provided the velocity is appropriately transformed (Smits and Dussauge, 1996). Smits and Dussauge (1996) gave the equations for the transformed velocity scaling, which were rewritten by Fernholz based on Cebeci and Bradshaw (1984):

$$\frac{U^*}{u_\tau} = \frac{1}{k}\ln\frac{yu_\tau}{\nu_w} + C^* \tag{5.4}$$

where,

$$U^* = \frac{U_e}{b}\sin^{-1}\left[\frac{2b^2\dfrac{U}{U_e} - a}{\sqrt{\left(a^2+4b^2\right)}}\right]$$

$$C^* = \frac{1}{k}\ln\frac{y_1 u_\tau}{\nu_w} + \frac{U_e}{bu_\tau}\sin^{-1}\left[\frac{2b^2\dfrac{U_1}{U_e} - a}{\sqrt{\left(a^2+4b^2\right)}}\right]$$

$$a = \left(1 + r\frac{\gamma-1}{2}M_e^{\,2}\right)\frac{T_e}{T_w} - 1$$

$$b = \sqrt{r\frac{\gamma-1}{2}M_e^{\,2}\frac{T_e}{T_w}}$$

The suffix 1 here denotes a boundary condition at the lower end of the valid range for the log-law. For an adiabatic wall, U_1/U_e is in the range of 0.3 ~ 0.6, $a = 0$, and $C^* \approx C_{inc}$ (i.e., it has the same value as the incompressible case).

Figure 5.2 shows the Mach 2 streamwise velocity profiles in natural and transformed coordinates. It clearly shows that Fernholz's transformed equations work well for collapsing the compressible data with the incompressible law-of-the-wall profile. The log-law-region in Fig. 5.2 extends to about y^+=3000.

5.3 RMS VELOCITY PROFILE

As stated above, the total temperature decreases during a run and leads to a continuous reduction of the freestream velocity. Figure 5.3 shows how the velocity varied during a run at two locations, $y = 21.4$ mm and $y = 2.0$ mm. Each symbol in the figure is the spatial average of 30 velocity vectors that were obtained at a single instant in time. The time between neighboring symbols was 0.1 second. Figure 5.3 clearly shows that the velocity in the freestream (y=21.4 mm) exhibited a systematic decrease during the run, and it appears that a similar system variation can be seen for the location lower in the boundary layer. This indicates that the computation of the RMS velocities will be affected if the overall mean velocity profile is used. To account for this problem, a "local mean" was used in the RMS calculations. The idea is that for each "y" location, a linear fit is made to the velocity data as shown in Fig. 5.3. Then the linear fit value is used as the "local" mean, and is used to calculate the RMS.

Figure 5.4 compares the u_{rms} results based on the overall mean and local mean. The figure shows that the effect of variable temperature is not large. The u_{rms} near the wall based on the overall mean is almost the same as the one computed using the local mean. The difference increases away from the wall; however, the effect contributes only about 20% to the fluctuations in the freestream. Nevertheless, the u_{rms} values reported in this chapter will be based on the local mean. The v_{rms}, however, is based on the overall mean since the total temperature effect is small on v_{rms}.

The incompressible streamwise velocity fluctuations are typically normalized by $\overline{u'^2}/u_\tau^2$. For compressible boundary layers, Morkovin (1962) suggests the appropriate normalization is $\frac{\rho}{\rho_w}\frac{\overline{u'^2}}{u_\tau^2}$, which takes into account the density variations owing to compressibility. Under this scaling, velocity fluctuations in compressible boundary layers can be made to collapse with incompressible boundary layer data. This scaling has been shown to work well for compressible boundary layers with Mach numbers up to about 5 (Bradshaw, 1977; Elena and Lacharme, 1988; Smits et. al., 1989; Smith and Smits, 1993; Spina, et. al., 1994; So, 1998).

Figure 5.5 compares the current data with the data from other sources. The upper bound and lower bound were measured from Fig. 4 of Elena and Lacharme (1988). Their figure included hot wire data from five sources and LDA data from three sources. The Mach number range was 1.7 ~ 4.7. Figure 5.5 shows that the current data rest just on the upper bound of the other eight sources and is close to the LDA results.

The results from Elena and Lacharme (1988) were measured and plotted together with the current PIV data with Morkovin's normalization scale. They are shown in Fig. 5.6. It shows that the current $\overline{u'^2}$ and $\overline{v'^2}$ profiles agree very well with the Mach 2.32 (Re_θ=4,700) boundary layer result by Elena and Lacharme (1988) who used LDA. Furthermore, the $\overline{u'^2}$ profile is similar to the incompressible and LDA profiles, which emphasizes the validity of Morkovin's hypothesis. It is also seen that the LDA and PIV measurements exhibit a similar

$\overline{v'^2}$ profile. Furthermore, they follow the same shape as the incompressible profile, but have lower values overall.

What may be an interesting feature of the current u_{rms} profile is that it exhibits a "bump" at about y/δ_{999}=0.3. Similar bumps can be seen in other data (e.g. the hotwire data in Fig. 5.6), but they certainly do not appear in all compressible boundary layer measurements, and so it is not clear at this time whether they are physically real. Nevertheless, they appear in enough data throughout the literature to warrant some attention. A brief discussion that suggests a possible reason for this effect is given below.

Figure 5.7 shows streamwise velocity fluctuation profiles measured in incompressible boundary layers with medium to high Reynolds numbers (from Smits and Dussauge, 1996). They stated that there was a tendency for the velocity fluctuations to form a second maximum in a region corresponding to the mean-profile log-law-region, and this tendency was more pronounced as Reynolds number increased. They further state that: "Such second peaks are often observed in high Reynolds number compressible boundary layers (Figures 3.1.1 and 3.1.2 in Fernholz and Finley, 1981), although generally not so pronounced".

Figure 5.8 further compares the current data with other boundary layer fluctuation profiles. The profiles were taken from a plot (Fig. 3.1.1) in Fernholz and Finley (1981). These profiles were measured using hot wires: 58030101 by Kistler (1958) and 78020101 and 78020102 by Kussoy et al. (1978). Figure 5.8 shows that the two Mach 2.3 boundary layers profiles show a bump at y^+=3500. For the current Mach 2 case, the bump starts at y^+=2900. This location is where the log-law-region ends in the mean velocity profile, which is at y^+=3000 (see Fig. 5.2), and so it appears to be the second peak as discussed above.

Table 5.1 Mach 2 boundary layer profile parameters

Parameters	Value	Parameters	Value	Parameters	Value
U_∞ (m/s)	490.8	δ^* (mm)	2.6	P_0 (Pa)	2.62×10^{5}
U_{99} (m/s)	485.8	θ (mm)	0.9	C_f	1.62×10^{-3}
δ_{99} (mm)	12.48	u_τ (m/s)	18.45	Re_θ	3.49×10^{4}
δ_{999} (mm)	16.66	T_0 (K)	270	Re_x	7.31×10^{7}

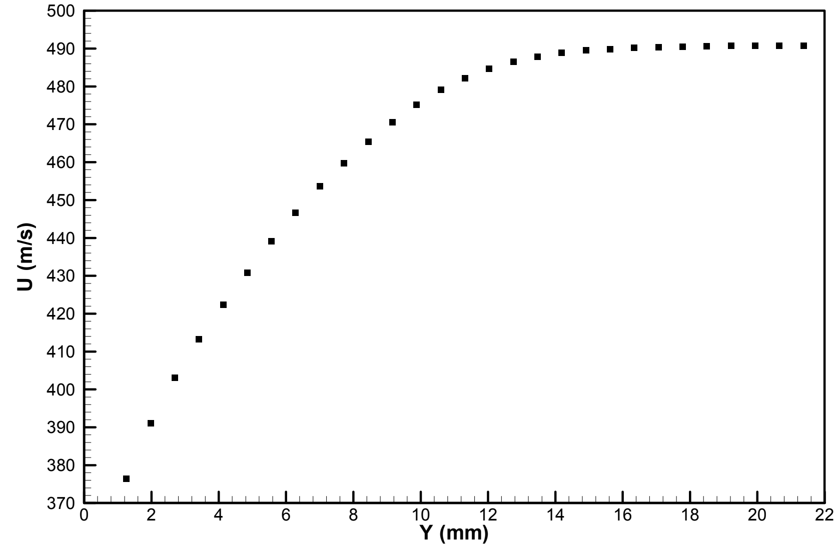

Figure 5.1 Mach 2 mean streamwise velocity profile.

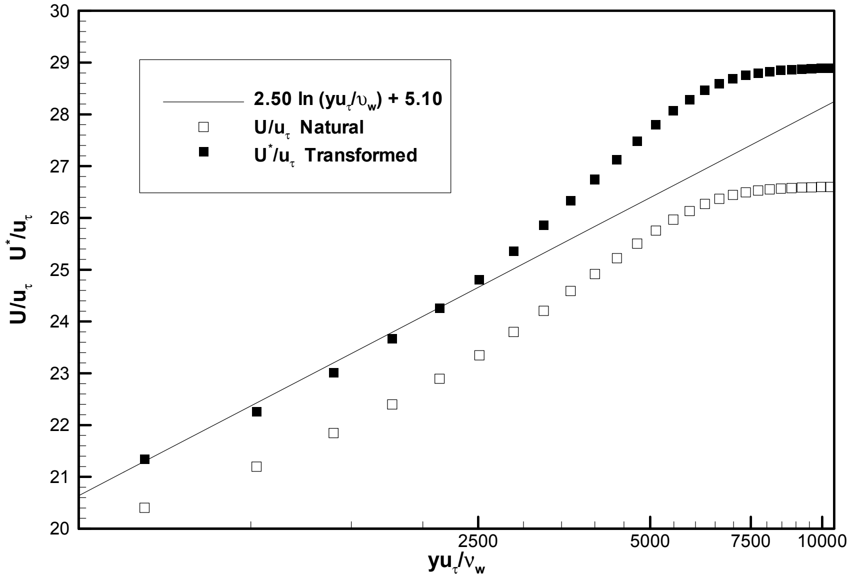

Figure 5.2 Mach 2 mean streamwise velocity profile in natural and transformed coordinates.

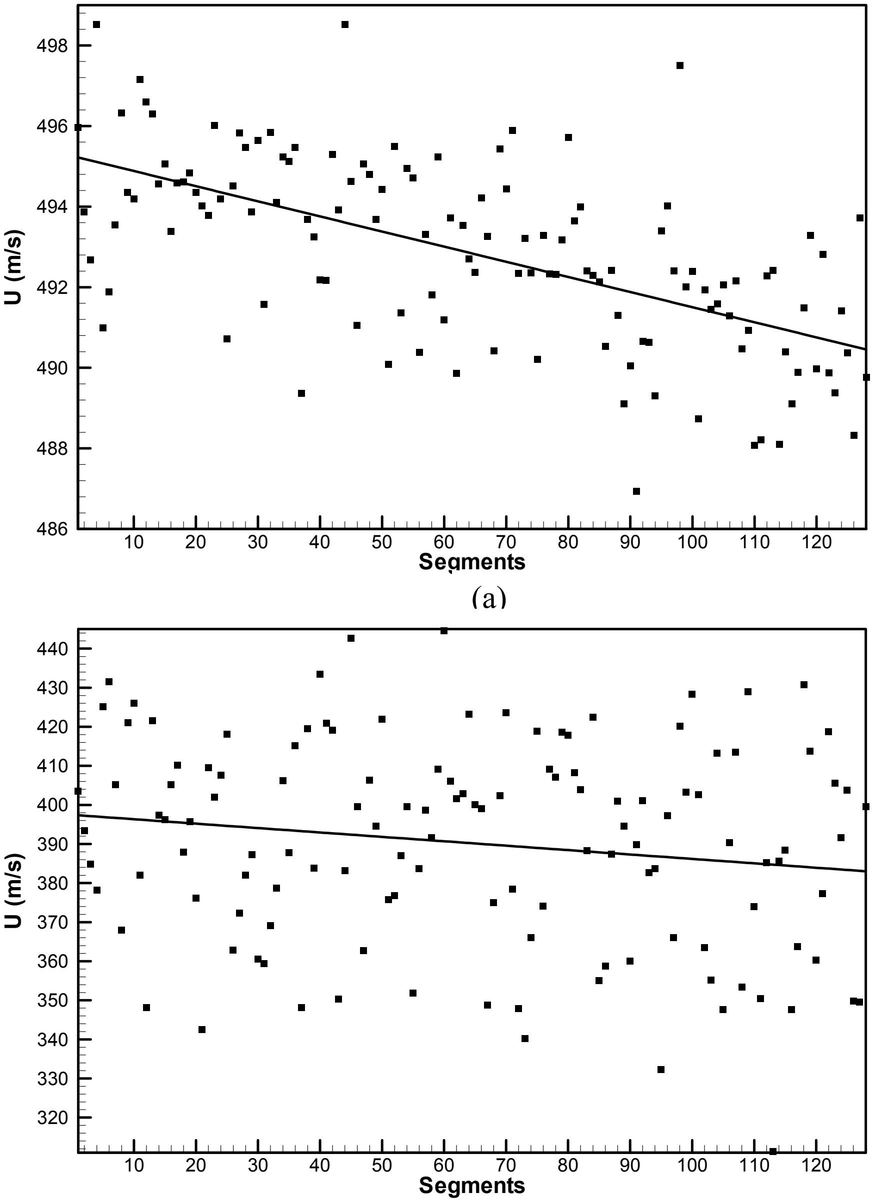

(a)

(b)

Figure 5.3 Variation of streamwise velocity during a single run. Each symbol is the spatial average of a row of PIV vectors at an instant in time. The time delay between each pair of symbols is 0.1 second. The solid line is the linear fit of all the symbols. (a) y = 21.4 mm, (b) y = 2.0 mm.

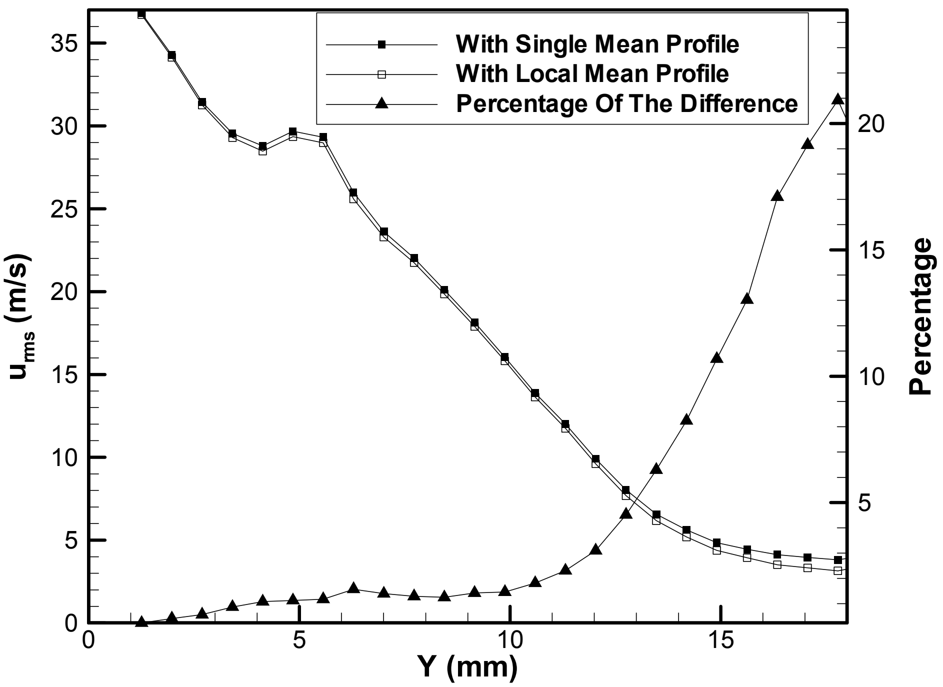

Figure 5.4 Comparison of u_{rms} from total mean profile and local mean profile.

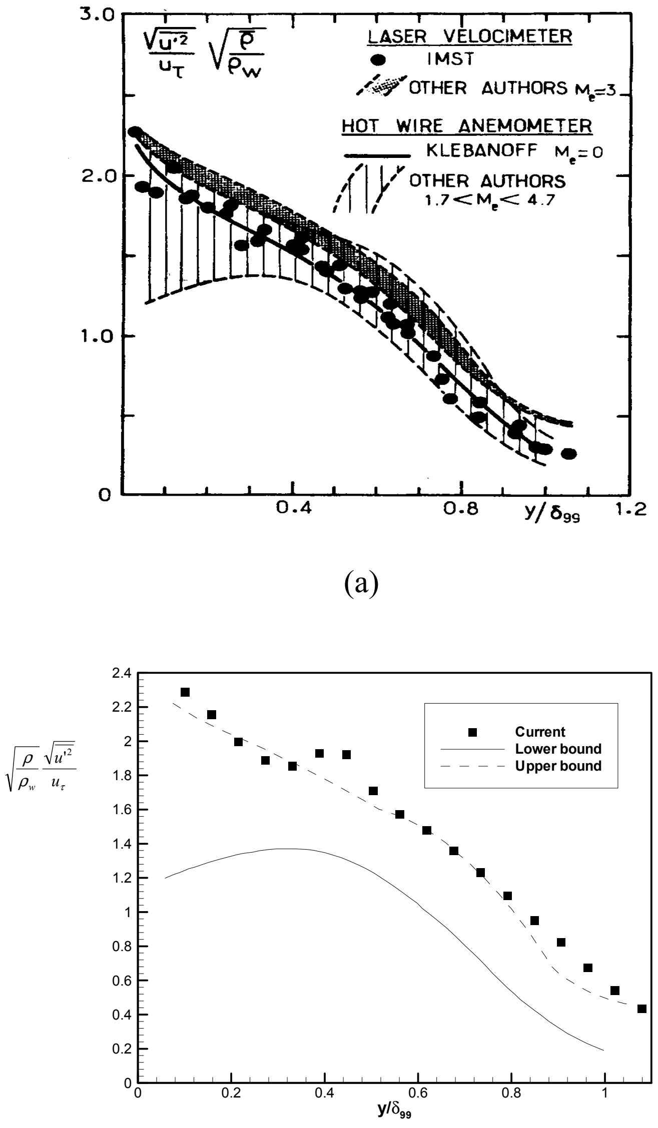

(a)

(b)

Figure 5.5 Comparison of the current data with data from other sources. (a) Elena and Lacharme (1988) Fig. 6, which includes hot wire and LDA data from 8 different sources. The Mach number range is 1.7 ~ 4.7; (b) Current data and the upper / lower bound measured from (a).

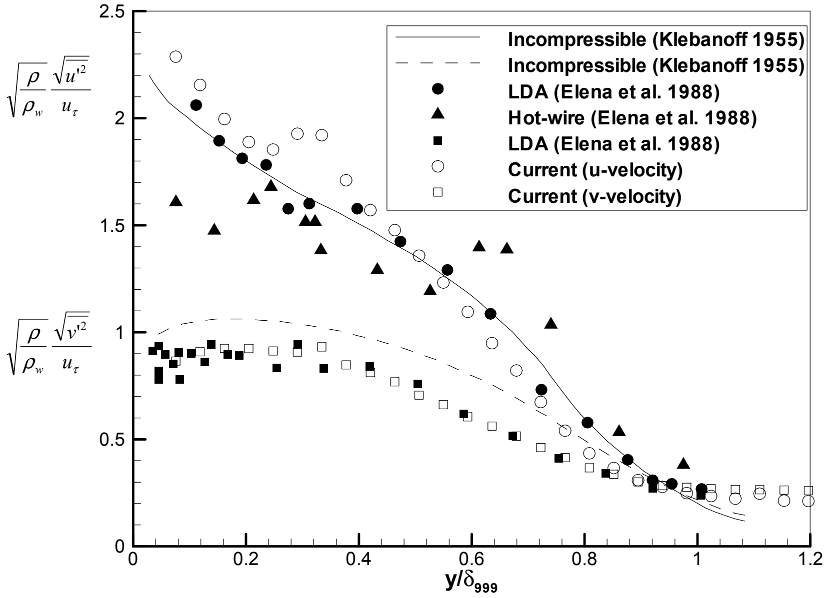

Figure 5.6 Streamwise velocity fluctuations using Morkovin's scaling.

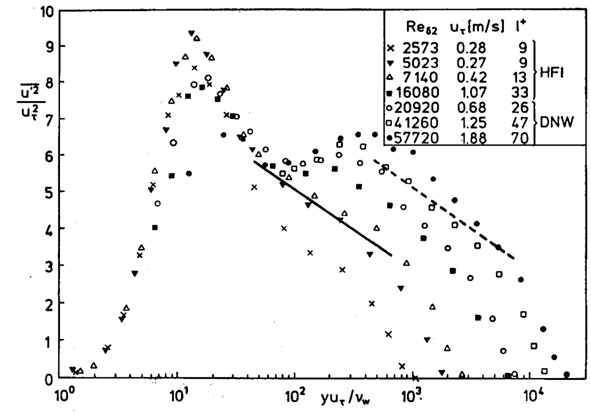

Figure 8.9: Distribution of the longitudinal Reynolds stress in inner-layer scaling at medium to high Reynolds numbers. Data from Bruns *et al.* (1992) and Nockemann *et al.* (1994). ————, Equation 8.14 for $Re_{\delta2} = 5,023$; ---------, $Re_{\delta2} = 57,720$. Figure adapted from Fernholz & Finley (1996) with permission from Elsevier Science Ltd., Oxford, England.

Figure 5.7 Incompressible streamwise velocity fluctuations from Smits and Dussauge (1996)

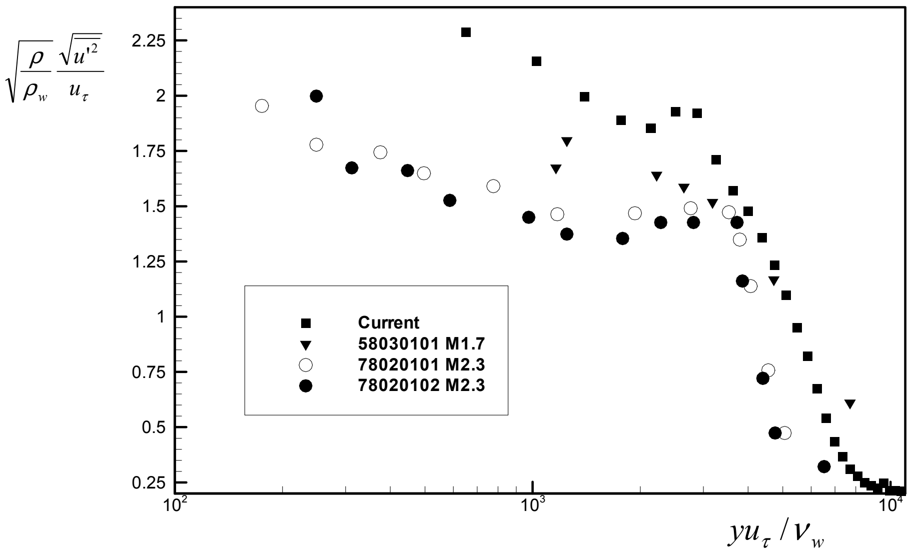

Figure 5.8 Further comparison of the current data with those from other sources. The other data were taken from Fig. 3.1.1 in Fernholz and Finley (1981). 58030101: Kistler (1958); 78020101 and 78020102 by Kussoy et al. (1978).

Chapter 6

Wide-Field PIV Measurement of SWTBLI

6.1 INTRODUCTORY REMARKS

The previous two chapters have shown that the PIV technique employed in this study has been carefully validated and is fully capable of measuring the complex flow features associated with SWTBLIs. In this chapter, wide-field PIV is used to image the entire interaction – covering the upstream boundary layer, intermittent region, separated flow and reattachment region – at an instant in time. The PIV was conducted simultaneously while monitoring the output from five fast-response pressure transducers located underneath the intermittent region. The fluctuating pressure measurements enabled the determination of the shock foot location at the same time that the PIV images were taken. A total of 2000 PIV vector fields were obtained from which a number of statistical quantities were computed. In several cases, conditional averaging was used, in which case averages were computed only for particular shock-foot locations. Unfortunately, it is a relatively rare event for the shock foot to be located near the extremes of the intermittent region (i.e. far upstream or downstream), and so the number of images in those cases was relatively small and thus the statistics computed suffered from significant precision uncertainty. An analysis of the uncertainty is given in Appendix A.

Figure 6.1 shows a composite image of the typical particle scattering fields that are acquired with wide-field PIV. The figure is composed of four images, one from each camera, located side by side. The ramp is in place in this image (seen as the black wedge at right) and the intermittent region is near the center of the image. The upstream boundary layer, whose thickness of about 13 mm is shown on the figure, is seen at the lower half of the composite as a region of less uniform particle density. The separation shock can be seen as a diagonal “blurry” region near the center of the figure. A diagonal white line was drawn “by hand” to help the reader identify the approximate location of the separation shock. The particle density is excellent for PIV, even in what is expected to be the region of separated flow, which should extend from just downstream of the shock until about half a boundary layer thickness up the ramp face.

Note some of the data presented as figures below are attached to the electronic version of this dissertation as “pseudo movies” in animated GIF format. The reason for including the pseudo movies is that they can be a much more effective means of showing the changes in the global structure of the interaction that occur with varying shock-foot location. The simplest way to play those files is to open them in Microsoft® Internet Explorer. Each frame in the movie is a conditional-average plot corresponding to one shock-foot location. There is no meaningful time relation between frames, which is why they are called “pseudo movies”. Two letters, 'SF', marked the shock foot position in the movie. All the frames in the pseudo movies are presented as figures in the dissertation text.

6.2 MEAN VELOCITY FIELDS

Figure 6.2 shows a composite mean vector field extending over the same total field of view as for the particle field composite-image. The mean vector field was obtained by averaging about 2000 vector fields from each of the four cameras. The vertical lines, labeled 1 through 5, mark the streamwise locations of the pressure transducers that were flush-mounted in the wall underneath the intermittent region. The mean velocity vectors within the upstream boundary layer are essentially parallel to the floor until about 30 mm upstream of the ramp where they begin to deflect upward by the separation shock. The deflection by the shock is relatively gradual because the shock is highly unsteady and therefore the mean field smears out any large instantaneous velocity gradients. Downstream of where the vectors begin to deflect, the deflection angle continuously increases and then decreases for locations near the wall, or approaches a constant value for vectors away from the wall. The region just upstream of the compression corner and near the lower wall is expected to be a region of separated flow and indeed the velocity is low in this region; however, no reverse flow is evident. This lack of reverse flow is different from what was measured with LDV by Kussoy et al. (1987) in strong three-dimensional interactions. Note, however, that the mean-flow measurements made by Settles et al. (1976) in the vicinity of a Mach 2.85, 24^{o} compression ramp (shown in Fig. 1.13) indicates that the reverse flow region is very close to the wall. In particular, the major reverse flow region was shown to be a very shallow region extending to about $y/\delta \sim 0.1$. In another study, Müller

(2001) made LDA measurements in an interaction generated by a 24° ramp in a Mach 2.5 flow. Their contours of mean velocity (shown in Fig. 1.2c), indicate that the reverse flow region is about 1 mm from the wall, which is about 1/13 of their boundary layer thickness. Their maximum mean reverse flow was less than 5% of the freestream velocity U. In the current study, if it is assumed that the region of reverse flow will extend to $y/\delta \sim 0.1$, then this corresponds to a y-location that is about 1.3 mm above the wall (since $\delta = 12.6$ mm). In fact, Müller's (2001) results suggest that it may be even smaller than this. Regardless of the exact height of the reverse-flow region, its height is nearly the same as the PIV resolution of 0.8 mm. This means that at the point closest to the wall, the effects of the reversed flow may be averaged out or at least severely attenuated. This effect is probably compounded by the fact that the PIV measurements are also affected by reflections very close to the wall and therefore this region cannot be reliably resolved with these measurements. LDA would be preferred to PIV for this purpose because LDA is less affected by reflections from adjacent surfaces. One other contributing factor to the lack of mean reversed flow is that the compression ramp in the current study is not full span. The finite span ramp can allow some crossflow off the sides, and the "3-D relieving effect" should weaken the interaction and hence the strength of recirculation.

6.3 INSTANTANEOUS VELOCITY FIELDS

Figure 6.3a shows a sample composite image of the instantaneous velocity vector field. The individual images that make up a composite image are taken at the same time, but the different composite images are not time-correlated. A careful viewing of Fig. 6.3a shows that these wide-field images provide a remarkable amount of information about the global structure of the interaction. In the instantaneous images, a relatively abrupt flow deflection, presumably across the separation shock, can be seen in nearly all of the images. To help the reader identify the shock, the locus of points where the vectors first begin to deflect upwards was identified “by eye” and is shown as the solid line in Fig. 6.3a. The shock is not shown extending to the wall because the flow deflection is not easily discerned within the turbulent boundary layer. It is seen from Fig. 6.3a that upstream of the shock, the vectors exhibit very little variation in angle or magnitude, as is expected because the RMS velocity fluctuations in the upstream boundary layer are just a few percent of the free stream velocity. Downstream of the shock, the vectors exhibit substantially more variation. What is presumably the separated flow region can also be seen as a region of low velocity. The likely point of separation is at about x=−30 mm. What appear to be large-scale turbulent structures in the shear layer above the separated flow can also be observed in Fig. 6.3a (e.g. at x=-10 mm; y=6 mm).

The pressure transducer signals were used to locate the shock foot position at the instant in time when the image was taken. For example, Fig. 6.4 shows the pressure time-history for each of the five pressure transducers. The data are shown for a 10 ms interval, and are centered on the time when the PIV image of Fig. 6.3 was taken. The pressure is seen to be relatively high on all but the farthest upstream transducer, but the pressure at transducer 1 is sufficient to be interpreted as a shock event (it must be larger than 6σ, where σ is the standard deviation of the undisturbed boundary layer fluctuations). Careful examination of other similar magnitude pressure “bumps” at transducer 1, together with the other traces, shows that the algorithm did indeed correctly identify a shock event. From these data, it can be concluded that the shock foot is at the far upstream position.

As mentioned above, the five vertical lines, numbered from 1 to 5, mark the positions of the five transducers. A letter 's', which may show up with those 5 numbers, is used to show the location of the shock foot deduced from the pressure measurement. For example, a combination of "1 s 2 3 4 5" means the shock foot was determined to be located between the first and second pressure transducers. In the case of Fig. 6.3a, the letter ‘s’ located to the left of the 1st transducer indicates the shock foot was at its farthest upstream position. It can be seen that the position of the shock foot is consistent with the location of the separation shock that was identified by using PIV.

Interestingly, Fig. 6.3a shows that although the shock foot is located upstream of transducer 1, the point of separation is not until about 10 mm (or about 0.8δ) downstream of the shock foot. This seems to contradict the view (Gramann and Dolling, 1990) that the instantaneous separation point is at, or close to, the instantaneous shock foot location. Careful inspection of a large number of such vector fields reveals cases where the separation point occurs just downstream of the shock foot, but in general it is clear that separation is not always induced directly by the shock foot itself. This may be related to the observation that the pressure rise at the farthest upstream transducer is relatively small when the shock foot is upstream of it, and this may indicate that the shock foot is relatively weak, and hence less likely to induce separation.

It is also observed that the region of "reattachment," which is expected to occur about 5 mm up the ramp face based on mean measurements, is not easily discerned. Taken as a whole, this reattachment region exhibits a wide variation in its structure, and in the majority of images no point of reattachment can be identified. The flow diverges on each side of the reattachment point.

The velocity fluctuation field, computed by subtracting the mean image of Fig 6.2 from the instantaneous image of Fig. 6.3a, is shown in Fig. 6.3b. In the fluctuation fields, the separation shock can often be easier to identify than in the instantaneous fields, because it often appears as a line to which the velocity vectors exhibit a perpendicular orientation. Figure 6.3b shows that the fluctuations are relatively small in the upstream boundary layer, but are substantially larger in the separated flow and in the recovering boundary layer on the ramp face. In fact, Fig. 6.3b shows that the fluctuation vectors downstream of the shock foot are nearly all negative, which indicates that an instant in time was captured when a large slug of low momentum fluid was passing through (or induced by) the interaction.

Figure 6.3c shows the contour plot of *u* (the x-component of velocity) computed from the vector field of Fig. 6.3a. In this figure it can be seen the change in the streamwise velocity across the separation shock is about 10%. This compares to the approximately 30% change that would be expected for a shock generated by a 20 degree wedge in an inviscid flow. This relatively small change in velocity is expected because the separation shock is initially weak, but gains strength by the coalescence of compression waves, and is not the strength of the inviscid shock until well up the ramp face. It can also be observed that the shock foot does appear to cause an immediate reduction in velocity, although boundary layer separation clearly does not occur until farther downstream. Figure 6.3c also shows that the reverse velocities within the separated flow region sometimes exceed 100 m/s, or about $0.2U_\infty$. Such large reverse-velocities occur even though the mean velocity shows no indication of reversed flow.

Figure 6.5a-c shows equivalent sample vectors fields for the case when the shock-foot is at the downstream extent of the intermittent region, i.e. downstream of transducer 5. Figure 6.5a shows the instantaneous velocity vectors, Fig. 6.5b shows the velocity fluctuations and Fig. 6.5c is a contour plot of the *u*-velocity. The presumed location of the separation shock outside of the boundary layer is also shown as the dark line in Fig. 6.5a. The shock is seen to be further downstream than in Fig. 6.5a, which is consistent with what is inferred from the pressure data. One interesting feature of Fig. 6.5 is that the velocity fluctuations are substantially lower than in Fig. 6.3 and there is only a very small (or possibly no) region of separated flow. The *u*-velocity contour plot shows that indeed no reverse-velocities are present in this image. A viewing of many such images indicates that as a general rule, when the shock-foot is downstream, the velocity fluctuations are weaker and the scale of the separated flow is smaller. This observation will be expanded upon below.

6.4 CONDITIONAL MEAN VELOCITY FIELDS

To investigate differences in flow structure with shock-foot position in more detail, ensemble average velocity fields were computed that were conditioned upon the shock-foot location (as discussed in chapter 3). These conditional averages are similar to the conditional LDV measurements of Kussoy et al. (1987).

The conditionally averaged velocity vectors plots for six shock-foot locations are shown in Fig. 6.6. (The animated GIF file, "vector.gif", has the pseudo movies for the plots in Fig. 6.6.) Similar to the unconditional mean velocity vector plot in Fig. 6.2, no obvious reverse flow is detected. The upstream flow is undisturbed with the flow parallel to the wall. The part of the shock in the freestream is indicated by the velocity vector deflection. Careful comparison of the location of the shock in each plot from Fig. 6.6a to Fig. 6.6b shows that when the shock foot undergoes large-scale displacements, the entire interaction is affected. For example, the separation bubble is largest when the shock is upstream and smallest when the shock is downstream (this effect is very obvious in the animated GIF). It is also seen that the angle of the separation shock in the freestream is essentially unchanged with shock-foot location. It appears that the outer part of the separation shock is simply shifted upstream or downstream, and so apparently does not vary in strength. However, this does not mean that the instantaneous shock angle is constant, as can be seen in the instantaneous images.

The conditionally averaged *u*-velocity contours for six shock-foot locations are shown in Fig. 6.7 (the animated GIF file is named "ucontour.gif").

These contours clearly show the flow field is substantially different depending on the location of the shock foot. The region of disturbed flow is clearly larger when the shock foot is upstream. The scale of the ‘separated’ or at least low-velocity flow is also substantially larger when the shock foot is upstream. This is in good agreement with the general concept that a larger separated flow and a farther downstream reattachment distance are present when the shock is upstream. The ensemble averages of Fig. 6.7 also do not show any reverse flow, as was discussed in the previous section. It also appears that the shock foot location inferred from the PIV will agree with the location identified by the transducers provided the 290 m/s *u*-velocity contour line is used. This observation is an *ad hoc* one, as it is not known if the 290 m/s contour has any particular physical significance. The consistency in the shock-foot positions determined by using these two techniques is encouraging, and it also suggests that it may be possible to use PIV only to detect the shock foot location; however, more careful analysis of the PIV-pressure data are needed before this can be done.

Another interesting observation is that systematic differences in the upstream boundary layer seem to be associated with the different shock-foot positions (which again is very obvious in the animated GIF). In particular, it can be seen that the boundary layer is thicker when the shock foot is upstream and thinner when it is downstream. This can be seen by comparing the location of a particular contour line in the upstream boundary layer (say 440 m/s) for different shock-foot locations. More evidence on this effect will be discussed in the following sections.

The conditionally averaged *v*-velocity contours for six shock-foot locations are shown in Fig. 6.8 (the animated GIF file is named "vcontour.gif"). The high transverse velocities are confined to a "V" shaped region downstream of the shock and above the separation bubble. The location where the extension of the 20 m/s contour line meets the wall can be used to indicate the shock location, as this location agrees well with the pressure measurements. The same contour line can be used to demarcate the boundary of the separation bubble, and thus the location where the 20 m/s contour line meets the ramp surface can be viewed as the mean reattachment point. Note that reattachment is not easy to identify from the vector plots shown in Fig. 6.5. Using this definition of the reattachment point, it is seen that a larger separated flow and a farther downstream reattachment distance is correlated to an upstream shock location. This observation is in agreement with the findings of Kussoy et al. (1987).

Figure 6.9 shows conditional-average u_{rms} contour plots for the six shock-foot locations. (The corresponding animated GIF file name is "con_u_rms.gif".) The mean velocity field used to calculate these u_{rms} contour plots is the conditional mean velocity, i.e., it is calculated by averaging velocity fields for the same shock-foot position. This figure shows that the presence of the separation shock substantially increases the magnitude of the fluctuations over those that appear in the upstream boundary layer. This is a well-known effect that is generally regarded as turbulence amplification due to the shock. Figure 6.9 also shows that the domain of elevated fluctuations is clearly larger for the shock-upstream case. Furthermore, as was observed from the instantaneous vector fields, the magnitude of the fluctuations is substantially higher (by about 50%) when the shock-foot is upstream as opposed to downstream. In addition, the domain of elevated fluctuations is substantially larger. The upstream high-fluctuation contour lines cover a bigger vertical distance from the wall for shock upstream than that for shock downstream. This further suggests that the upstream boundary layer thickness is related to the shock location. The relatively larger upstream u_{rms} for shock upstream than that for shock downstream also suggests that the downstream shock is in relatively more stable stage.

Figure 6.10 shows contour plots of conditional-average v_{rms} for shock upstream (Fig. 6.10a) to downstream (Fig. 12f) conditions. The animated GIF file is named "con_v_rms.gif". Similar to the u_{rms}, the upstream shock-foot has substantially higher magnitude of the v_{rms} and substantially larger domain of high v_{rms}. The inviscid shock, which is marked by the 25 m/s vrms contours, is shown again roughly parallel to for different shock locations.

6.5 RELATION BETWEEN UPSTREAM BOUNDARY LAYER THICKNESS AND SHOCK FOOT LOCATION

The conditional upstream (i.e., upstream of x=-45 mm) undisturbed boundary layer velocity profiles based on the shock positions are shown in Fig. 6.11a. Again, the numbers represent the pressure transducers and the letter 's' indicates the shock foot position. It is clearly shown that the boundary layer profile shape changes for different shock positions. The profile has a fuller shape when the shock is downstream than it does when the shock is upstream. The boundary layer thickness calculated from Fig. 6.11a is shown in Table 6.1. The boundary layer thickness is 14.3 mm when the shock is upstream, whereas it decreases to 11.8 mm when the shock is downstream. This shows that the boundary layer is thicker when the shock is upstream and thinner when it is downstream. This is a very intriguing result because it shows that the thickening / thinning mechanism proposed by McClure (1992) and Ünalmis and Dolling (1994) may indeed be correct. Recall that Beresh et al. (2002), in a PIV study, specifically addressed the thickening / thinning mechanism and found that it did not occur in Mach 5 compression ramp interactions. The difference between their study and the present one may be the difference in Mach numbers, but it is more likely to be due to the different particle seeding methods. Beresh et al. seeded their particles into the test section with an intrusive injector, and although they showed that the presence of the injector did not change the shock foot dynamics, it may have affected the correlation with the boundary layer thickness. Their most important observation was that the shock motion is correlated with velocity fluctuations in the upstream boundary layer. This mechanism will be tested with the current data below.

The u_{rms} profiles measured in the upstream boundary layer conditioned upon shock foot locations are shown in Fig. 6.11b. The u_{rms} profiles merge in the freestream, but they exhibit a systematic difference in magnitude for the different shock foot positions. For example, the u_{rms} for the most upstream shock is about 5 m/s larger than that for the most downstream shock. Although the difference is small, the consistent trend from one shock location extreme to the other suggests that it is a real effect. The significance of this observation is not currently known, but it does emphasize the importance of the upstream velocity fluctuations to the shock foot motion.

6.6 RELATION BETWEEN UPSTREAM STREAMWISE VELOCITY FLUCTUATIONS AND SHOCK FOOT MOTION

Beresh et al. (1999 and 2002) measured a relationship between the streamwise velocity fluctuations in the incoming boundary layer and the separation shock foot motion for a 28^o ramp in Mach 5 flow. Specifically, positive streamwise velocity fluctuations in the lower third of the upstream boundary layer correlated with downstream shock motions, and vice versa. As stated above, they used PIV with test-section seeding combined with fast response wall pressure measurements. Ünalmis et al. (2000) found similar results for an interaction generated by a blunt fin in a Mach 5 flow, also with test section seeding.

The current study used plenum particle seeding, and so there was no disturbance to the test section flow. Therefore, we have a good opportunity to check the consistency between the current study and those previous studies. In the current study, the equivalent analysis was conducted, where ensemble average velocity profiles were computed conditioned upon certain types of shock motion: no motion, downstream motion of 1 transducer spacing, upstream motion of 1 transducer spacing. To aid in this comparison, the results of Beresh et al. (2002), Ünalmis et al. (2000) and the current results are shown in Fig. 6.12, Fig. 6.13 and Fig. 6.14, respectively. The current data are not well suited for this purpose because the sample size for the conditional cases, which are shown in Table 6.2, was quite small, and it is this limited sample size that made it impossible to include results for shock sweeps of two or more transducer spacings.

Nevertheless, the data shown do exhibit consistent trends, indicates the velocity-fluctuation/shock-motion correlation proposed by Beresh et al. (2002) is indeed correct, and may be universal since it also occurs in Mach 2 interactions.

The significant velocity fluctuations occurred within 70% of the boundary layer in the study of Beresh et al. (2002) and within the whole boundary layer in the current study. The difference may due to the Mach number difference, i.e., Mach 5 for Beresh et al. (2002) and Mach 2 in the current study. Another possible reason for the difference is that the current study had much less number of data in the ensemble average so that the profiles in the current study converge slowly. The reason, however, is more likely caused by the different seeding methods. Beresh et al. (2002) used test section seeding, which introduced disturbance in the upstream of the interaction, as a result, decoupled the boundary layer profile changes from the interaction.

One interesting further observation can be made when comparing the profiles in Figs. 6.12-6.14. In all three experiments the magnitude of the velocity fluctuations when the shock moves upstream is larger than when the shock moves downstream. For example, in Fig. 6.12b, the velocity fluctuations for a shock moving upstream 3, 2 and 1 transducers are -22 m/s, -11 m/s and -4 m/s, respectively, whereas the fluctuations for a shock moving downstream 3, 2 and 1 transducers are 16 m/s, 5 m/s and 0 m/s. The velocity fluctuations follow the same trend with the direction of shock motion for both the blunt fin and Mach 2 compression ramp. Despite the relatively large uncertainty of these measurements, the presence of this effect in three independent studies suggest that it is real. The reason for this asymmetry is not known, but it suggests that there is a greater resistance to shock-upstream motions and therefore a larger velocity fluctuation is required to move the shock upstream. These comments at this time are purely speculative, but this may be an interesting effect that can be investigated in future studies, or perhaps with numerical simulation data.

Table 6.1 Boundary layer thicknesses as a function of shock-foot position.

Shock Position	Freestream U_∞ (m/s)	Boundary Layer Thickness δ_{99} (mm)
s 1 2 3 4 5	486.3	14.3
1 s 2 3 4 5	485.0	14.1
1 2 s 3 4 5	486.0	13.1
1 2 3 s 4 5	486.1	12.6
1 2 3 4 s 5	486.4	11.9
1 2 3 4 5 s	484.7	11.8

Table 6.2 The numbers of segments obtained for each shock motion.

	1.9 kHz (520 μs window)	5 kHz (200 μs window)	8.3 kHz (120 μs window)
Upstream 2 pressure transducers	78	18	4
Upstream 1 pressure transducers	344	268	181
No motion	494	960	1160
Downstream 1 pressure transducers	283	227	170
Downstream 2 pressure transducers	56	15	4

.

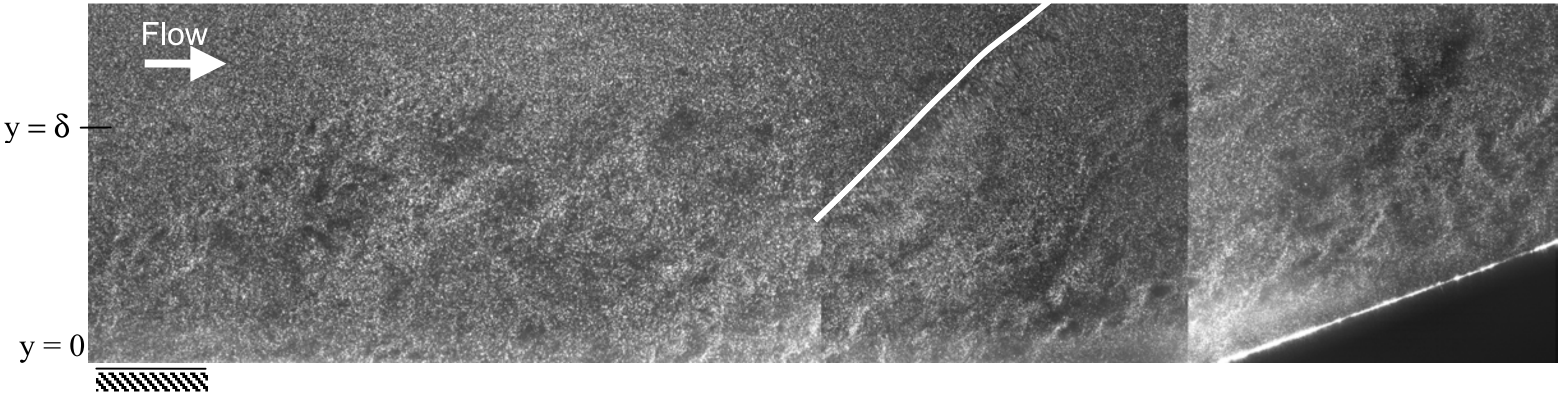

Figure 6.1 Sample four-image composite of single-laser-pulse particle scattering. The approximate location of the shock inferred from the blurring of the particle image is shown as the 'hand drawn' white line.

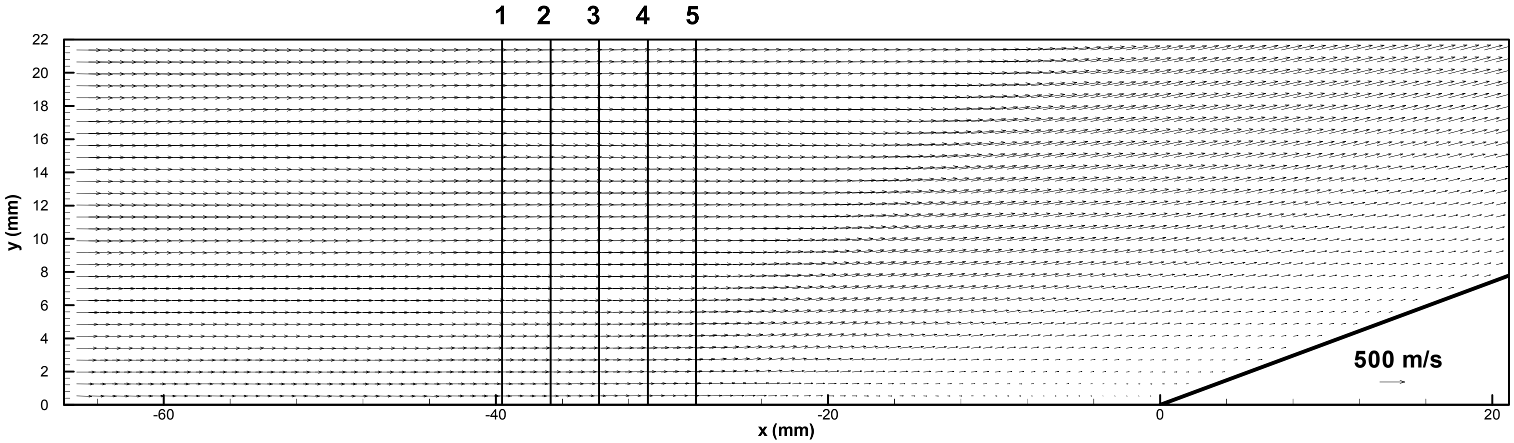

Figure 6.2 Composite mean velocity vector-field for the 20-degree ramp obtained by wide-field PIV.

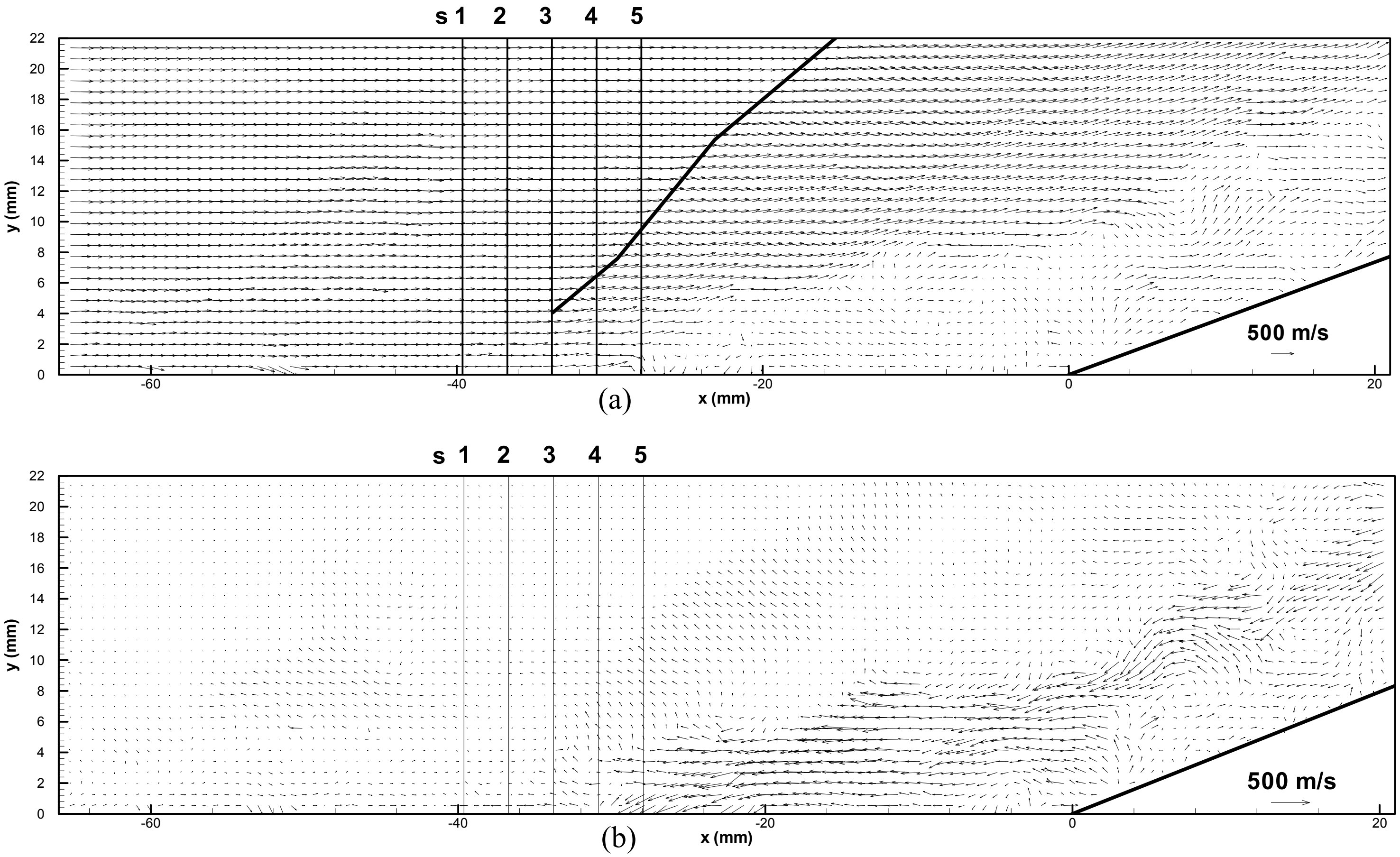

(a)

(b)

Figure 6.3 (See caption next page.)

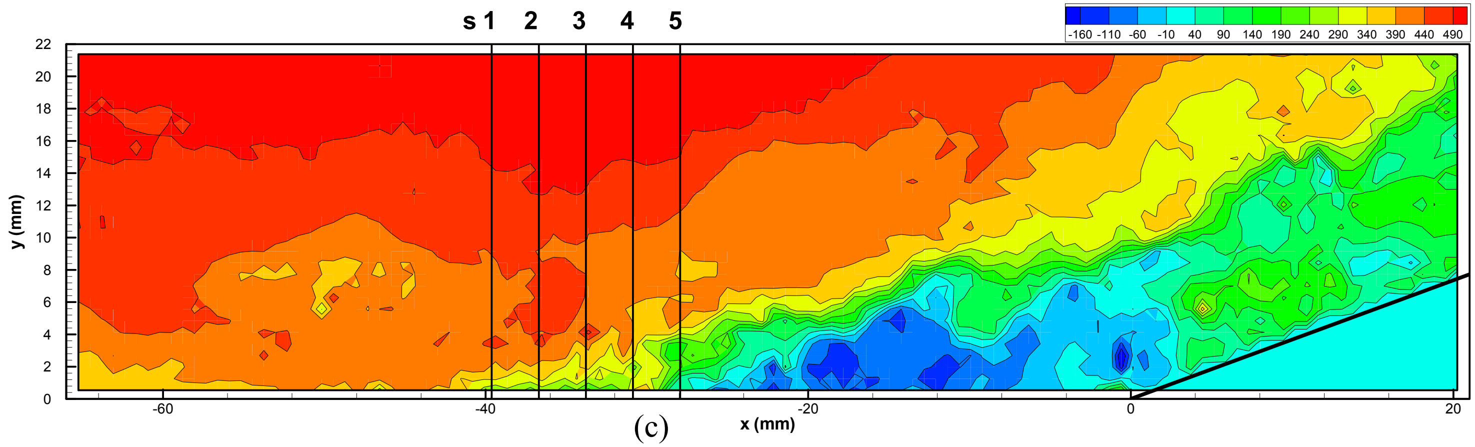

Figure 6.3 Sample instantaneous composite velocity fields for the case where the separation shock-foot is upstream of transducer 1: (a) instantaneous vector field; (b) fluctuating velocity vector field; and (c) contour plot of *u*-velocity (units in m/s). (A hand-drawn line is shown on (a) that indicates the upstream location where the velocity vectors outside the boundary layer first begin to deflect upward.)

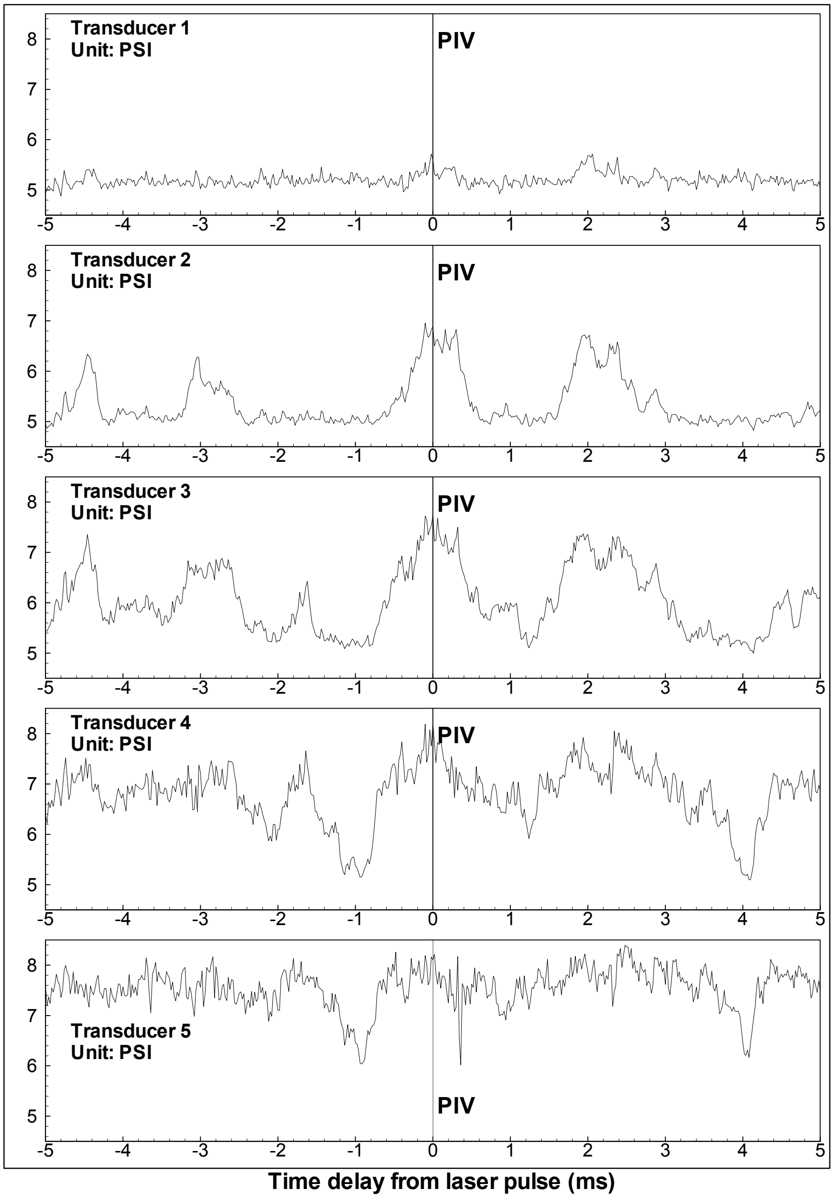

Figure 6.4 Pressure time histories for the five transducers located underneath the intermittent region. Transducer 1 is farthest upstream. The time (in ms) is relative to the first PIV laser pulse. The small pressure maximum at transducer 1 and high pressures on all other transducers show that the shock is at the upstream edge of the intermittent region.

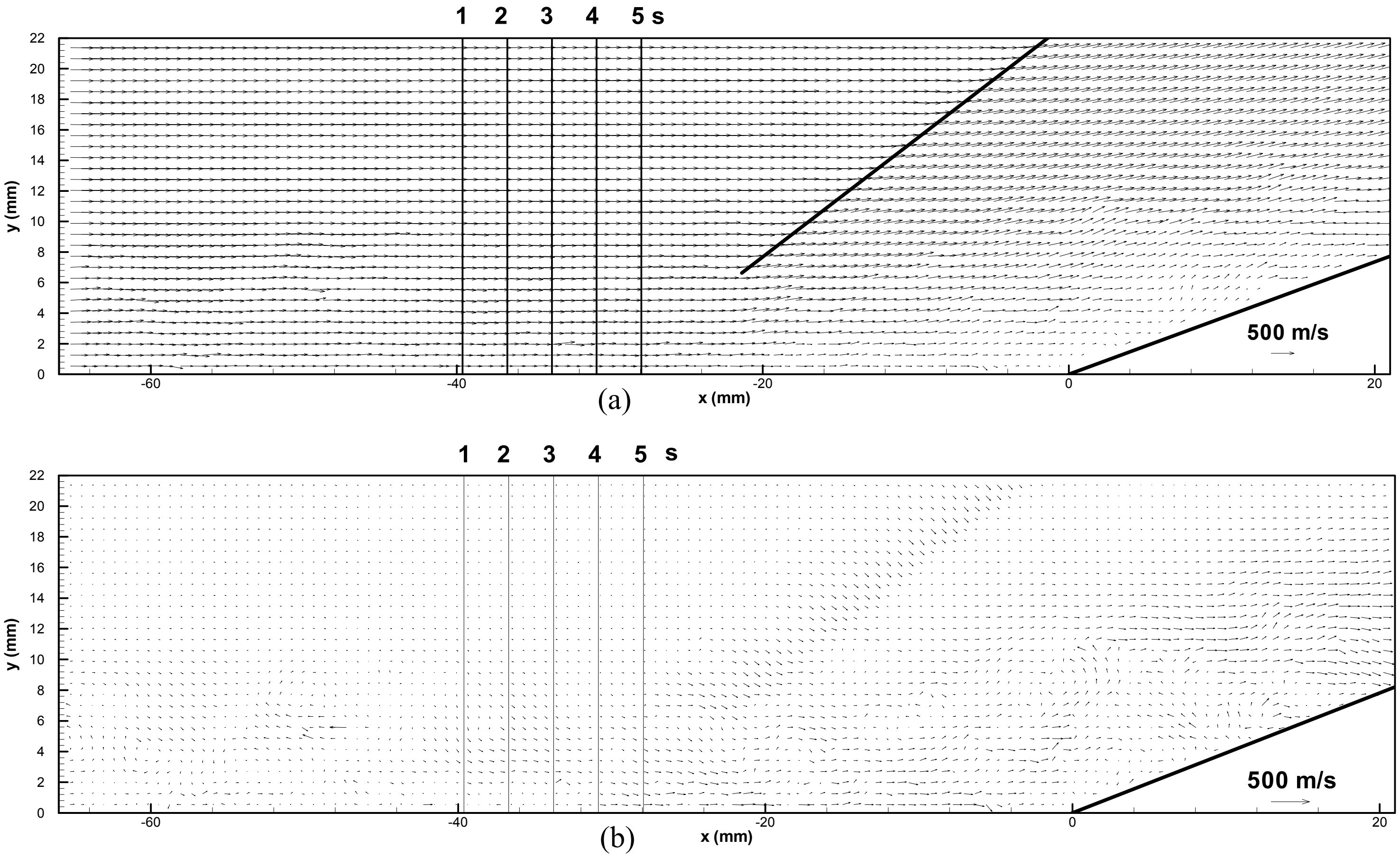

(a)

(b)

Figure 6.5 (See caption next page.)

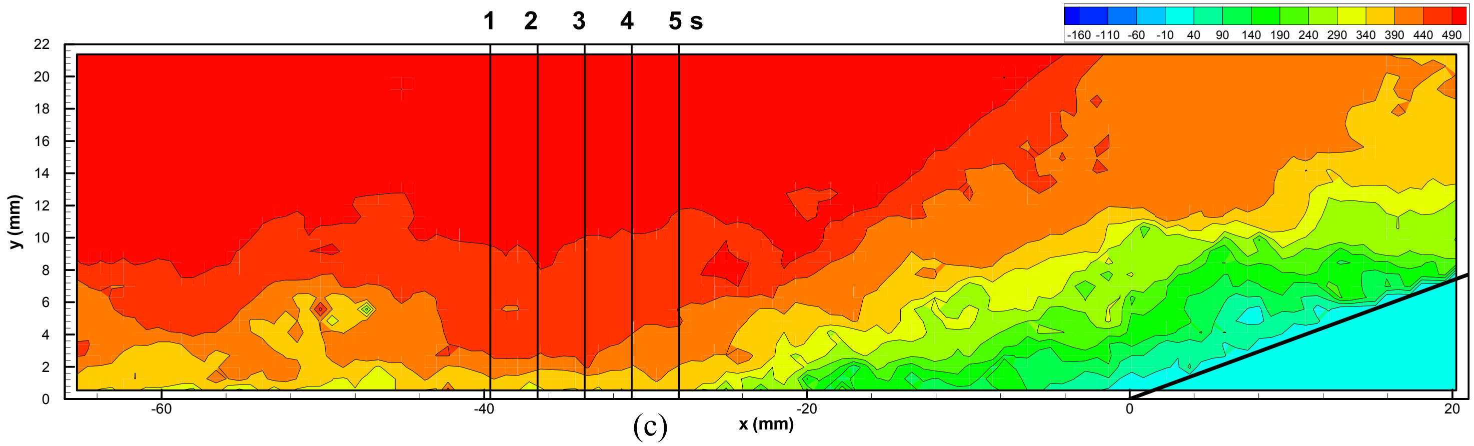

Figure 6.5 Sample instantaneous composite velocity fields for the case where the separation shock-foot is downstream of transducer 5. (a) instantaneous vector field, (b) fluctuating velocity vector field, and (c) contour plot of *u*-velocity (units in m/s). (A hand-drawn line is shown on (a) that indicates the upstream location where the velocity vectors outside the boundary layer first begin to deflect upward.)

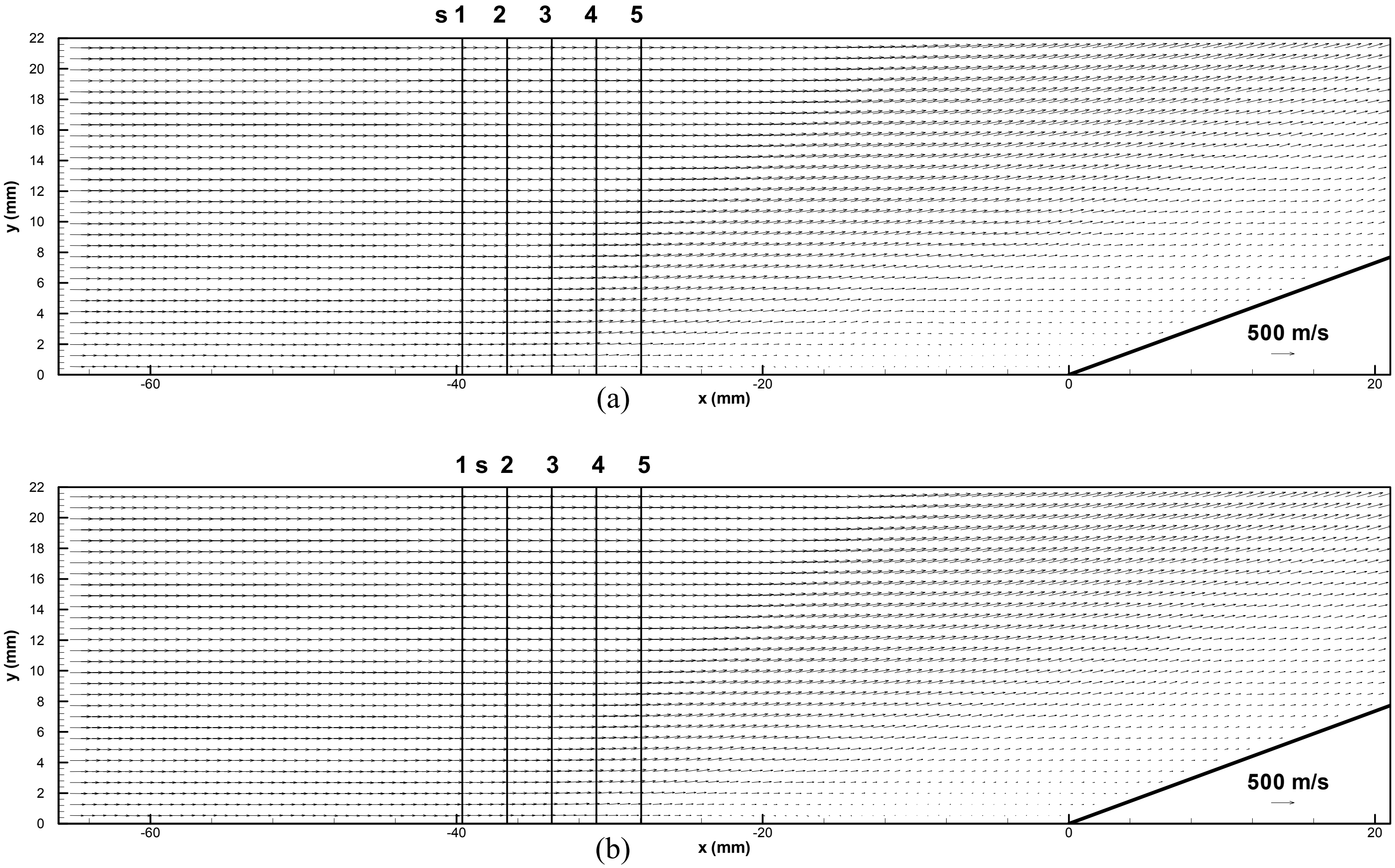

(a)

(b)

Figure 6.6 (See caption next page.)

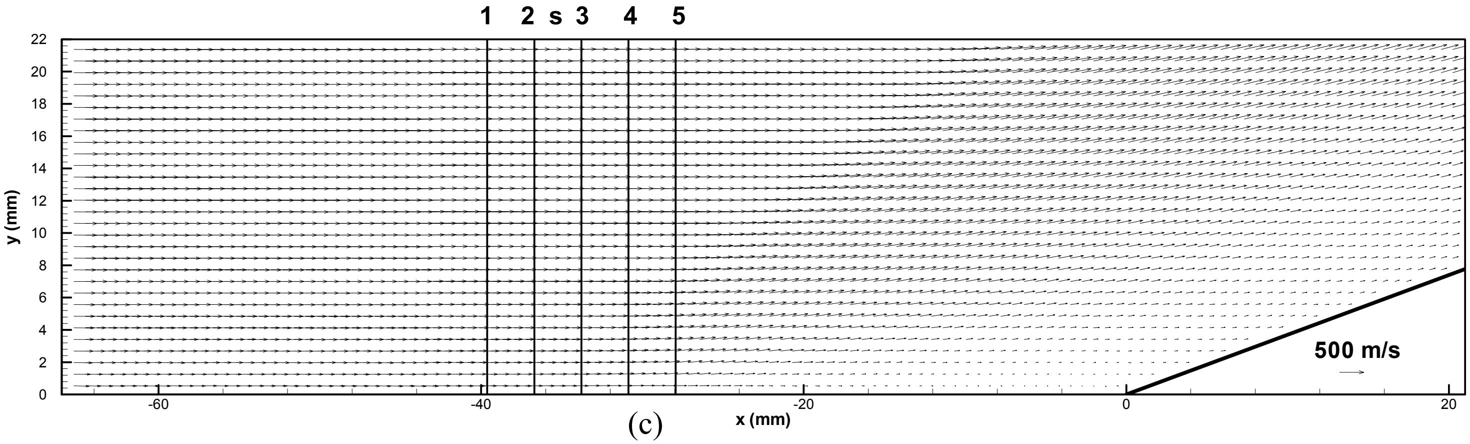

(c)

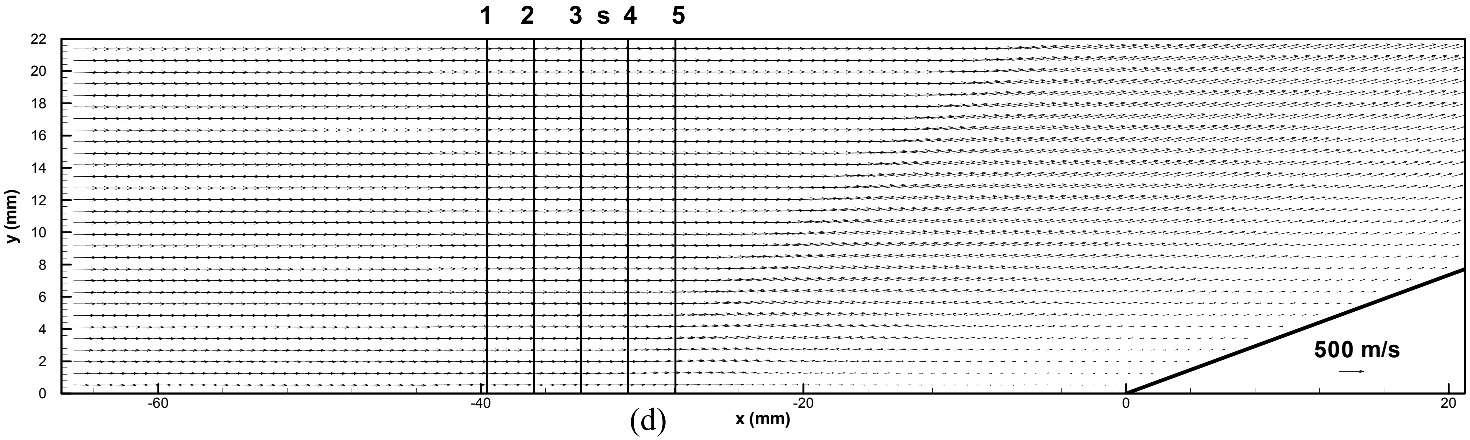

(d)

Figure 6.6 (See caption next page.)

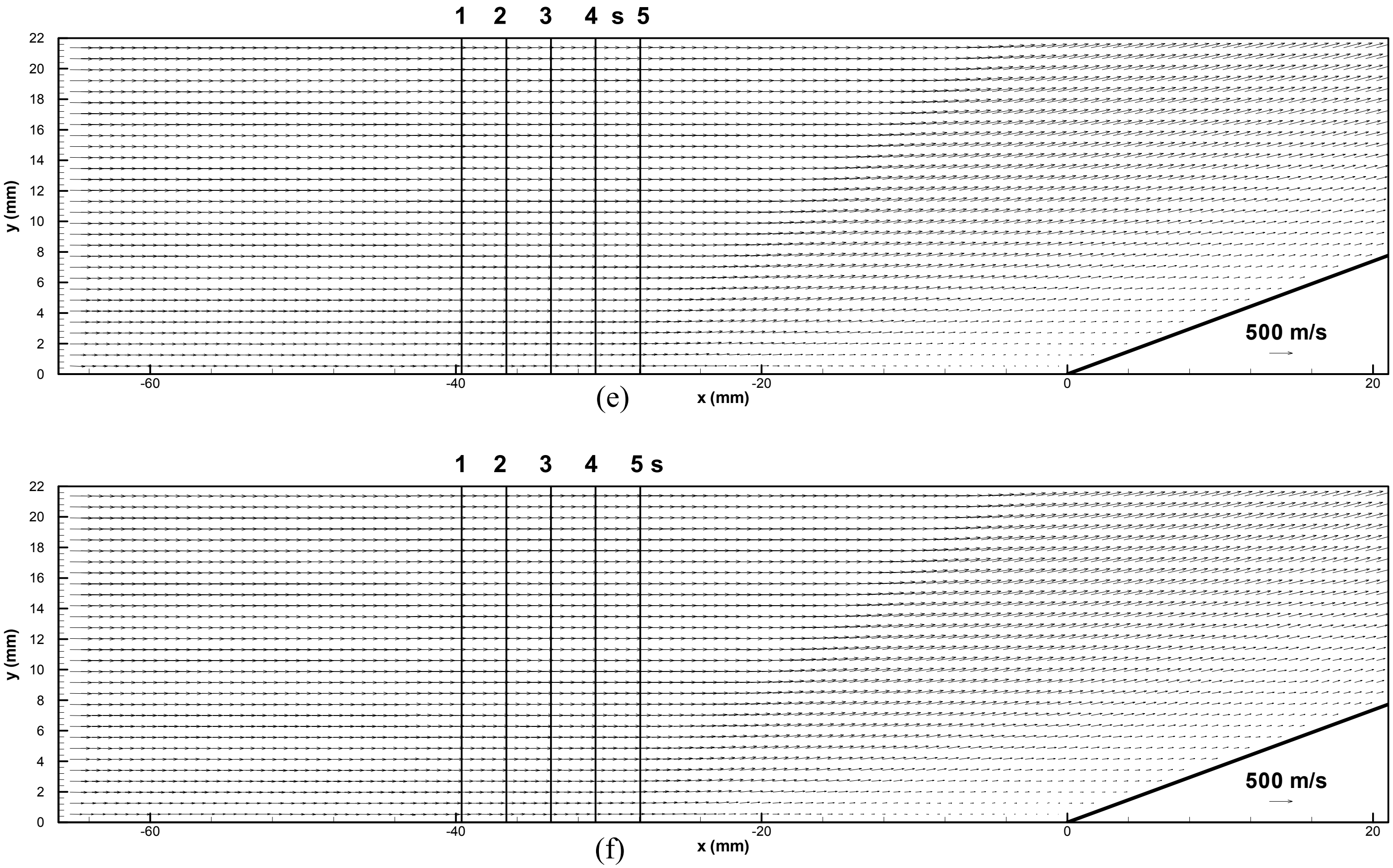

Figure 6.6 Conditional-average velocity vector plots for six shock-foot locations (units in m/s)

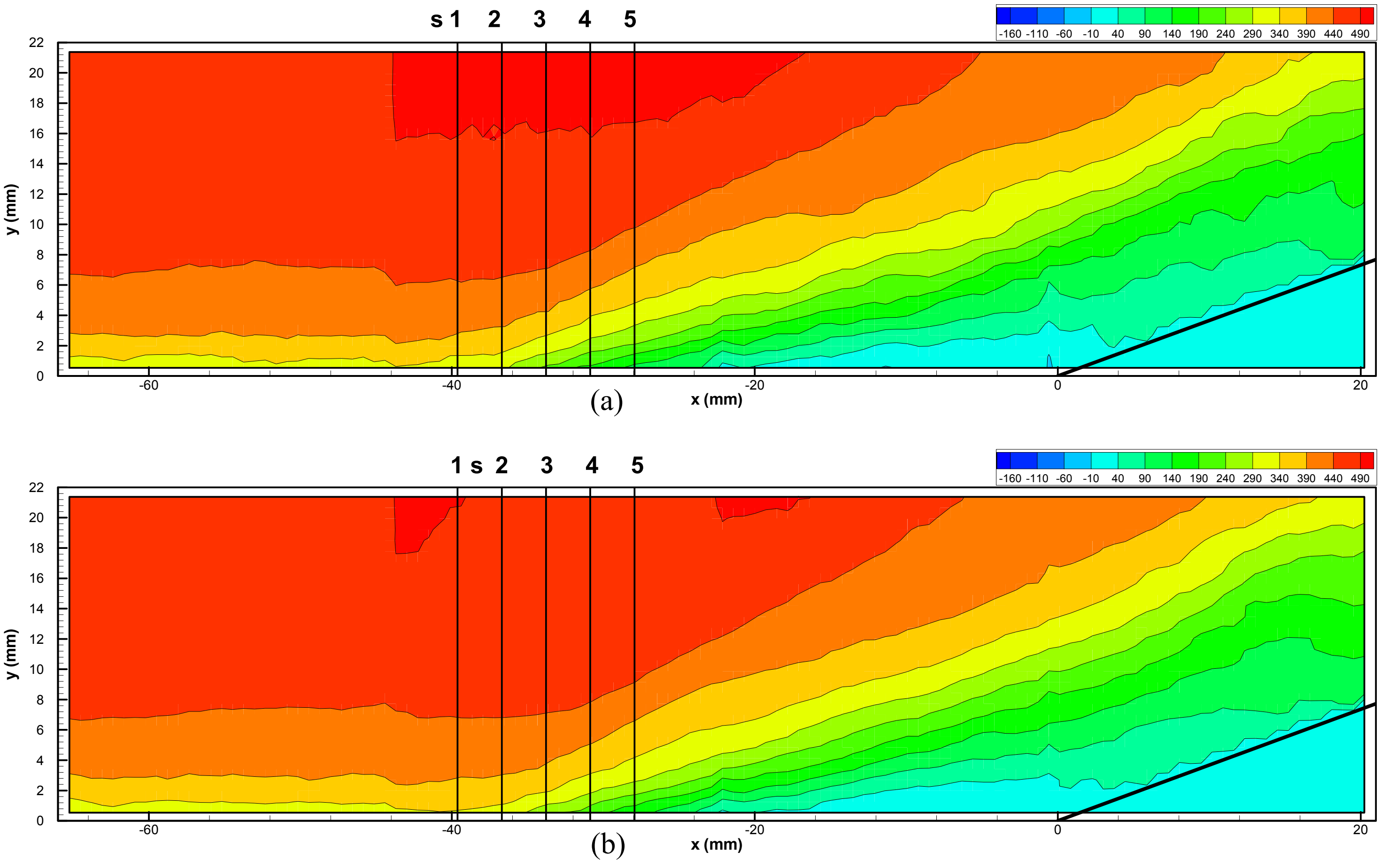

(a)

(b)

Figure 6.7 (See caption next page.)

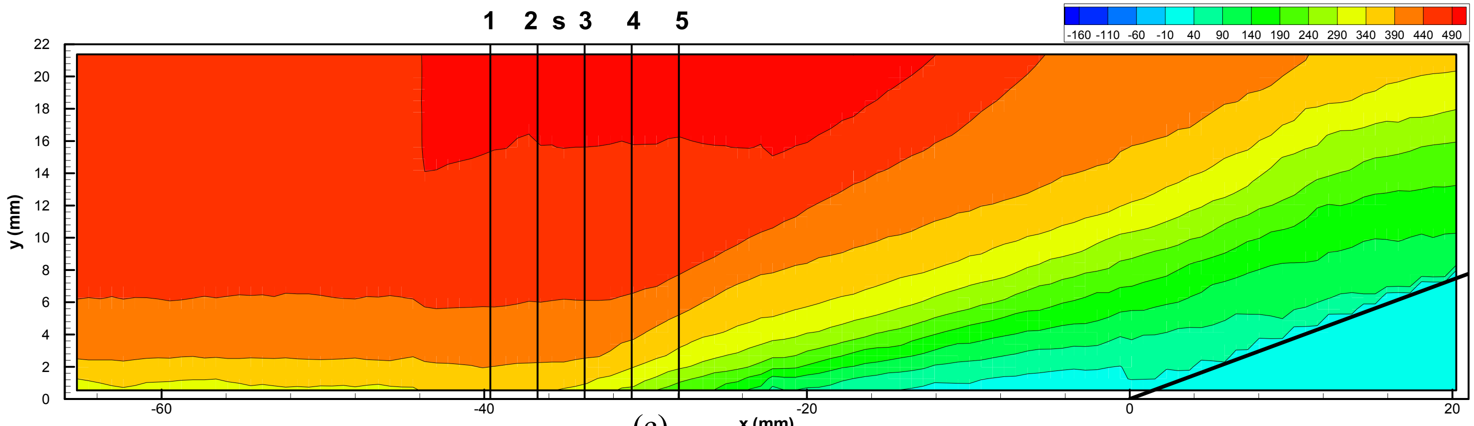

(c)

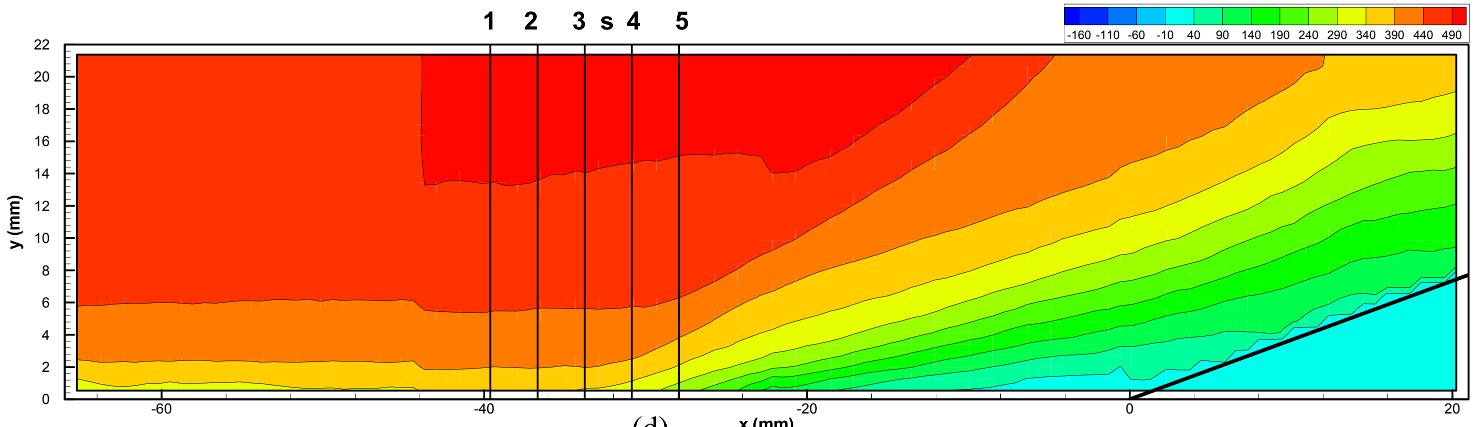

(d)

Figure 6.7 (See caption next page.)

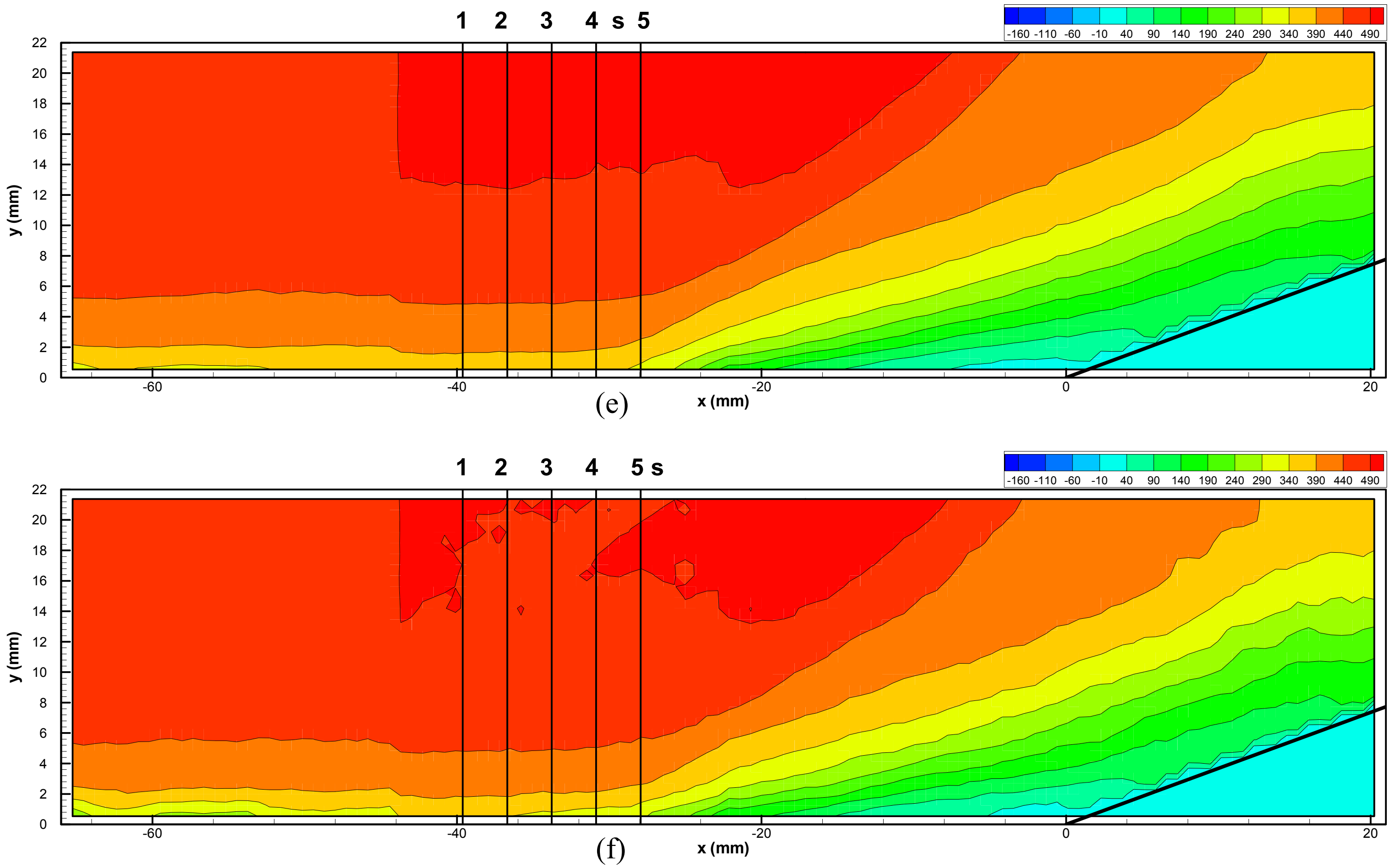

(e)

(f)

Figure 6.7 Conditional-average *u*-velocity contour plots for six shock-foot locations (units in m/s).

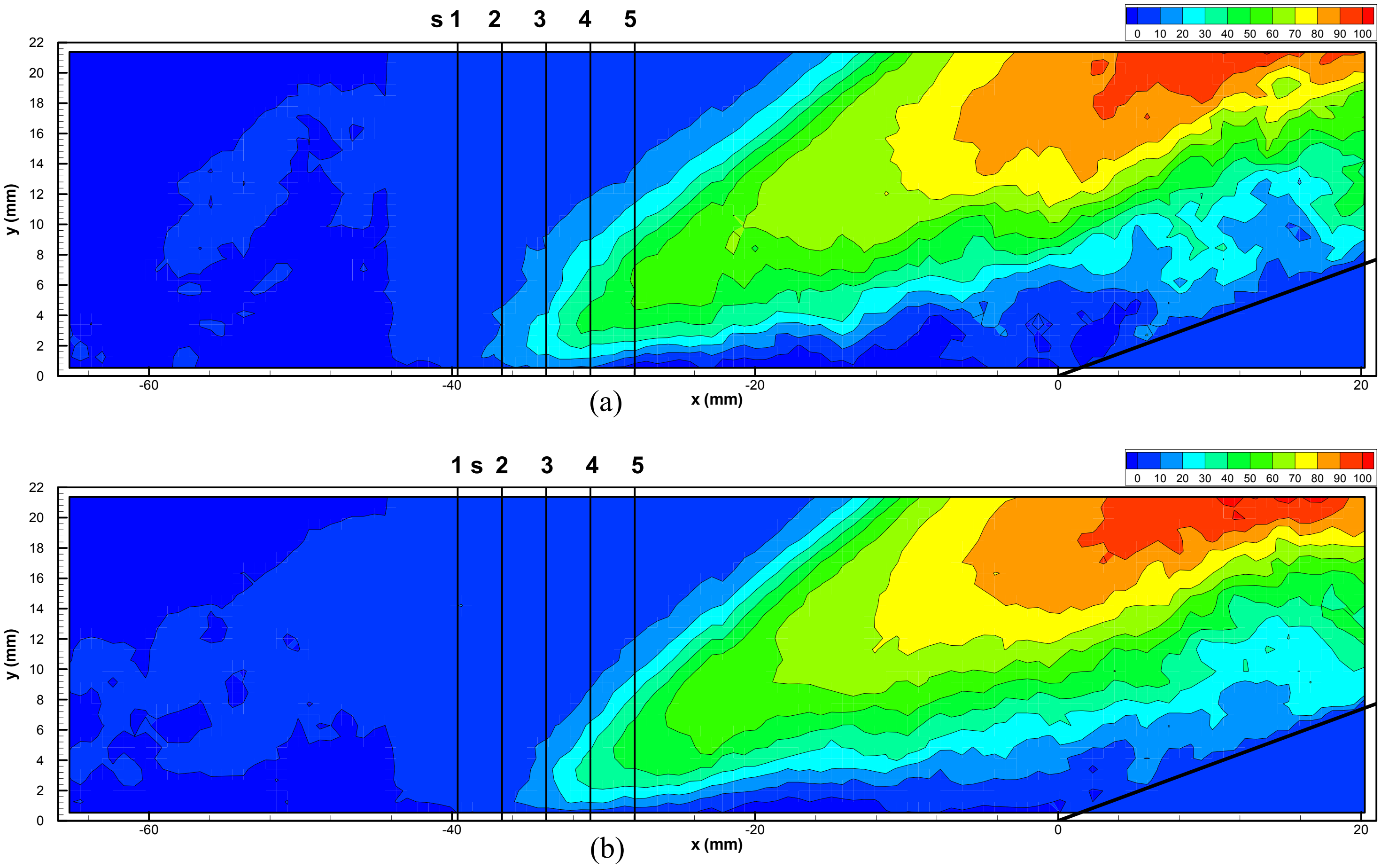

Figure 6.8 (See caption next page.)

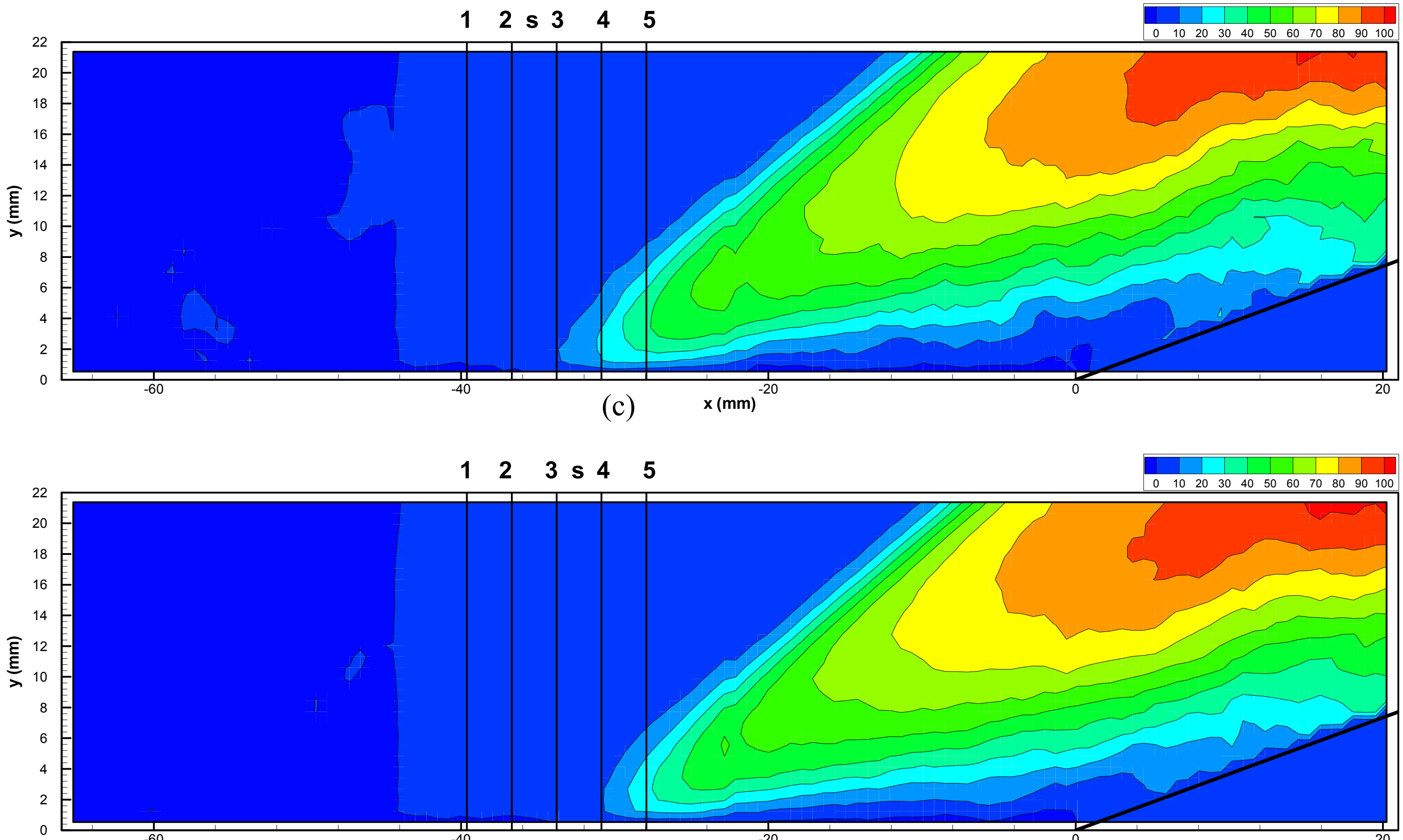

(c)

(d)

Figure 6.8 (See caption next page.)

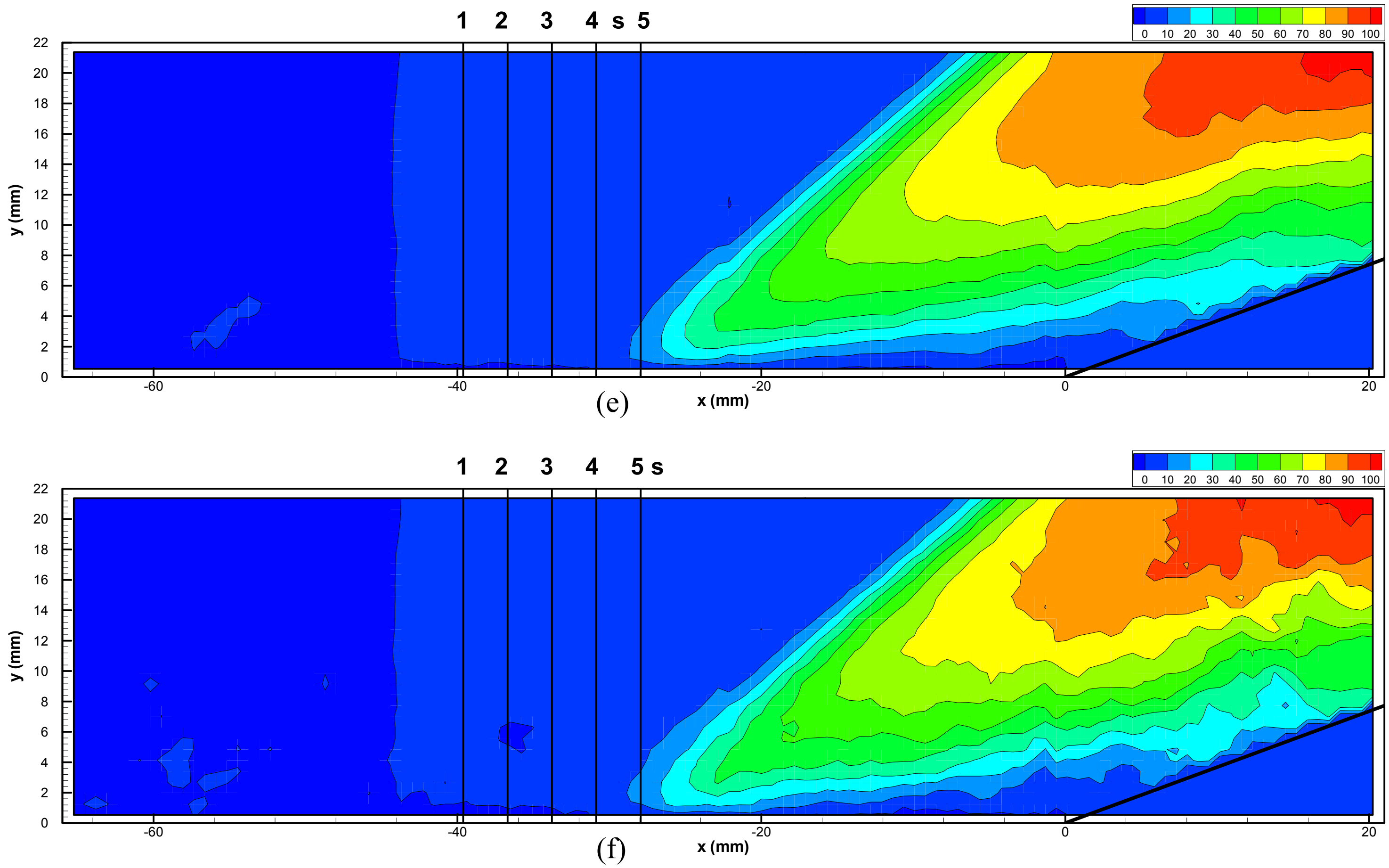

Figure 6.8 Conditional-average *v*-velocity contour plots for six shock-foot locations (units in m/s)

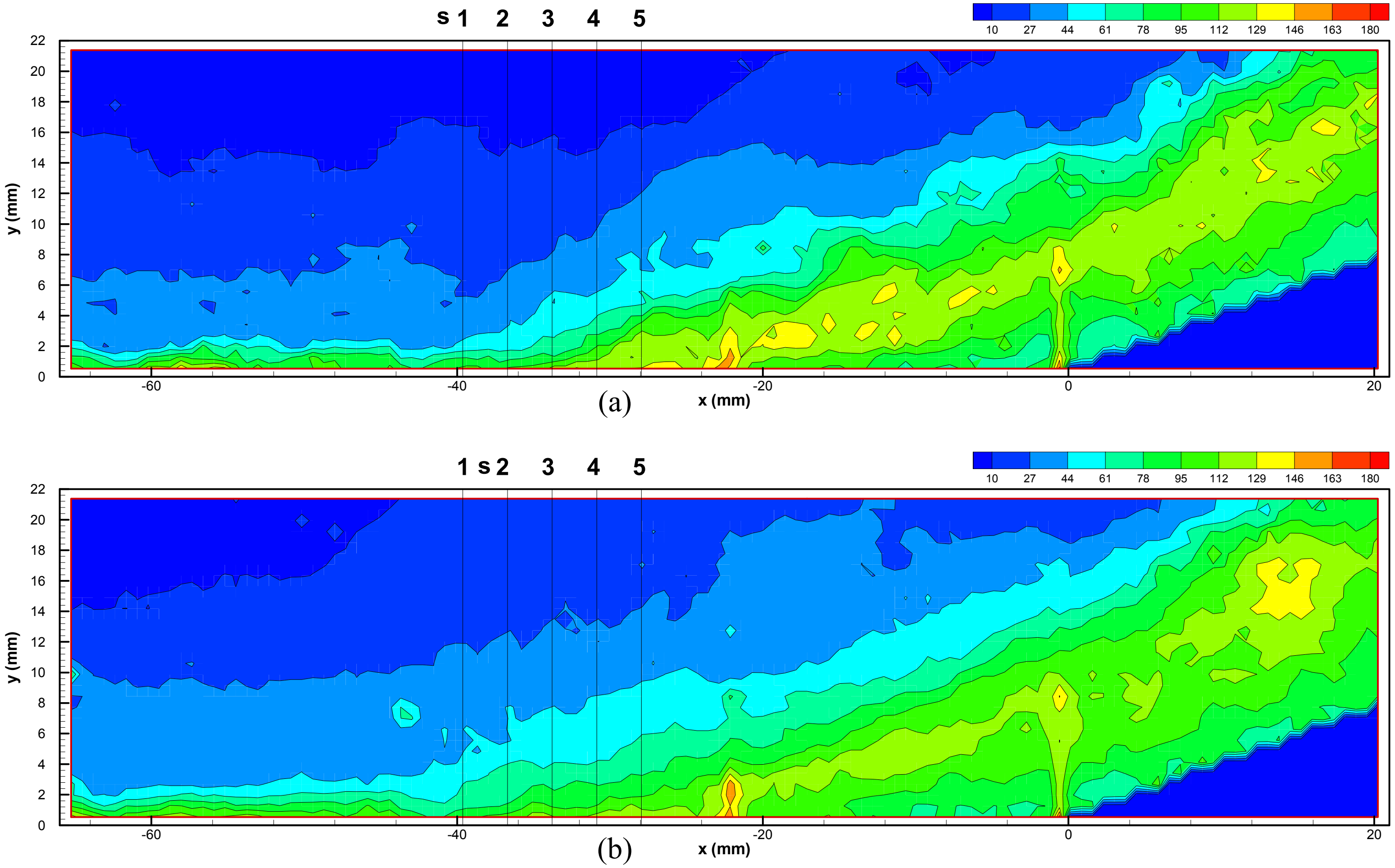

Figure 6.9 (See caption next page.)

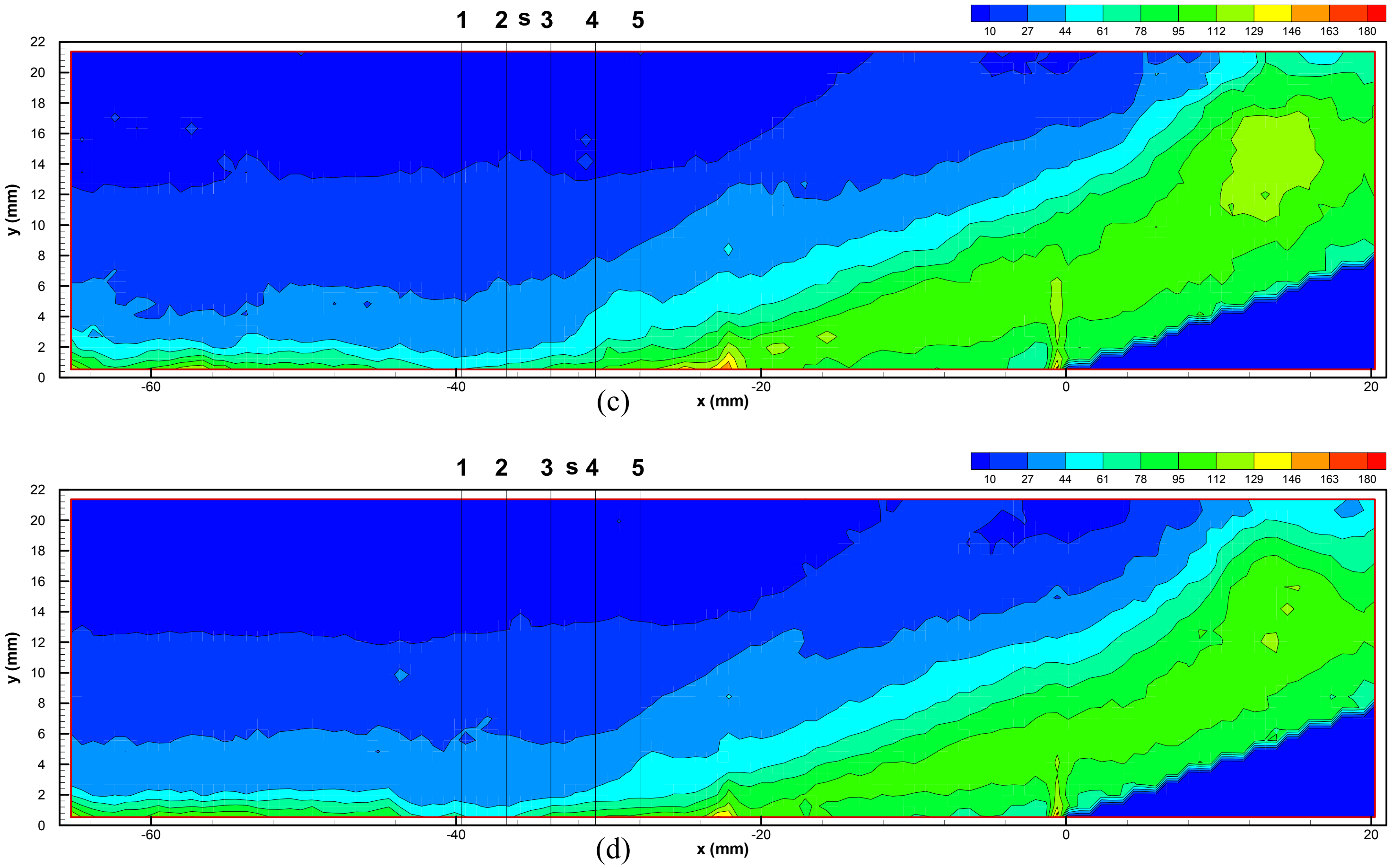

Figure 6.9 (See caption next page.)

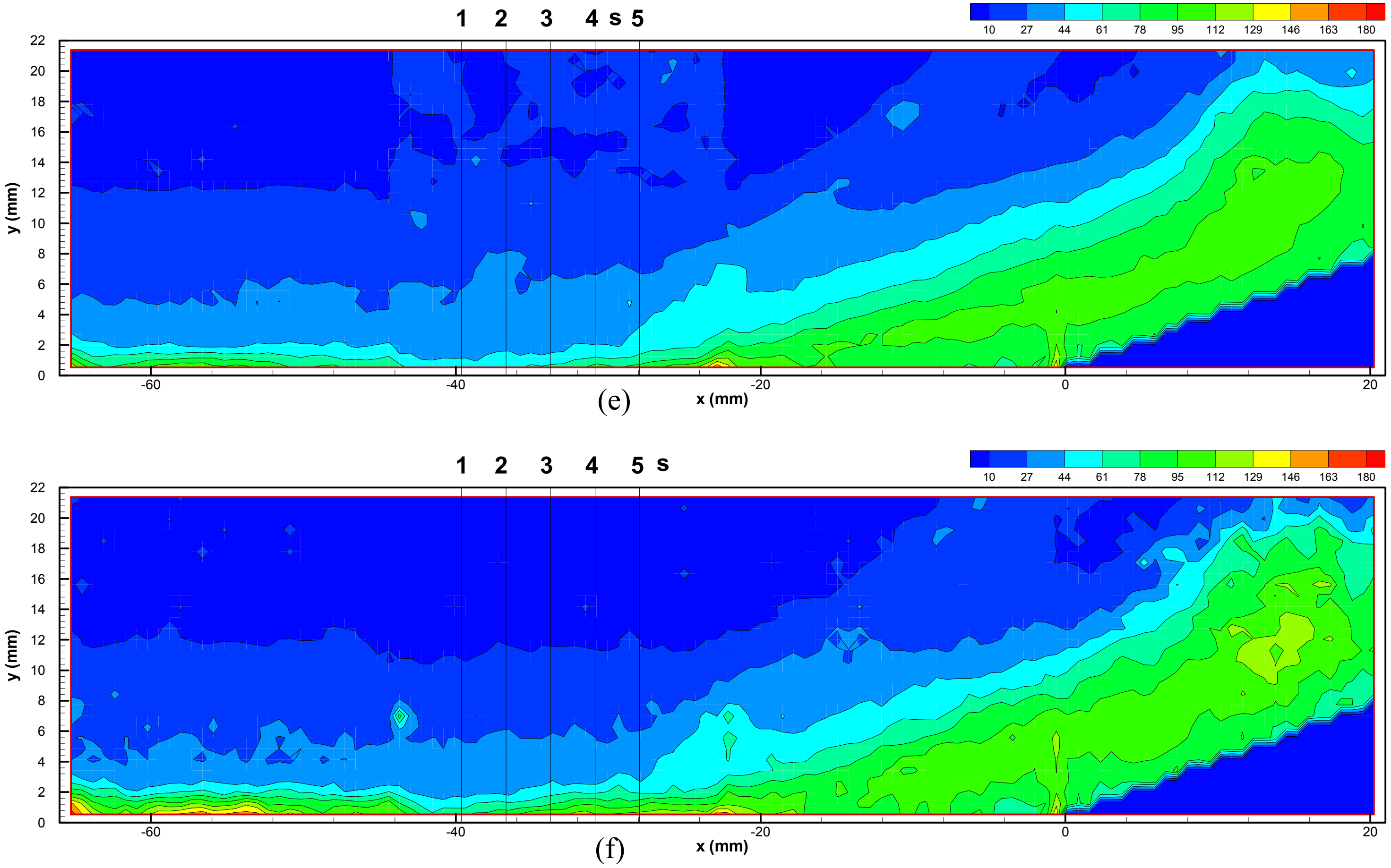

Figure 6.9 Conditional u_{rms} contour plots for six shock-foot locations (units in m/s).

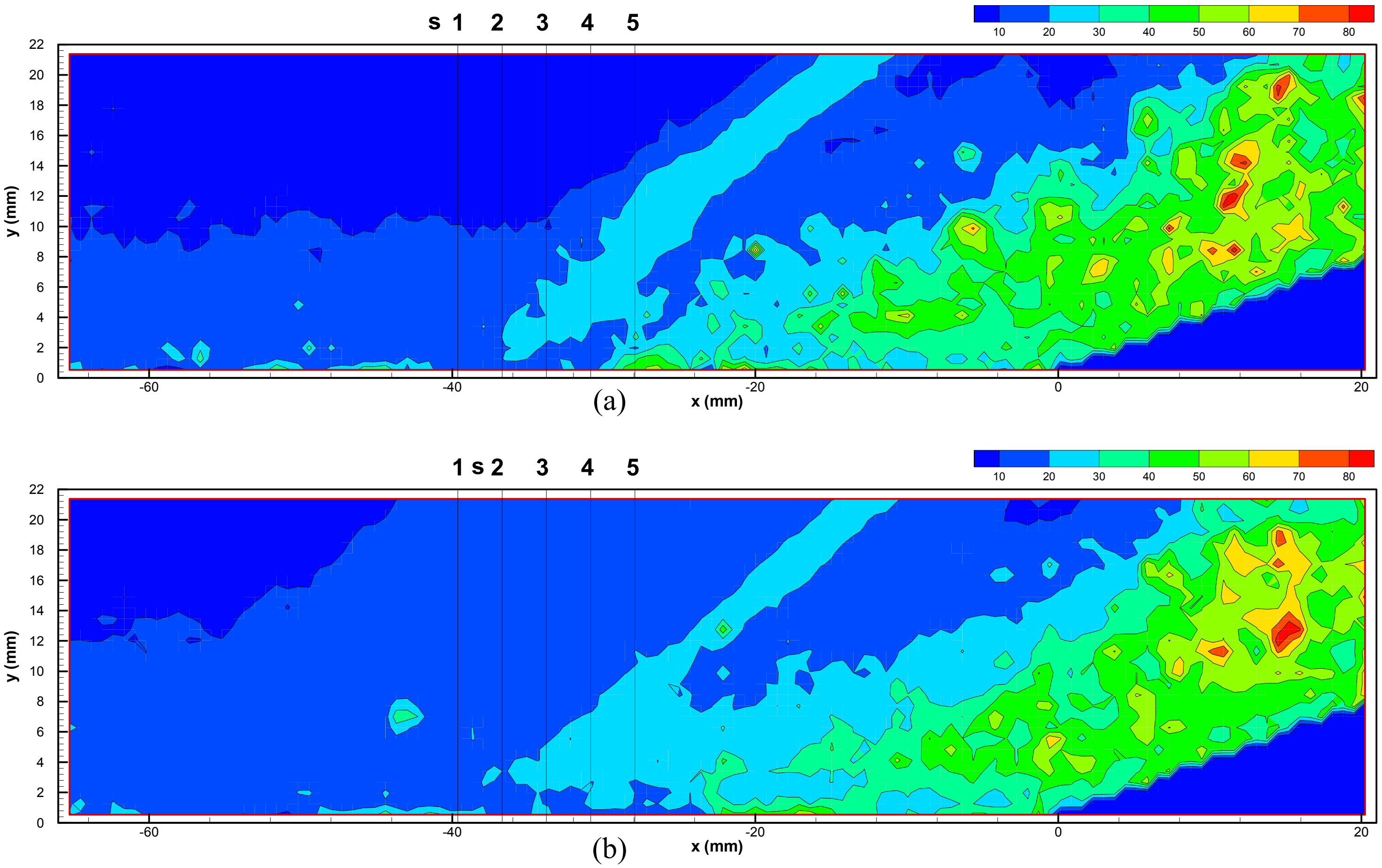

Figure 6.10 (See caption next page.)

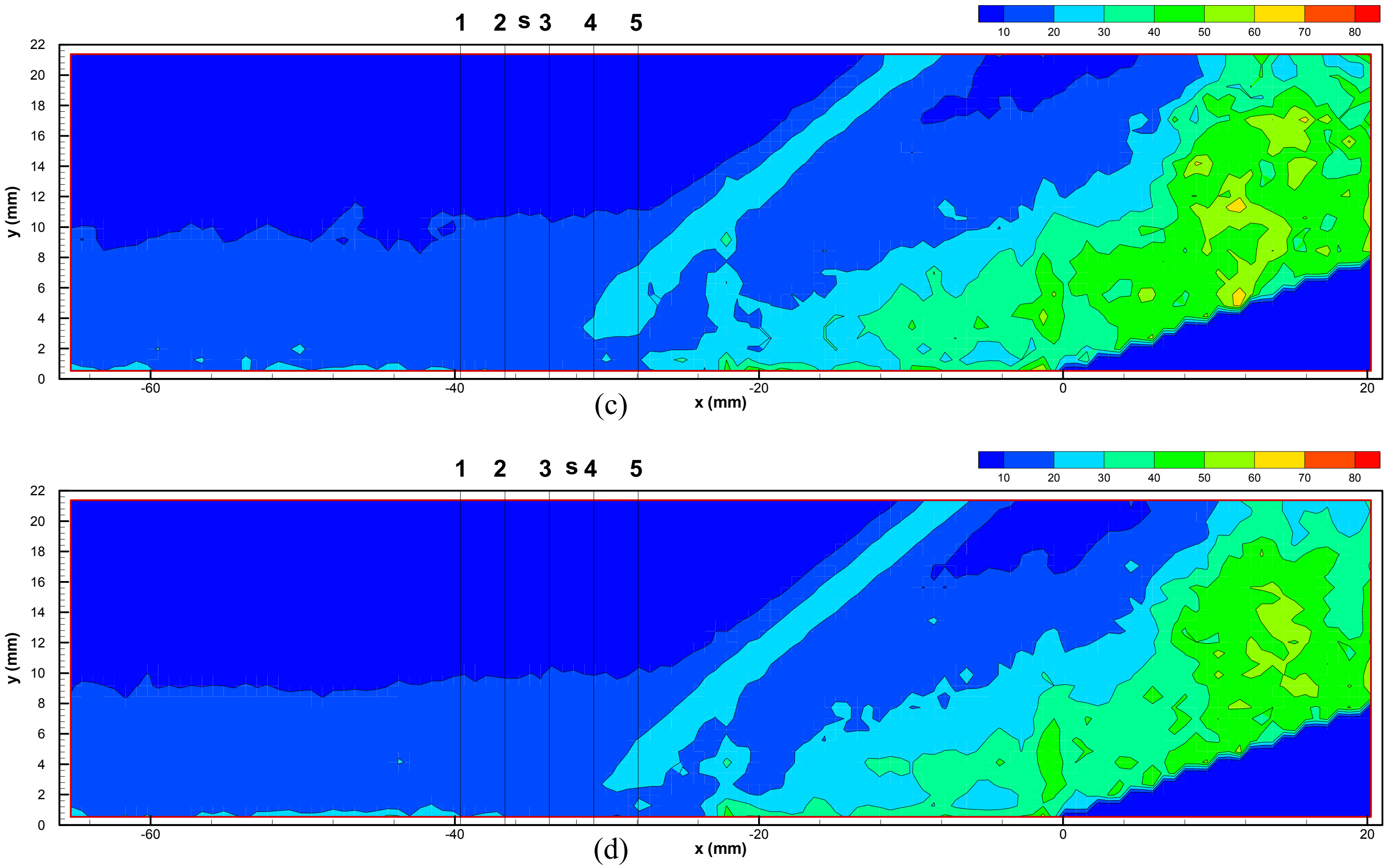

(c)

(d)

Figure 6.10 (See caption next page.)

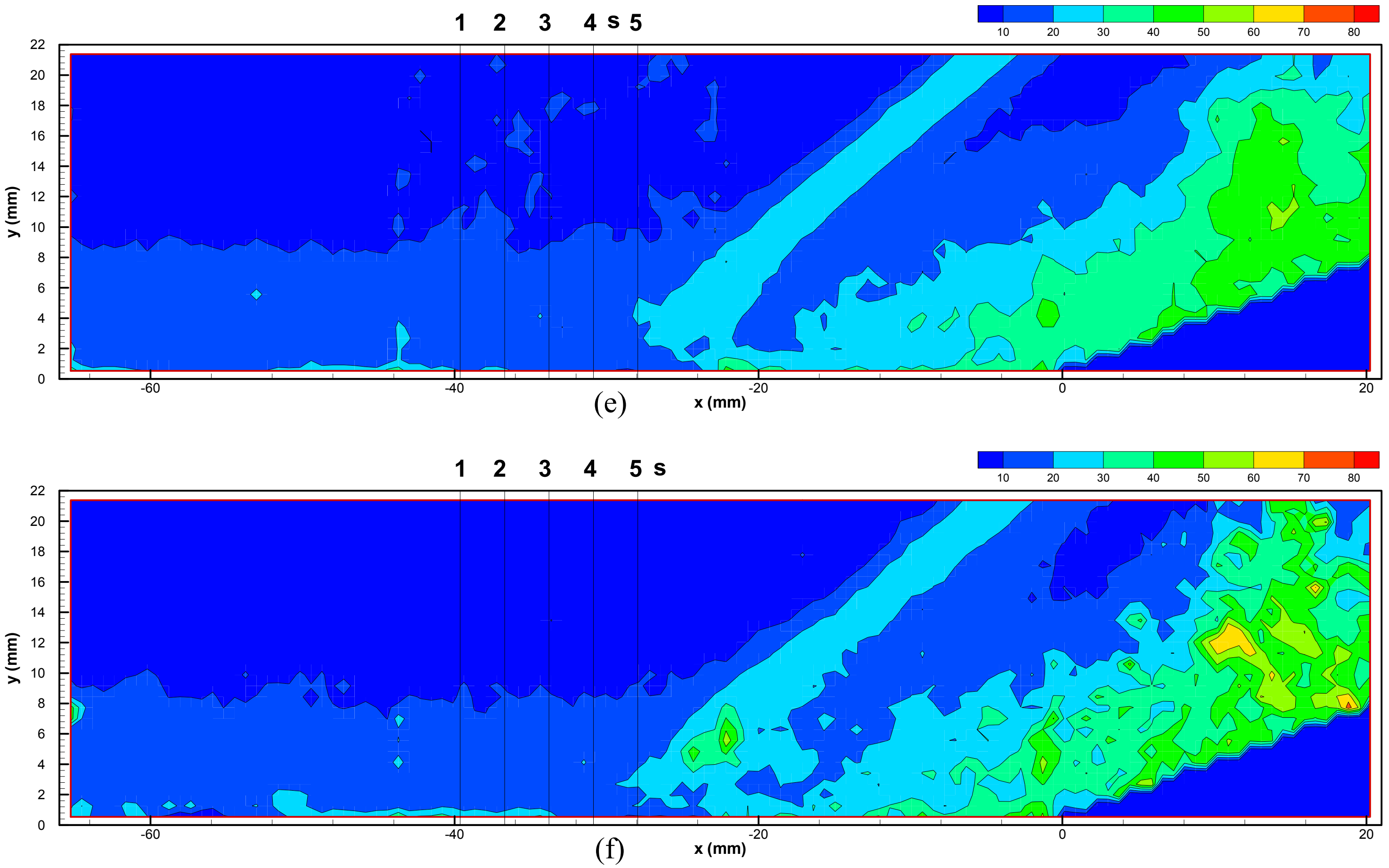

Figure 6.10 Conditional u_{rms} contour plots (units in m/s).

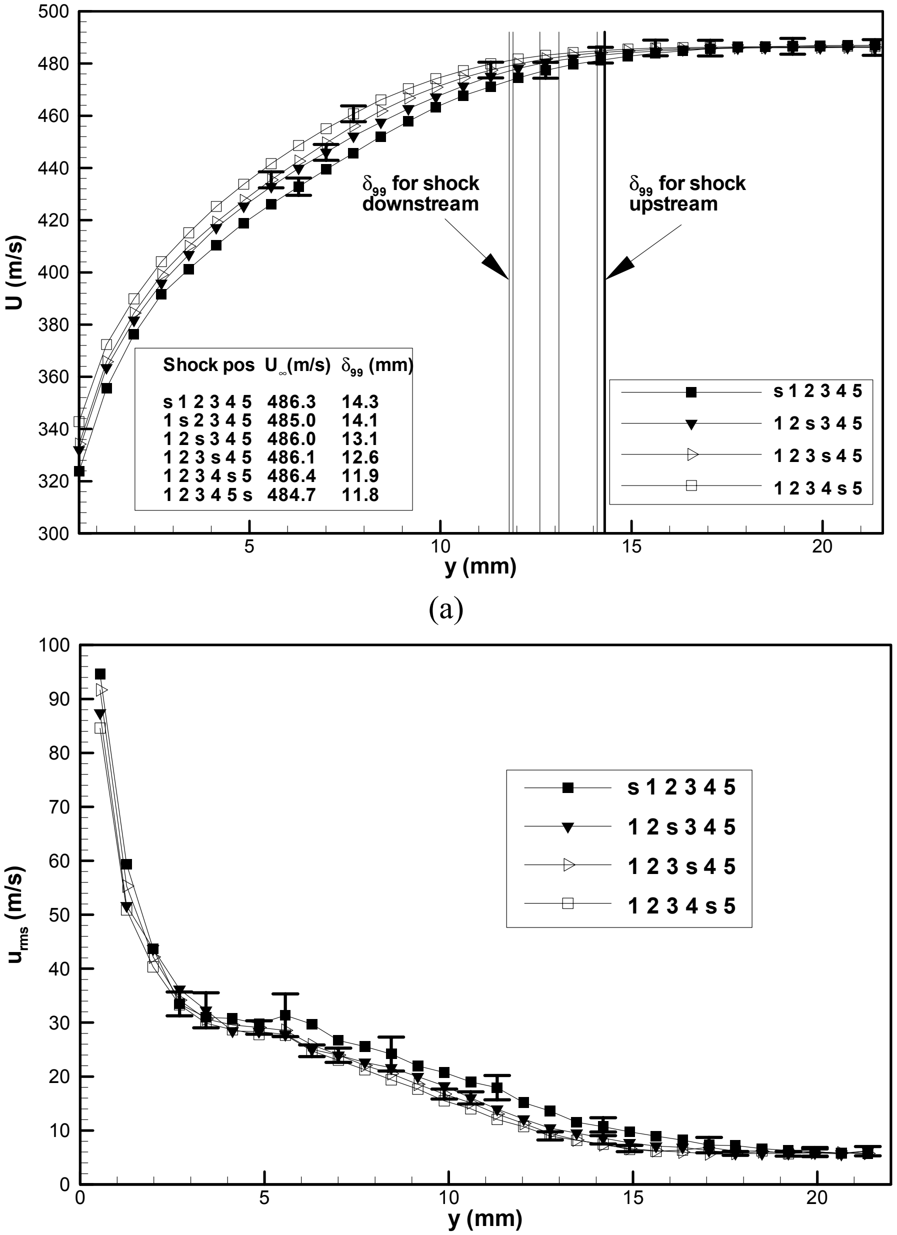

(a)

(b)

Figure 6.11 Upstream (i.e., upstream of x=-45 mm) boundary layer profiles for different shock-foot locations: (a) streamwise velocity profile, and (b) u_{rms} profiles.

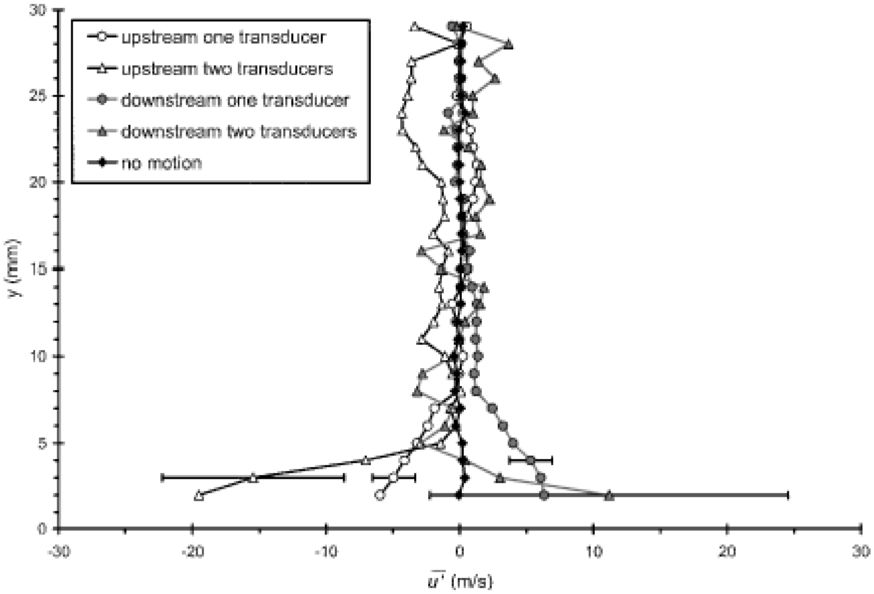

(a)

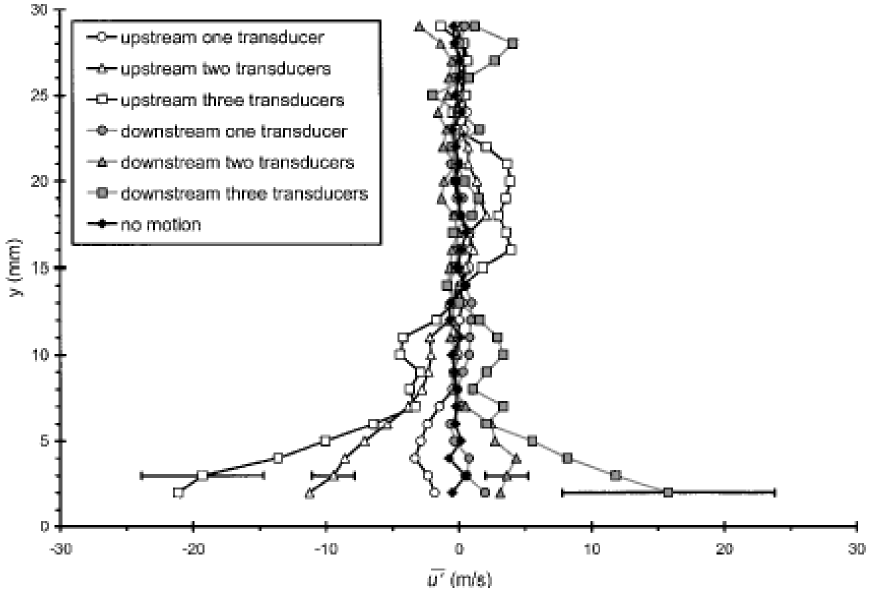

(b)

Figure 6.12 Conditional ensemble average profiles of the streamwise velocity fluctuations in the incoming boundary layer conditioned on the separation shock foot motion within a time period of: (a) 100 and (b) 250 µs. (28^o ramp in Mach 5 flow; Beresh et al. 1999 and 2002).

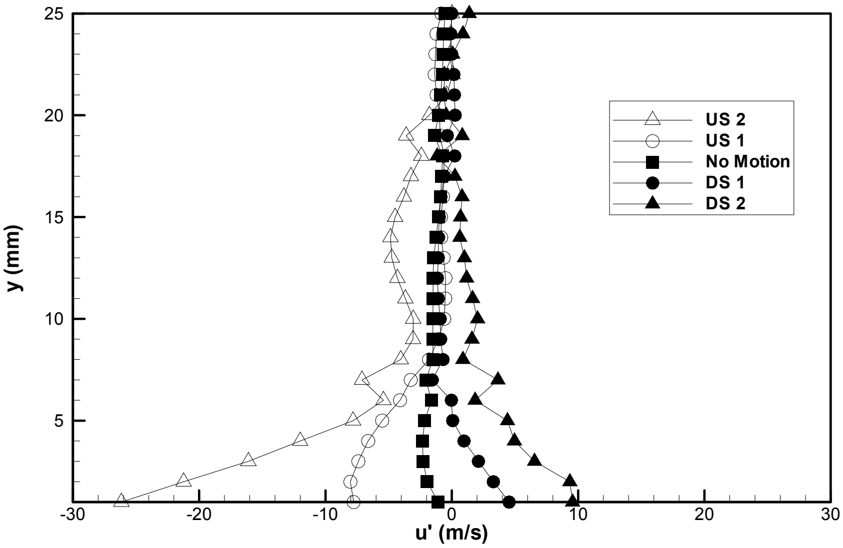

(a)

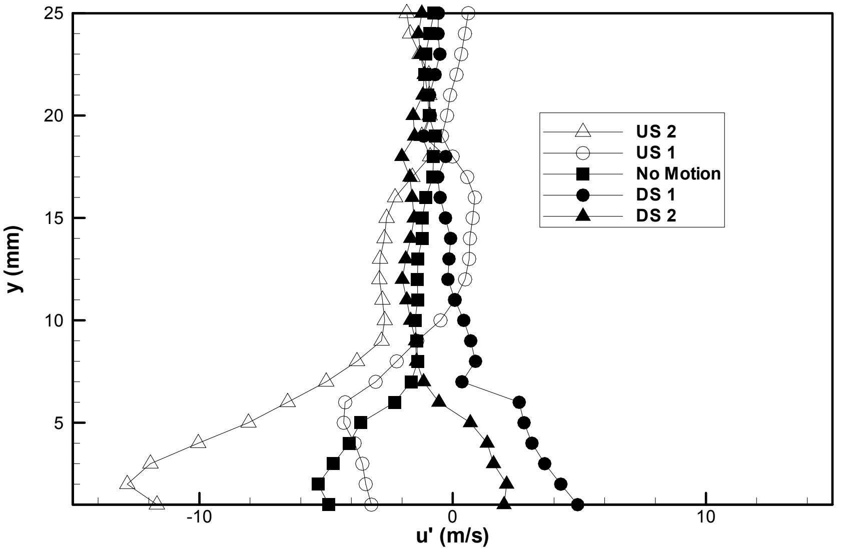

(b)

Figure 6.13 Conditional ensemble average profiles of the streamwise velocity fluctuations in the incoming boundary layer conditioned on the separation shock foot motion within a time period of: (a) 100 and (b) 250 μs. (Blunt fin in Mach 5 flow; Ünalmis et al. 2000).

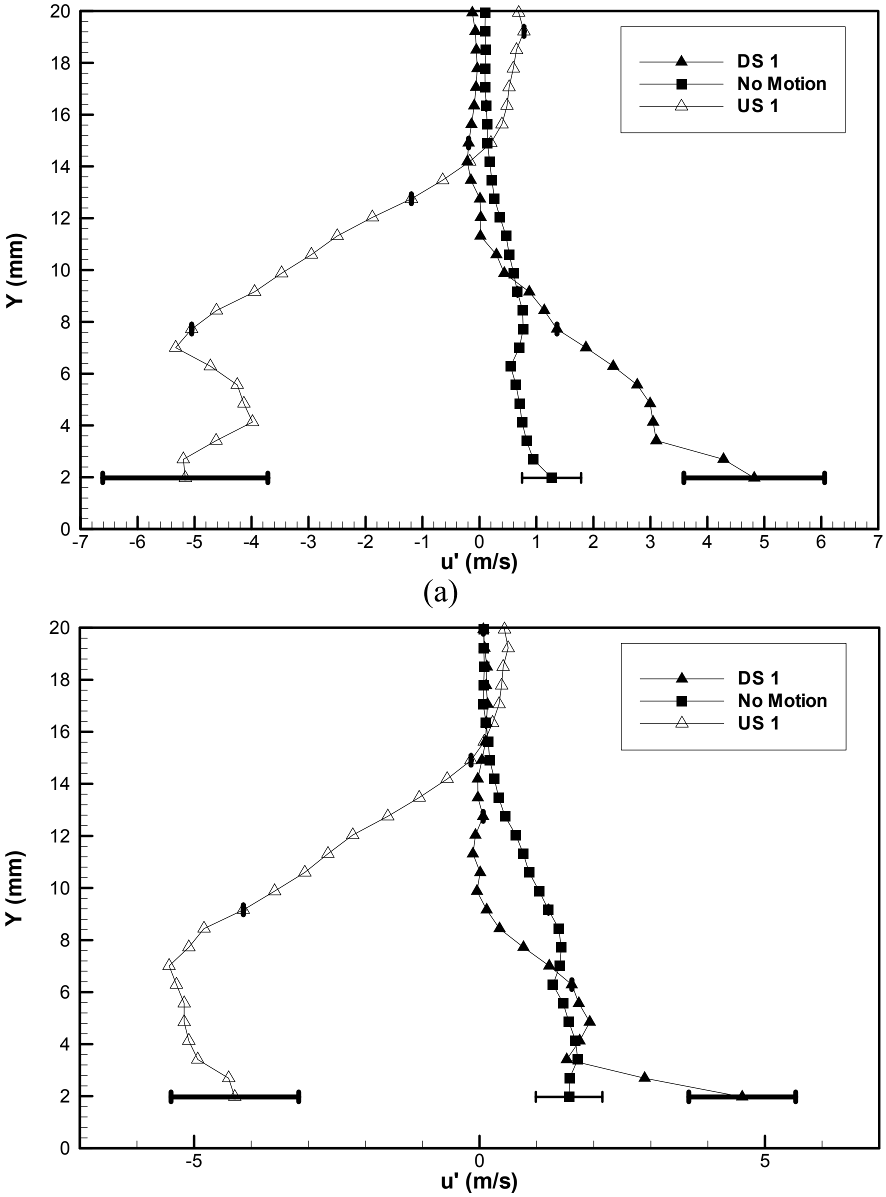

(a)

(b)

Figure 6.14 (See caption next page.)

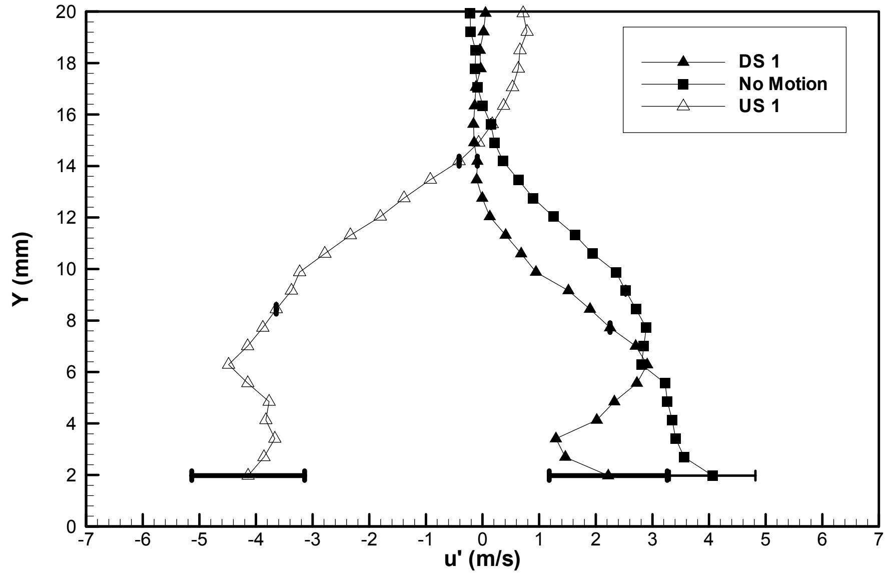

(c)

Figure 6.14 Conditional ensemble average profiles of the streamwise velocity fluctuations in the incoming boundary layer conditioned on the separation shock foot motion within a time period of: (a) 120; (b) 200; and (c) 520 μs. (20^o ramp in Mach 2 flow; current study).

Chapter 7

Time-Sequenced PIV Measurement of SWTBLI

7.1 INTRODUCTORY REMARKS

The wide-field PIV discussed in chapter 6 provides a powerful tool for investigating shock-induced separated flows; however, because the sampling rate is only 10 Hz, the data are essentially randomly sampled and can provide no time-correlated information. In many cases, however, time-correlated information is desired to investigate dynamic phenomena, such as the evolution of turbulent structures as they pass through the interaction. As discussed in chapter 4, the multi-camera, multi-laser PIV system is capable of capturing up to four time-sequenced PIV vector fields with a time between images as small as 30 μs. In this chapter, two experiments are discussed where two-vector fields are acquired with an inter-frame time of 40 μs. In these two independent applications, measurements were made in: (*i*) the intermittent region to investigate shock dynamics, and (*ii*) the upstream boundary layer to investigate the boundary layer acceleration mechanism proposed by Beresh et al. (2002).

The work discussed in this section is only preliminary and at best can be considered as a set of “proof-of-concept” experiments. The time-sequenced PIV work is preliminary because time and funding constraints precluded a more thorough development and application of the techniques.

7.2 TIME-SEQUENCED PIV OF INTERMITTENT REGION

The objective of this set of experiments was to demonstrate the application of time-sequenced PIV for the purpose of investigating separation shock dynamics, such as the response of the shock to turbulent structures convecting through the flow. Details of the procedure were discussed previously in chapter 4. The two cameras viewed the same region in the flow by having both view the flow through a beam splitting cube. The cameras were registered "by eye" by adjusting their translation and tilt until the fields of view were matched to an accuracy of about a pixel. This level of accuracy was sufficient for the purposes of this demonstration experiment.

As a test of the ability to capture the time-sequences with the same field of view, the timing of the lasers and cameras was adjusted to produce zero time delay so that, in theory, the cameras would acquire identical images. Displacement, translation, or relative distortion between the two cameras could result in the images being imperfect matches at zero time delay. Figure 7.1 shows sample instantaneous vector fields for these validation experiments. The field of view is such that both the separation shock and some of the separated flow region can be captured. It can be seen that the vector fields are very similar, with the primary differences being due to bad (outlying) vectors. The mean vector fields (not shown) are virtually identical. These results indicate that any differences seen in the time sequences will likely be due to actual fluid mechanical phenomena, not diagnostic problems.

Sample time-sequenced velocity vector fields obtained with a time delay of 40 μs are shown in Fig. 7.2. The field of view is the same as in the validation experiments, and therefore it captures part of the separation shock and part of the region of separated flow, but typically not the separation shock foot. In 40 μs, fluid traveling at the freestream velocity of 500 m/s will travel a distance of 20 mm, i.e. nearly across the entire image, which is 21.6 mm wide. Fluid that is traveling slower than this, such as that in the boundary layer or separated flow, should not convect as far. From the sample images of Fig. 7.2 some interesting observations can be made. For example, near the vertical middle of the image it is seen that the velocity vector angle after the shock in Fig. 7.2(a) is substantially different in each image of the pair. Furthermore, although the shock foot cannot be seen in these images, the separation shock does seem to be reasonably distorted in 40 μs. Some degree of shock distortion, likely by convecting turbulent structures, can be seen in all three of the image pairs and is qualitatively consistent with what have been observed by using PLS imaging (Beresh et al. 1998). In Beresh et al. (1998), the PLS visualizations in Mach 5 compression ramp interactions showed that although the outer part of the shock would be greatly distorted by upstream turbulent structures, the shock foot did not move appreciably in 15-30 μs. Since the shock foot cannot be identified in the PIV images, owing to interference from the boundary layer turbulence, it is not known if this is the case in the present study. Future experiments that seek to explore the shock dynamics in more detail would greatly benefit from making simultaneous wall pressure measurements to identify the instantaneous shock-foot position.

In the first frame Fig. 7.2(b), it appears that the separation shock foot is located just upstream of the leftmost edge of the image. Downstream of this location, the flow exhibits varying deflection angles, but it does not appear to be separated anywhere in the image. In the second frame, it is not clear where the shock foot is, but the flow is clearly separated starting at about x=30 mm. From these limited data it is not known why the flow separates at that instant. It is possible that the region of separated flow simply convected into the field of view, or the shock strengthened during this time, or perhaps a turbulent structure with a large negative velocity fluctuation convected through the shock. At this time it is only possible to conjecture about the possible mechanisms, but such effects clearly warrant additional study, perhaps with simultaneous pressure measurements to locate the shock foot. In addition, in future studies four-image time-sequences could be used to provide even more information about the time-varying flow field.

7.3 CORRELATION WITH UPSTREAM ACCELERATION AND SHOCK FOOT MOTION

As discussed in Chapter 1, Beresh et al. (2002) showed that there is a correlation between upstream boundary layer velocity fluctuations and shock foot motion. They also suggested that the likely mechanism that drives the shock motion is that rate of change of the velocity profile, rather than simply fluctuations in the profile. This led them to suggest that perhaps measurements of local acceleration (i.e., *du/dt*) would exhibit a stronger correlation with shock motion than u' does.

Therefore, a preliminary study was conducted to see if acceleration in the upstream boundary layer is correlated with shock-foot motion. The acceleration measurements were made by using two PIV cameras, which imaged the same field of view, but which captured particle image pairs separated in time by 40 μs. Such a measurement requires careful registration of the two cameras, and this procedure and its validation were discussed in chapter 4.

The experiments were conducted by capturing time-sequenced PIV images in the upstream boundary layer simultaneously with data from six fast-response pressure transducers located under the intermittent region. The total number of valid segments (acceleration fields) obtained in this set of experiment was 2770. The numbers of segments based on the shock motions are listed in Table 7.1.

Figure 7.3 shows the mean velocity profiles derived from the two cameras with a 40 μs delay. The velocity profiles are similar to those discussed in chapter 5. Careful inspection of the figure shows that there is a small difference between the profiles obtained with the two cameras. As shown in Fig. 7.4, the mean velocity difference (Δu) varies from -0.9 m/s in the freestream to 2.1 m/s in the inner part of the boundary layer. (In the discussion below, the velocity difference Δu will be called the "acceleration" because it is directly proportional to it, i.e. $a=\Delta u/\Delta t$.) Since the time-delay is only 40 μs, it is unlikely that actual mean acceleration was present during the run. In fact, since each profile represents an average over the whole run, they should ideally be identical. The fact that they are not identical means that there is a small but systematic bias in the camera registration. Since the flow acceleration is approximated as $a=\Delta u/\Delta t$, this difference in the mean velocity would be interpreted as mean flow acceleration. Several instantaneous acceleration profiles are shown in Fig. 7.5. The figure shows that the instantaneous acceleration varies from -40 to 60 m/s, which is significantly larger than the system bias. This suggests that the system bias should not greatly affect the accuracy of the instantaneous acceleration measurements.

To provide further validation of the current set of experiments, conditional ensemble average profiles of the streamwise velocity fluctuations in the incoming boundary layer conditioned on the separation shock foot motion, were calculated and shown in Fig. 7.6. Similar results were shown in chapter 6, which were computed using the independently obtained wide-field PIV data. Although these profiles have relatively large precision uncertainty (see Appendix A), systematic trends can be seen that are similar to those of Fig. 6.14.

Figure 7.7 shows six instantaneous acceleration vector fields for the case when the shock moves downstream one pressure transducer within a 240 μs window. Here the instantaneous acceleration is defined as the velocity difference, $\Delta\vec{v}$, which is a vector quantity. The common feature for all these acceleration vector fields is that the acceleration is very small in the freestream, whereas there are large variations of the acceleration within the boundary layer. For example, Fig. 7.7a has significant positive acceleration, whereas Fig. 7.7b has significant negative acceleration. It is clear from such acceleration fields that there is no obvious systematic direction of acceleration that is associated with downstream shock foot motion.

The possible relationship between the upstream acceleration and the shock motion is further explored by plotting conditional ensemble average streamwise acceleration profiles in the incoming boundary layer for different shock foot motion within a time period of: 480, 240, and 120 μs. These plots are shown in Fig. 7.8. Because of the small number of segments, the profiles exhibit large uncertainty, and therefore no meaningful relationship can be identified between the acceleration and shock motion.

The potential relationship between acceleration and the change in direction of the shock foot motion (turn-around) was also investigated. Figure 7.9 shows the conditional ensemble average profiles of the streamwise acceleration in the incoming boundary layer for cases when the separation shock foot changed direction within a time period of 240 μs. There is some indication, in the outer part and inner part of the boundary layer, that the acceleration is negative for shock motion changing direction from downstream to upstream and vice versa. However, this picture is blurred by the profiles at the middle part of the boundary layer, i.e., from y=3 to 10 mm. This indicates that there may be some relationship between the upstream acceleration with the shock turn-around, but the relationship is likely weak.

In summary, no meaningful relationship between acceleration in the upstream boundary layer and shock-foot motion could be found. These data were clearly limited by the high precision uncertainty of the measurements. The large uncertainty is a little surprising because about 350 segments were used for each profile and each segment contains a row of 30 vectors for a total of about 10,000 points. Obviously, as discussed in Appendix A, not all of those points are independent and so the effective number of data points may be an order of magnitude lower. Furthermore, it is well known that differentiation is a noise enhancing process, and differentiation is being approximated by differencing, this process is also likely noise enhancing. This probably has the effect of increasing the number of data points that are required to obtain statistical convergence. Certainly these results suggest that PIV is not well suited for generating this type of statistical data. It seems clear that a continuous point measurement technique would give superior results because a great deal more data could be taken at a given point in the flow. This problem was recognized early in the study, but it was hoped that the acceleration / shock motion would be strong enough that it could be observed even with relatively large measurement uncertainty. It can be concluded then that any such correlation is likely not large, but this study cannot rule out its existence.

Table 7.1 The numbers of segments obtained for each shock motion.

	2.1 kHz (480 μs window)	4.2 kHz (240 μs window)	8.3 kHz (120 μs window)
Downstream to upstream	130	37	5
Upstream to downstream	256	73	14
Upstream 2 pressure transducers	65	27	5
Upstream 1 pressure transducers	341	358	232
No motion	738	1181	1601
Downstream 1 pressure transducers	353	363	256
Downstream 2 pressure transducers	75	34	3

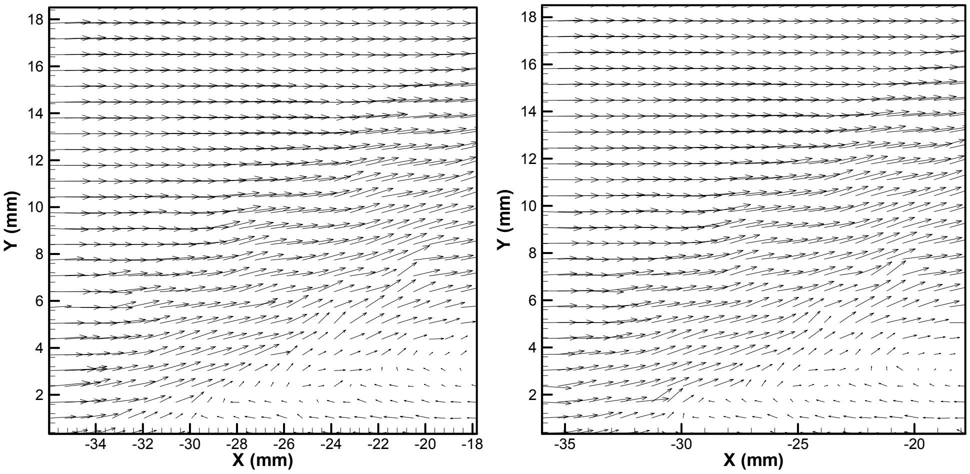

(a) (b)

Figure 7.1. Sample instantaneous vector fields for the time-sequenced PIV validation experiments. The time delay between PIV images is zero. (a) First camera, (b) Second camera.

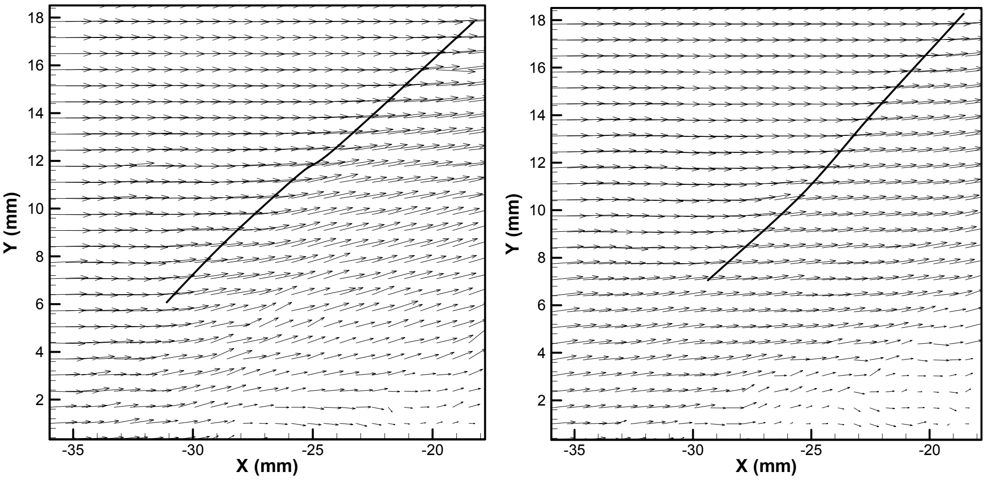

(a)

Figure 7.2. (See caption next page.)

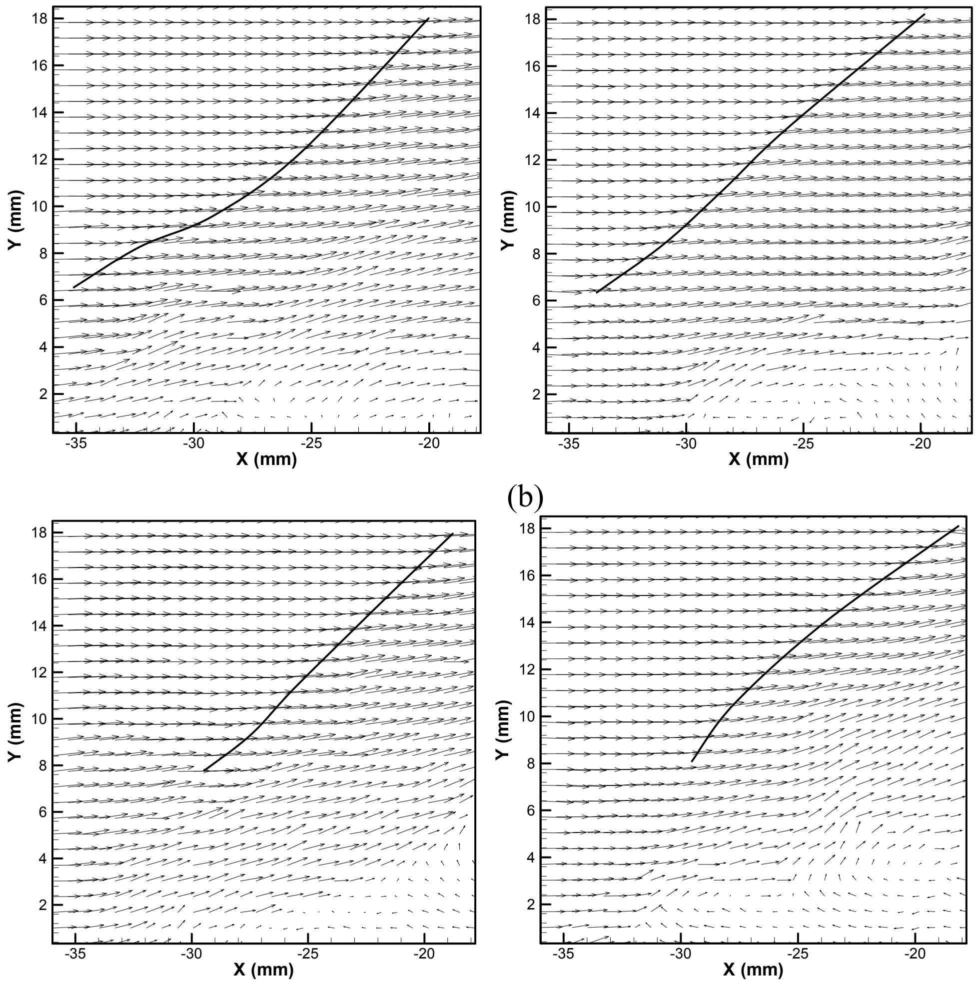

(b)

(c)

Figure 7.2. Velocity vectors for time-sequenced PIV pairs separated in time by 40 μs. (a-c) are different realizations. The image at right was taken 40 μs after the image at left.

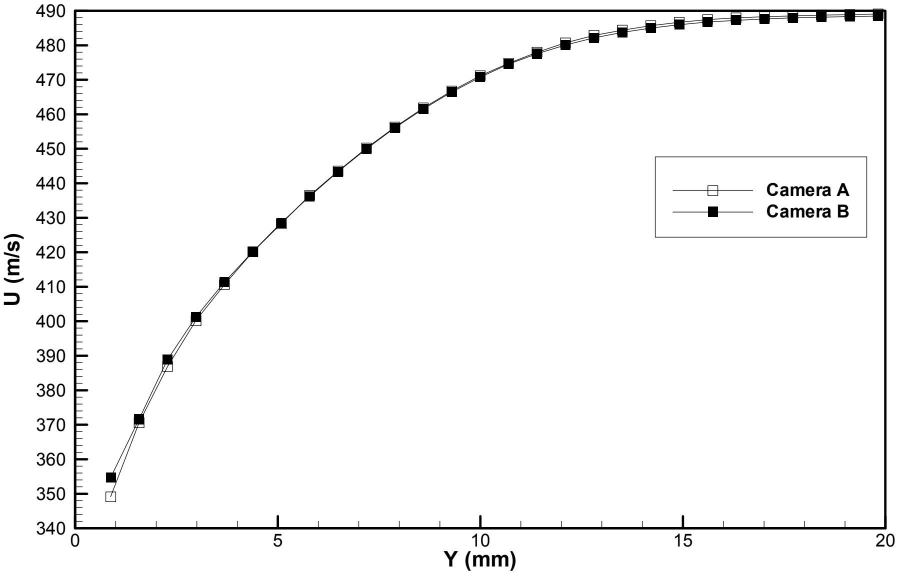

Figure 7.3 Mean velocity profiles for the two cameras. The time between vector fields was 40 μs.

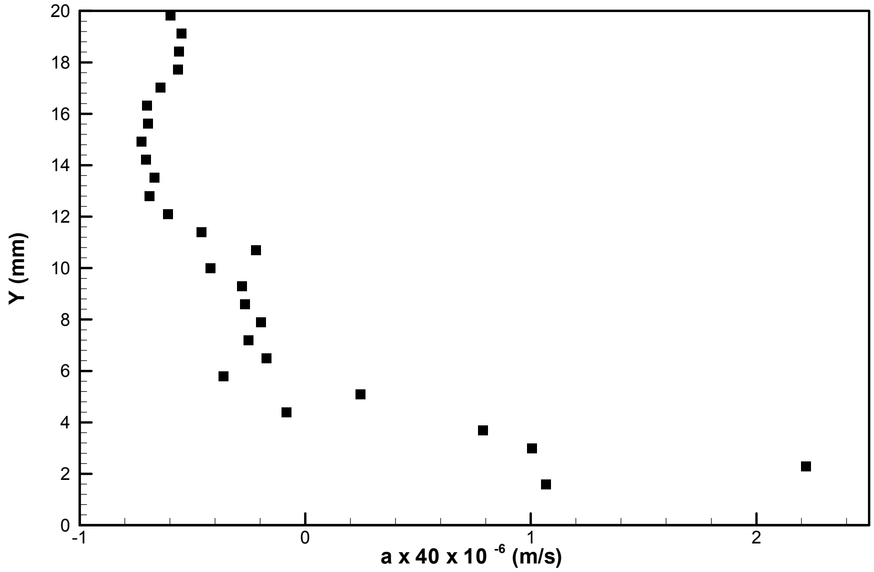

Figure 7.4 Mean velocity difference (Δu) profile across the boundary layer. The velocity difference is proportional to the acceleration ($a=\Delta u/\Delta t$).

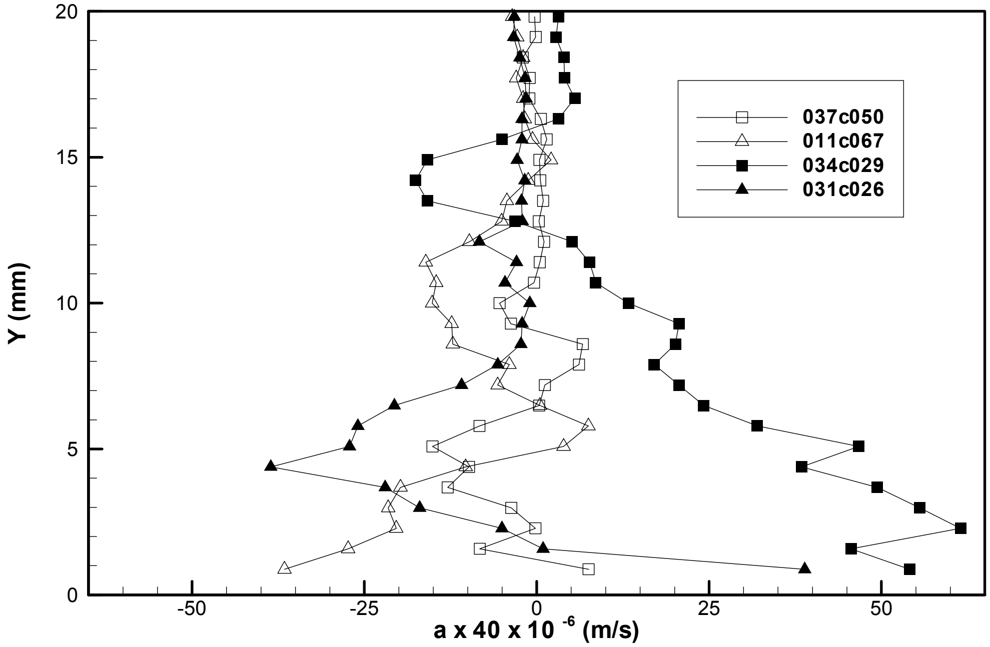

Figure 7.5 Sample instantaneous acceleration profiles.

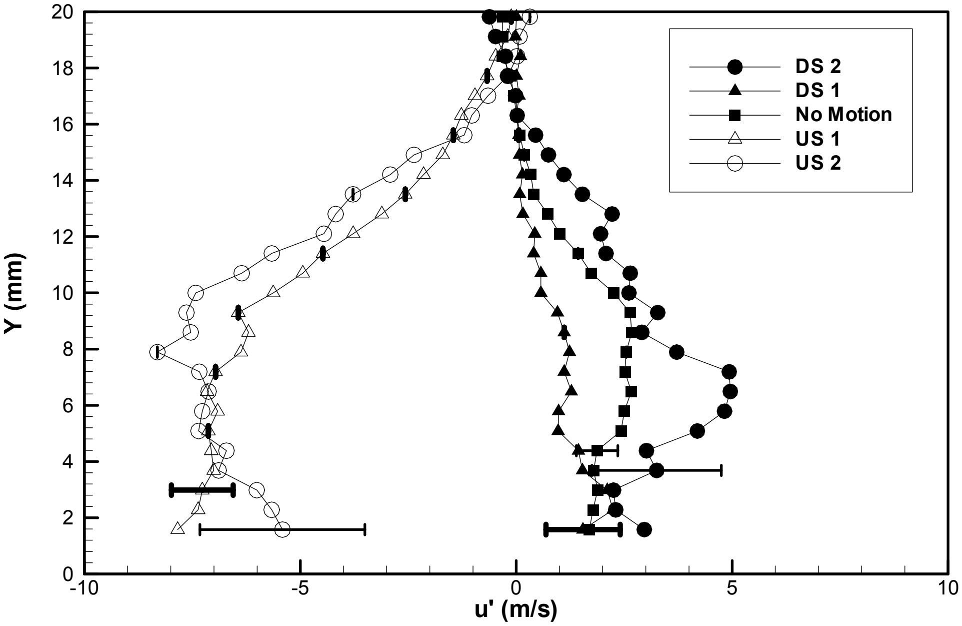

(a)

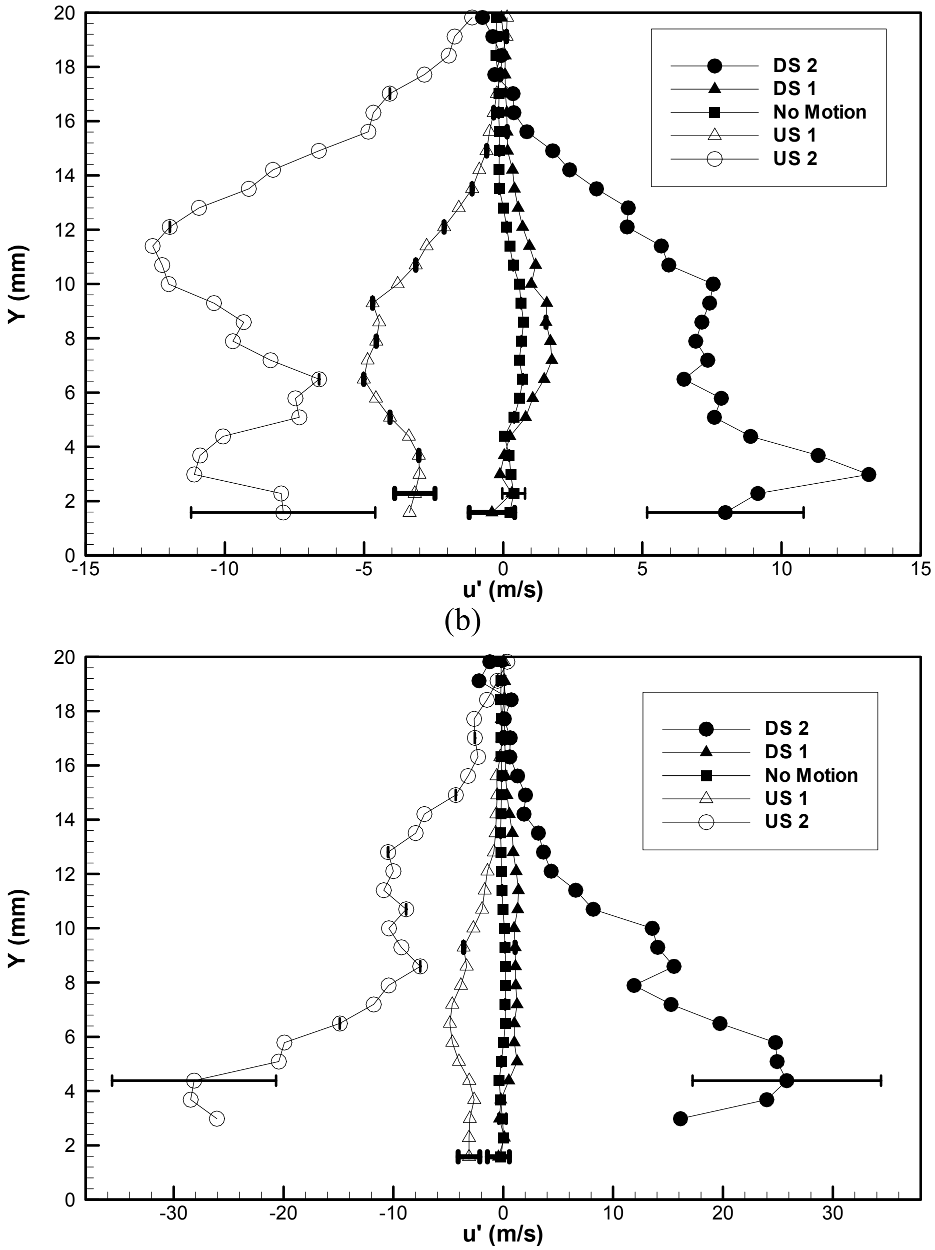

(b)

(c)

Figure 7.6 Conditional ensemble average profiles of the streamwise velocity fluctuations in the incoming boundary layer conditioned on the separation shock foot motion within a time period of: (a) 480; (b) 240; and (c) 120 μs. (20^{o} ramp in Mach 2 flow).

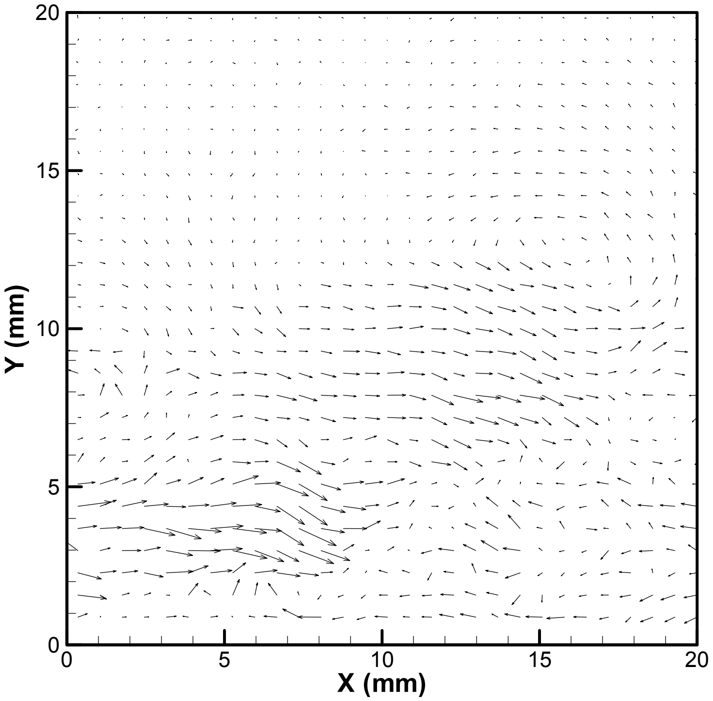

(a)

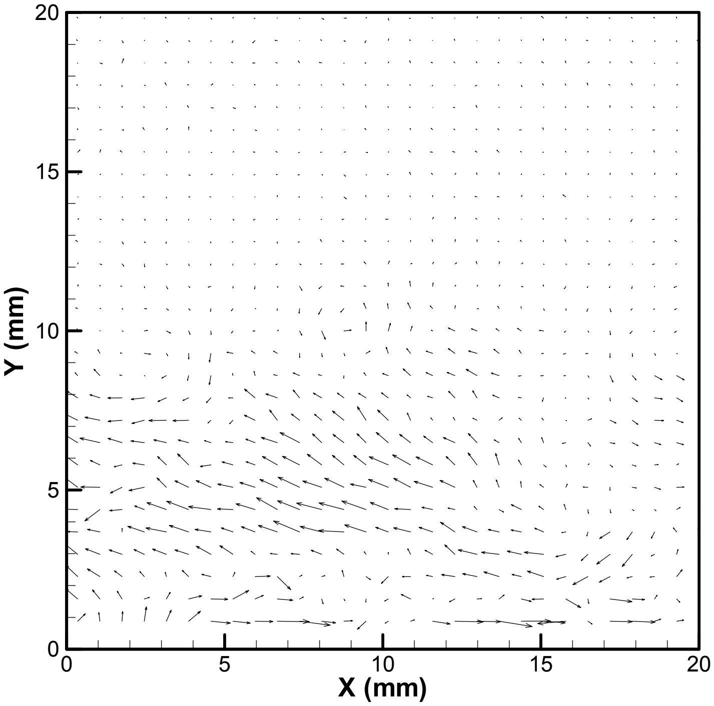

(b)

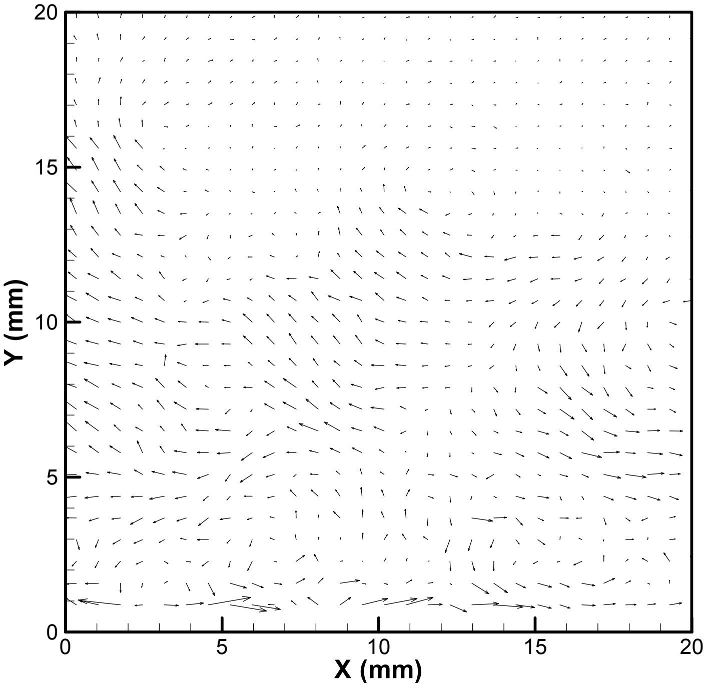

(c)

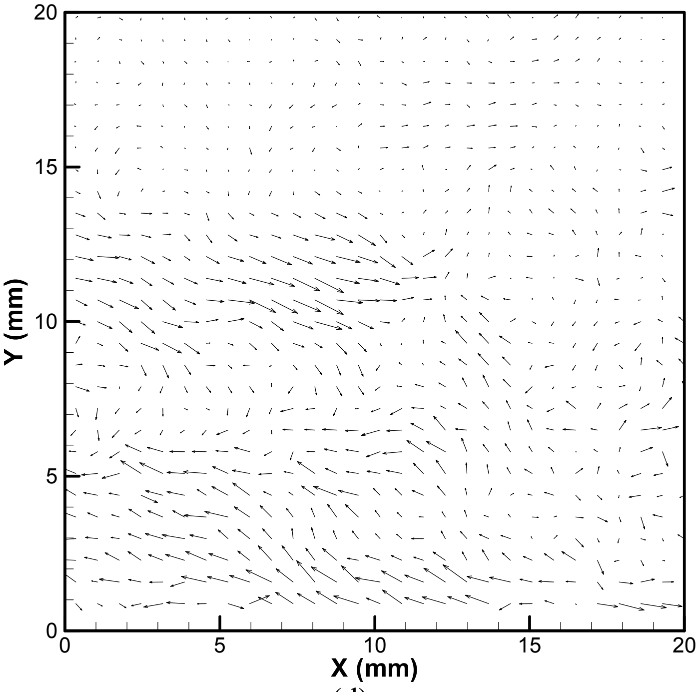

(d)

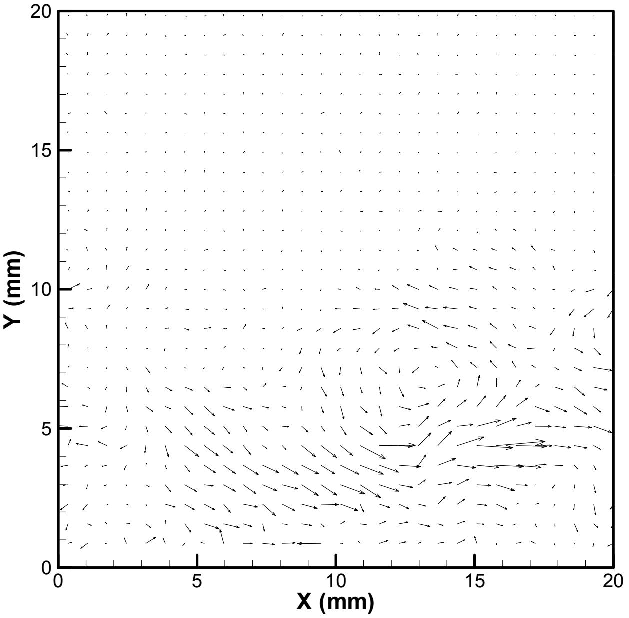

(e)

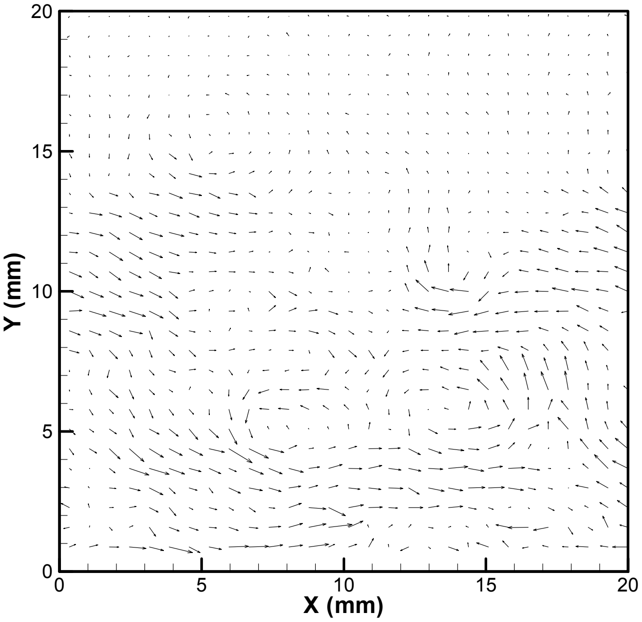

(f)

Figure 7.7 Instantaneous acceleration vector fields for shock moving downstream one pressure transducer within 240 μs (4.2 kHz window).

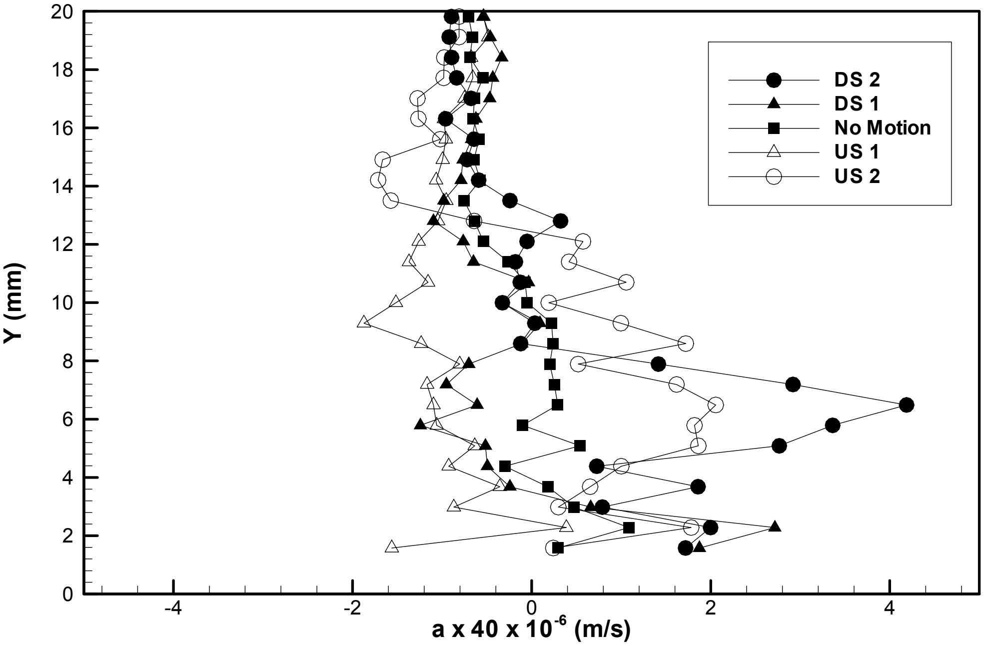

20
18
16
14
12
10
8
6
4
2
0
Y (mm)
-4
-2
0
2
4
a x 40 x 10^{-6} (m/s)
DS 2
DS 1
No Motion
US 1
US 2

(a)

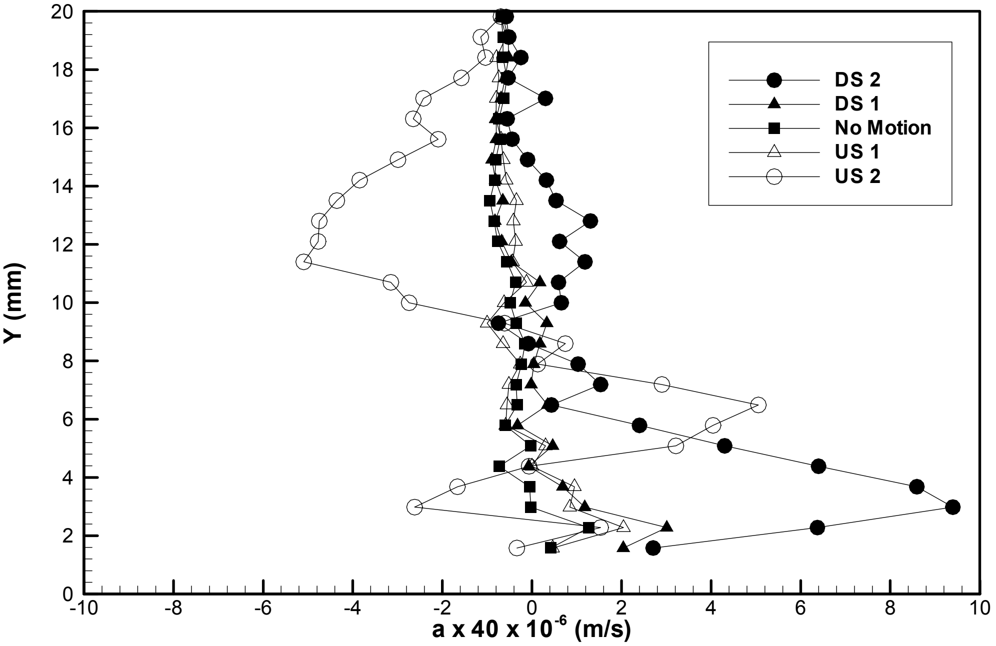

20
18
16
14
12
10
8
6
4
2
0
Y (mm)
-10
-8
-6
-4
-2
0
2
4
6
8
10
a x 40 x 10^{-6} (m/s)
DS 2
DS 1
No Motion
US 1
US 2

(b)

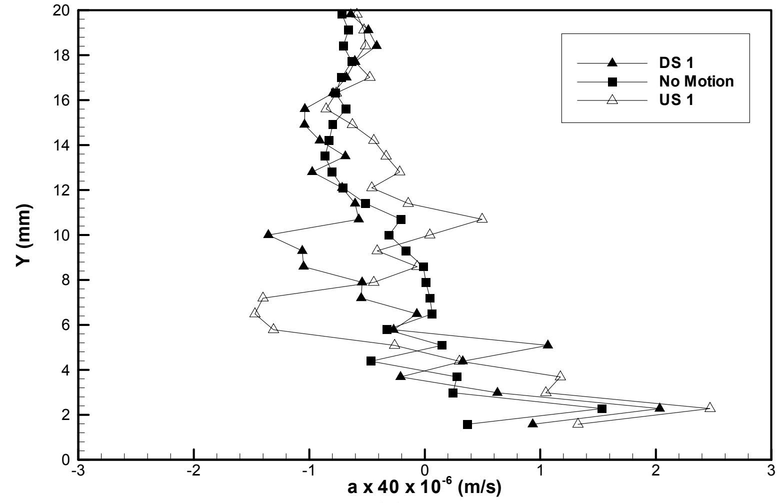

(c)

Figure 7.8 Conditional ensemble average profiles of the streamwise acceleration in the incoming boundary layer conditioned on the separation shock foot motion within a time period of: (a) 480; (b) 240; and (c) 120 μs. (20^{o} ramp in Mach 2 flow).

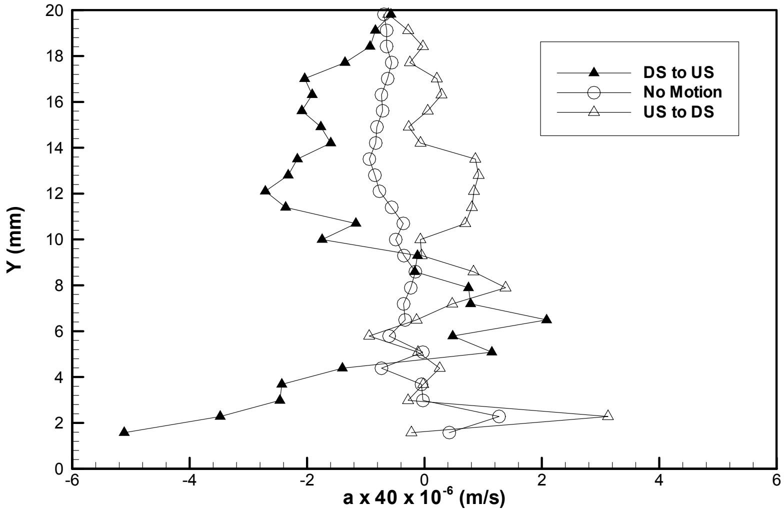

Figure 7.9 Conditional ensemble average profiles of the streamwise acceleration in the incoming boundary layer conditioned on the separation shock foot changing direction within a time period of 240 μs. (DS to US means shock changes moving direction from downstream to upstream)

Chapter 8

Summary and Conclusions

The objective of this study was to develop a new multi-camera, multi-laser PIV system and use it to gain new insight into the physics of shock-induced turbulent boundary layer separation. Therefore, a major portion of this dissertation is devoted to a discussion of the design, characterization and validation of the PIV system in the Mach 2 wind tunnel. The validation involved an investigation of different seed particles and careful measurements of the particle response time. Measurements of the upstream Mach 2 boundary layer were also made as further validation of the PIV technique and to characterize the boundary layer for the SWTBLI studies. The new PIV system was used to study unswept compression ramp SWTBLIs, with a focus on understanding how the global flow structure is related to the shock-foot dynamics. A summary of this work is given below.

8.1 MULTI-LASER AND MULTI-CAMERA PIV SYSTEM

The multi-laser, multi-camera PIV system was developed and applied successfully in the Mach 2 wind tunnel. This system can be used in three different configurations: "wide-field" (4k×1k pixels obtained by having 4 cameras side by side), "medium-field" (2k×1k pixels obtained with 2 cameras side by side) and "narrow-field" (1k×1k pixels, obtained with a single camera). Time sequenced-PIV can be used for the medium-field (two-image sequence) and narrow-field (four-image sequence) configurations, and can provide information on flow dynamics, such as structure evolution or separation shock motion. The time separation between two pairs of PIV velocity fields can vary from 30 μs to 150 μs, due to the limitation of the FLC light shutter response frequency and double pulsed laser energy. This range of times is sufficient for the purpose of studying SWTBLI dynamics since the shock motion occurs with frequencies that are typically less than 10 kHz (≥100 μs). The response time of the PIV particles, titanium dioxide (TiO_2) P25, has been estimated from both oblique shock and bow shock flow fields. The particle time constant is estimated as 2.3-3.2 μs, which gives a Stokes number of about 0.1-0.15 in the current Mach 2 SWTBLI, which shows that the particles can faithfully track the large-scale velocity fluctuations.

8.2 MACH 2 BOUNDARY LAYER PROFILES FROM PIV MEASUREMENT

The PIV system was further tested by making measurements of the undisturbed Mach 2 turbulent boundary layer on the test section floor upstream of the interaction. The flow field parameters are listed in table 5.1. The skin friction coefficient was obtained by fitting the mean velocity data to the model proposed by Sun and Childs (1973, 1976). When plotted in inner (wall) variables and with the transformed velocity U^*, the mean profile agreed well with the incompressible law-of-the-wall. The RMS velocity profiles, normalized using Morkovin's scaling, agree well with profiles from other sources, i.e., the Mach 2.32 boundary layer results measured with LDA by Elena and Lacharme (1988). A local maximum in the RMS profile was observed and is believed to be the "second peak" that has been previously observed in high Reynolds number incompressible boundary layers (Smits and Dussauge 1996).

8.3 WIDE-FIELD PIV MEASUREMENT OF SWTBLI

The PIV system was used to obtain wide-field velocity measurements of a Mach 2 compression ramp interaction simultaneous with fast response pressure measurements under the intermittent region. The wide-field PIV enabled the imaging of the entire interaction, spanning the upstream boundary layer, intermittent region, separated flow and the reattachment region on the ramp face.

The instantaneous vector fields reveal complex flow features that exhibit large variations from image to image. The velocity fluctuations in the upstream boundary layer are seen to be relatively small, whereas substantially larger fluctuations exist in the regions of separated flow and reattachment. The separated flow region exhibits large instantaneous reverse-velocities and large velocity fluctuations in the shear layer above it. In only a few images can a clear point of reattachment on the ramp face be observed. It was further observed that the separation shock wave location inferred from the PIV images agreed well with the shock-foot position inferred from the pressure data. Furthermore, the shock foot did not necessarily result in immediate downstream separation of the boundary layer as had been proposed by previous researchers. Instead, it was observed that the flow downstream of the shock foot could be separated, separated only well downstream of the shock foot, or even remain attached through the entire interaction.

The unconditional average velocity fields show no indication of reverse-flow. The reason for a lack of mean reverse flow is that the region of reverse flow was probably too small for the PIV system to resolve. This conclusion is based on previous studies that suggest the region of reverse-flow would be confined to a region about 1 mm from the wall, which is near the limit of the PIV resolution.

The relationship between the interaction global structure and the shock foot location was investigated by computing conditional-average vector fields, which were conditioned upon the shock-foot location. The conditional averages show that when the shock is upstream, the scale of the separated flow, the velocity fluctuations and the domain of perturbed flow, are all substantially larger than when the shock-foot is located downstream.

An important finding of this study is that there is a clear correlation between the thickness of the upstream boundary layer and shock foot position. Specifically, a thicker upstream boundary layer is associated with an upstream shock location and *vice versa*. This observation contradicts the previous study by Beresh et al. (2002) who studied Mach 5 compression ramp interactions by using PIV. Interestingly, the current data do support the primary finding of Beresh et al. (2002) that the shock motion is correlated with low-frequency velocity fluctuations in the lower part of the upstream boundary layer. The reason proposed for this apparent contradiction is that the correlation between velocity fluctuations and shock motion is the primary one, and was correctly measured by Beresh et al. Furthermore, it is proposed that in naturally developing boundary layers, the low-frequency fluctuations tend to be associated with variations in the thickness of the boundary layer. However, in the case of Beresh et al. they used an intrusive injector in the test section to seed their particles, and therefore the turbulence induced by the injector may have decoupled the fluctuations in the lower part of the boundary layer from variations in its thickness.

The correlation between the thickness of the upstream boundary layer and the shock foot position and the correlation between shock motion and the low-frequency velocity fluctuations in the upstream boundary layer may be close related and both caused by the upstream global low frequency large-scale turbulent structures. This idea, however, need to be studied with more specially designed experiment.

It was further observed that in the current study and in two others, measurements showed that larger velocity fluctuations are correlated with upstream shock foot motion than with downstream shock foot motion. This observation, which has not been noted previously, suggests there is an inherent asymmetry in the way the separation shock responds to upstream velocity fluctuations; i.e. it offers more resistance to upstream motion than to downstream motion.

8.4 TIME-SEQUENCED NARROW FIELD PIV MEASUREMENT

The multi-camera, multi-laser PIV system was used in two “proof-of-concept” experiments to use time-sequenced imaging to study flow dynamics. In the first experiment, the two time-sequenced PIV vector fields were obtained of the intermittent region, where the time between vector fields was 40 µs. This set of experiments proved that time-sequenced PIV can be used effectively to study flow dynamics, such as changes in the separation shock shape, development of separation and the convection of large-scale turbulent structures.

In another set of experiments, a preliminary study was conducted to test the hypothesis that the rate of change of the velocity profile (or upstream acceleration, $\Delta u/\Delta t$), is correlated with shock motion in a Mach 2 compression ramp interaction. This was accomplished by capturing images of the same field of view with a time delay between images of 40 μs. The results show no meaningful relation between upstream acceleration with the large-scale shock motion. The results seem to imply a weak relationship between upstream acceleration and shock turn-around events, but the data are not conclusive because of inadequately converged statistics. The failure to find a clear relationship between upstream acceleration and shock foot motion in this study does not rule out the possibility that such a relationship exists because the experiments were limited in the amount of data that could be collected.

8.5 FUTURE WORK

Future work could involve improving on the measurements that were discussed in this dissertation and conducting new measurements to investigate phenomena that could not be studied with the current methods. For example, for some quantities, such as correlations between the shock motion and velocity/acceleration fluctuations, the statistics were not sufficiently converged and so the data exhibited large precision uncertainties. Although this would be a cumbersome task, this could be improved by taking larger data sets, or by using an alternative technique to detect the upstream fluctuations. It may actually be preferable to use hot-wire anemometry to detect mass flux fluctuations in the upstream boundary layer and to relate them to the shock foot motion. Such data would provide an interesting complement to the PIV data, which is best used to study the relationship between flow structures.

The wide-field PIV system is a very powerful tool and should be used to study a number of different SWTBLIs, including those generated by cylinders, blunt fins, swept ramps, glancing shocks, etc. Because the type of data that result from wide-field PIV has never before been captured in these flows, new insights would likely result from such an effort. The multi-camera, multi-laser system has not been used to its full capabilities. In particular, it would be nice to capture four-time-sequenced PIV vector fields to study structure dynamics in SWTBLIs. In particular it would be illuminating to see how structures in the upstream boundary layer respond as they pass through the separation shock. Alternatively, it would be useful to operate the PIV system to do “Lagrangian structure tracking”. In this configuration, four cameras are located side-by-side and each camera detects laser pulses with a different time delay, so that a single structure can be tracked as it convects past the four cameras. This configuration could be used to track a turbulent structure as it convects from the upstream boundary layer, through the separation shock, over the separated flow and through the reattachment region. This would prove extremely useful for understanding how shock waves interact with turbulent structures.

The flow field structures close to the shock foot have been seen to change greatly within 40 μs. Time-sequenced PIV measurement with simultaneous pressure transducer measurement in the intermittent region will allow us have a much better understanding of the shock foot motion. The current PIV system, which can take up to 4 velocity fields within each cycle, is good enough for this purpose.

Appendix A

Uncertainty Analysis

PIV uncertainty analysis can be found in many references and will be briefly reviewed here. Beresh (1999) discussed the magnitudes of several sources of uncertainty: 0.2% for laser pulse separation time; 0.2% for determination of the field-of-view of the camera by imaging the ruler, and 0.1 pixel (~0.5% in the current experiment) for the PIV data reduction algorithm. The uncertainty sources in the PIV data reduction algorithm include out-of-plane motion, variations in the particle images from one exposure to the next, non-spherical particle images, particle image diameter, and irregularities in the laser sheet or the CCD array sensitivity (Huang et al. 1997, Westerweel 1997, 2000). The intrinsic (measurement system) uncertainty of the PIV technique is found by computing the root-sum-squares value, i.e., δ_{piv}=0.6%.

Much of the data presented in chapters 6 and 7 is in statistical form. Because the number of PIV images that were required is limited, the precision uncertainty was typically limited by the limited sample size and run-to-run variations, rather than the uncertainty of the PIV algorithm. All precision uncertainties reported for the mean values were 95% confidence levels and were computed as follows:

Assume that M segments (individual PIV vector fields) contributed to the sample used to compute the mean value, $\bar{x}$. Each PIV field contains 30×30 vectors and since typically transverse profiles were computed, each row of 30 vectors was averaged to improve the statistical convergence. Therefore, there were a total of N=30M total samples, x_i, that contributed to the average value, $\bar{x}$. The mean value was computed as:

$$\bar{x} = \frac{1}{N}\sum_{1}^{N} x_i$$

The precision uncertainty in $\bar{x}$ is given by:

$$\delta_x = \pm 2\frac{S_x}{\sqrt{N}} \quad \text{(95\% confidence)}$$

where S_x is the sample standard deviation defined as:

$$S_x = \left[\frac{1}{N-1}\sum_{1}^{N}(x_i - \bar{x})^2\right]^{1/2}$$

The total uncertainty is given by computing the root-sum-squares value from the intrinsic and precision uncertainties:

$$\delta = \sqrt{\delta_{piv}^2 + \delta_x^2}$$

The unconditional sampling uncertainties for the mean velocity, fluctuation velocity, and acceleration are shown in Figs. A.1, A.2, and A.3 respectively. The total number of samples is 2770 from 30 runs. The relative uncertainty for the mean velocity, shown in Fig. A.1, is 2% at the freestream and 7.5% close to the wall. The uncertainty in the velocity fluctuations, shown in Fig. A.2, is about ±5 m/s in the freestream and increases to about ±15 m/s close to the wall. Figure A.3 shows that for acceleration the uncertainty is about ±2 m/s in the freestream and increases to about ±14 m/s close to the wall.

The conditional sampling uncertainties for the velocity fluctuations and acceleration are shown in Fig. A.4 and Fig. A.5. The conditional sampling uncertainties are still calculated from 30 runs with the total number of samplings listed in Table 7.1.

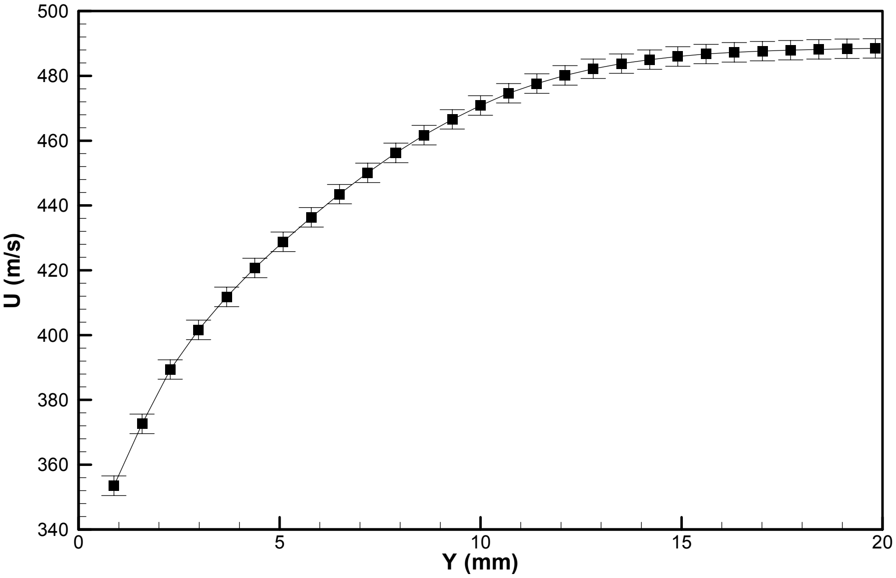

Figure A.1 Precision uncertainty for PIV measurement of Mach 2 boundary layer mean velocity profile.

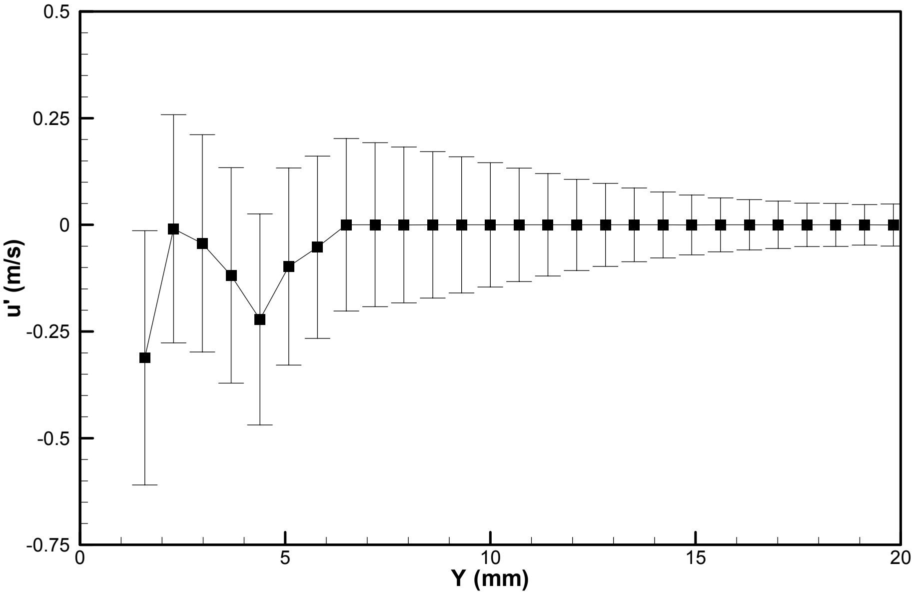

Figure A.2 Precision uncertainty for PIV measurement of Mach 2 boundary layer unconditional averaged velocity fluctuations profile.

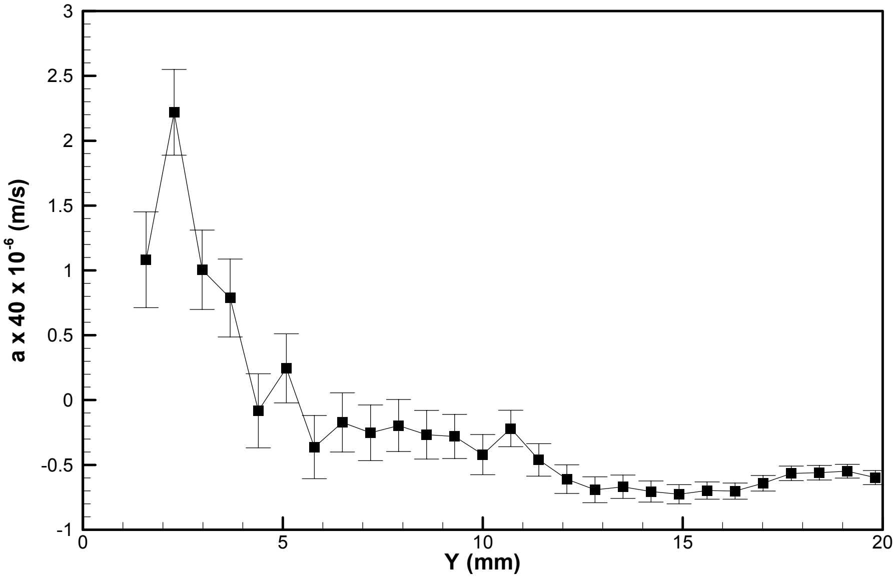

Figure A.3 Precision uncertainty for PIV measurement of Mach 2 boundary layer unconditional averaged acceleration profile.

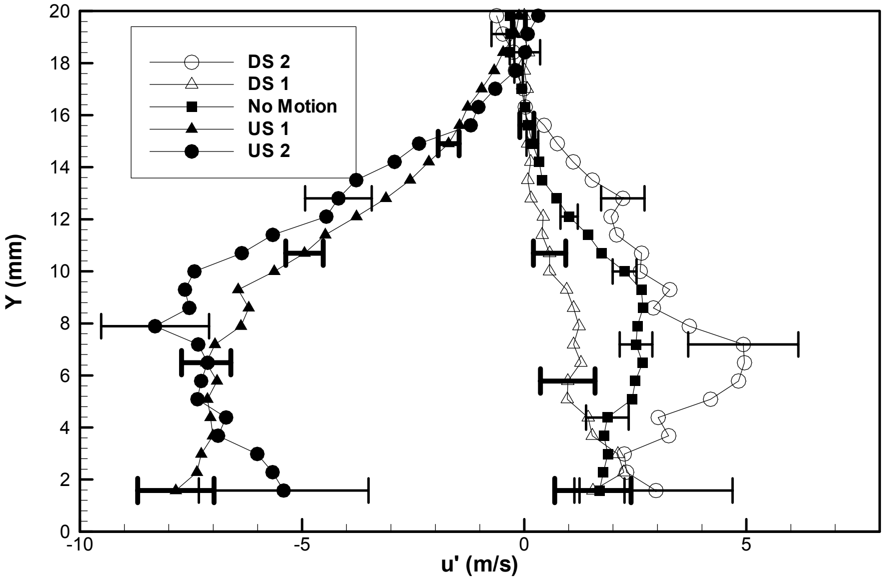

Figure A.4 Precision uncertainty of conditional averaged velocity fluctuations profiles for shock motions in a 480 μs window.

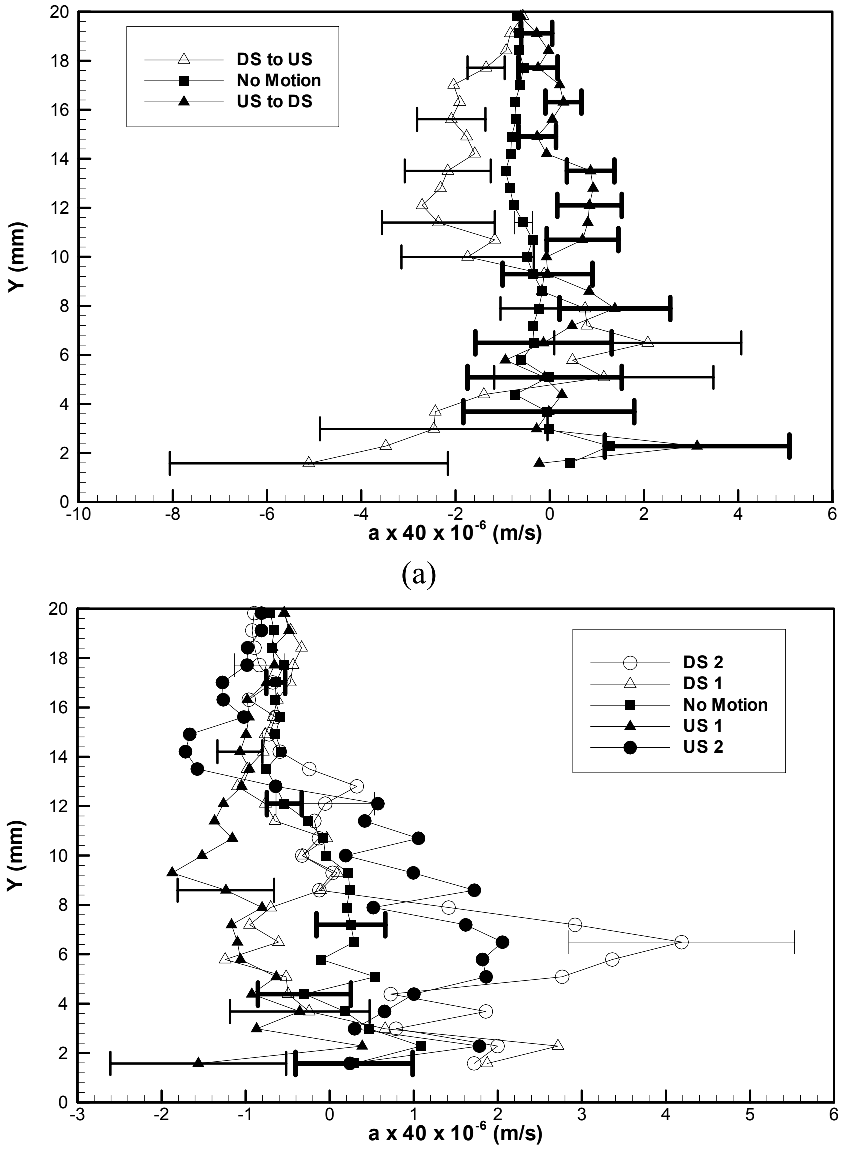

(a)

(b)

Figure A.5 Precision uncertainty of conditional averaged acceleration velocity profiles: (a) Shock changing direction in a 240 μs window, and (b) Shock motions in a 480 μs window.

References

Adams, N.A., (1998), "Direct Numerical Simulation of Turbulent Compression Ramp Flow", Theoret. Comput. Fluid Dynamics, 1998, Vol. 12, pp. 109-129.

Adams, N. A., (2000), “Direct simulation of the turbulent boundary layer along a compression ramp at M = 3 and $Re_\theta = 1685$”, Journal of Fluid Mechanics, Vol. 420, 2000, pp. 47-83.

Adamson, T. C. Jr. and Messiter, A. F., (1980), "Analysis of Two-Dimensional Interactions Between Shock Waves and Boundary Layers", Annual Review of Fluid Mechanics, Vol. 12, pp. 103-138, 1980.

Alkislar, M. B., Lourenco, L. M., and Krothapalli, A., (2000), “Stereoscopic PIV Measurements of a Screeching Supersonic Jet,” Journal of Visualization, Vol. 3, No. 2, 2000, pp. 135-143.

Andreopoulos, J., and Muck, K.D., (1987), "Some New Aspects of the Shock Wave/Boundary Layer Interaction in Compression Ramp Flows", Journal of Fluid Mechanics, Vol. 180, 1987, pp. 405- 428.

Andreopoulos, Y., Agui, J. H. and Briassulis, (2000), "Shock Wave-Turbulence Interaction", Annual Review of Fluid Mechanics, vol. 32, pp. 309-345, 2000.

Ardonceau, P. L., (1984), "The Structure of Turbulence in a Supersonic Shock-Wave / Boundary-Layer Interaction," AIAA Journal, Vol. 22, No. 9, pp. 1254-1262, September 1984.

Beresh, S. J., Comninos, M., Clemens, N. T., and Dolling, D. S., (1998), “Incoming turbulent boundary layer structure on a shock-induced separated flow”, AIAA Paper 99-0620, 36th Aerospace Sciences Meeting and Exhibit, Reno, NV, January 12-15, 1998.

Beresh, S.J., (1999), "The Effect of the Incoming Turbulent Boundary Layer on a Shock-Induced Separation Flow Using Particle Image Velocimetry", PhD dissertation, Department of Aerospace Engineering and Engineering Mechanics, The University of Texas at Austin.

Beresh, S. J., Clemens, N. T., and Dolling, D. S., (1999), "The relationship between upstream turbulent boundary layer velocity fluctuations and separation shock unsteadiness", AIAA Paper 99-0295, 37th Aerospace Sciences Meeting and Exhibit, Reno, NV, January 11-14, 1999.

Beresh, S.J., Clemens, N.T. and Dolling, D.S., (2002), "Relationship Between Upstream Turbulent Boundary - Layer Velocity Fluctuations and Separation Shock Unsteadiness", AIAA Journal, Vol. 40, No. 12, December 2002, pp. 2412-2422.

Bradshaw, P., (1977), "Compressible Turbulent Shear Layers", Annual Review of Fluid Mechanics, Vol. 9, 1977, pp. 33-54.

Brusniak, L, and Dolling, D. S., (1994), "Physics of Unsteady Blunt-Fin-Induced Shock Wave / Turbulent Boundary Layer Interactions," Journal of Fluid Mechanics, Vol. 273, August 25, 1994, pp. 375-409.

Cebeci, T. and Bradshaw, P., (1984), "Physical and Computational Aspects of Convective Heat Transfer", Springer-Verlag.

Chan, S. C., (1996), "Planar Laser Scattering Imaging of Shock Wave Turbulent Boundary Layer Interactions," M. S. Thesis, Department of Aerospace Engineering and Engineering Mechanics, The University of Texas at Austin, November 1996.

Degrez, G., (1981), "Exploratory Experimental Investigation of the Unsteady Aspects of Blunt Fin-Induced Shock Wave Turbulent Boundary Layer Interactions", M.S.E. Thesis (1516-T), Dept. of Mechanical and Aerospace Engineering, Princeton University, Princeton, N. J., June 1981.

Disimile, P. J. and Scaggs, N. E., (1989), "High Reynolds Number Wedge-Induced Separation Lengths at Mach 6", AIAA Journal, Vo. 27, No. 12, December 1989, pp. 1827-1828.

Doerffer, P. P. and Bohning, R., (2003), "Shock Wave - Boundary Layer Interaction Control by Wall Ventilation", Aerospace Science and Technology, 2003, No. 7, pp. 171-179.

Dolling, D.S. and Bogdonoff, S.M., (1981), "Scaling of Interactions of Cylinders With Supersonic Turbulent Boundary Layers", AIAA journal, Vol. 19, No. 5, May 1981, pp. 655-657.

Dolling, D. S., and Bogdonoff, S. M., (1982), "Blunt Fin-Induced Shock Wave/Turbulent Boundary-Layer Interaction", AIAA Journal, Vol. 20, No. 12, December 1982, pp. 1674-1680.

Dolling, D. S., and Murphy, M. T. (1983), "Unsteadiness of the Separation Shock Wave Structure in a Supersonic Compression Ramp Flowfield," AIAA Journal, Vol. 21, No. 12, pp. 1628-1634, December 1983.

Dolling, D. S., and Or, C. T., (1985), "Unsteadiness of the Shock Wave Structure in Attached and Separated Compression Ramp Flows," Experiments in Fluids, Vol. 3, pp. 24-32, 1985.

Dolling, D. S., and Brusniak, L., (1989), "Separation Shock Motion in Fin, Cylinder, and Compression Ramp Induced Turbulent Interactions," AIAA Journal, Vol. 27, No. 6, June 1989, pp. 734-742.

Dolling, D. S., (1993a), "Fluctuating Loads in Shock Wave / Turbulent Boundary Layer Interaction: Tutorial and Update," AIAA Paper 93-0284, 31st Aerospace Sciences Meeting and Exhibit, Reno, NV, January 11 - 14, 1993.

Dolling, D. S., (1993b), “Unsteady Phenomena in Shock Wave/Boundary Layer Ineraction”, AGARD Report 792, 1993.

Dolling, D.S., (2000), “50 years of shock wave/boundary layer interaction - what next?”, AIAA paper 2000-2596, 19-22, June 2000, Denver, CO.

Elavarasan, R., Krothapalli, A., Venkatakrishnan, L., and Lourenco, L., (2001), “Suppression of Self-Sustained Oscillations in a Supersonic Impinging Jet,” AIAA Journal, Vol. 39, No. 12, 2001, pp. 2366-2373.

Elena, M. and Lacharme, J. P., (1988), "Experimental Study of a Supersonic Turbulent Boundary Layer Using a Laser Doppler Anemometer", Journal de Mecanique theorique et appliquee, (Journal of Theoretical and Applied Mechanics), Vol. 7. No. 2, 1988, pp.175-190.

Erengil, Mehmet E., and Dolling, David S., (1991a), “Unsteady wave structure near separation in a Mach 5 compression ramp interaction”, AIAA Journal, Vol. 29, No. 5, May 1991, pp. 728-735.

Erengil, M. E., and Dolling, D. S. (1991b), "Correlation of Separation Shock Motion with Pressure Fluctuations in the incoming Boundary Layer," AIAA Journal, Vol. 29, No. 11, November 1991, pp. 1868-1877.

Erengil, M.E. and Dolling, D.S., (1993a), "Effects of Sweepback on Unsteady Separation in Mach 5 Compression Ramp Interactions," AIAA Joumal, Vol. 31, No. 2, pp. 302-311, Feb. 1993.

Erengil, M.E., and Dolling, D.S., (1993b), "Physical causes of separation shock unsteadiness in shock wave/turbulent boundary layer interactions", AIAA paper 93-3134, July 1993.

Fernholz, H. H. and Finley, P. J., (1981), "A Further Commentary of Compressible Boundary Layer Data With a Survey of Turbulence Data", AGARDograph No. 263, 1981.

Garnier, E., Sagaut, P. and Deville, M., (2002), "Large Eddy Simulation of Shock/Boundary-Layer Interaction", AIAA Journal, Vol. 40, No. 10, October 2002, pp. 1935-1944.

Gramann, R. A., and Dolling, D. S., (1990), "Detection of Turbulent Boundary - Layer Separation Using Fluctuation Wall Pressure Signals", AIAA Journal, Vol. 28, No. 6, 1990, pp. 1052-1056.

Gefroh, D., Loth E., Dutton, C. and McIlwain, S., (2002), "Control of an Oblique Shock/Boundary-Layer Interaction with Aeroelastic Mesoflaps", AIAA Journal, Vol. 40, No. 12, December 2002, pp. 2456-2566.

Haertig, J., Havermann, M., Rey, C. and George, A., (2002), "Particle Image Velocimetry in Mach 3.5 and 4.5 Shock-Tunnel Flows," AIAA J., Vol. 40, No. 6, June 2002, pp. 1056-1060.

Hopkins, E. J., Keener, E. R. and Polek, T. E., (1972), "Hypersonic Turbulent Skin-Friction and Boundary-Layer Profiles on Nonadiabatic Flat Plates", AIAA Journal, Vol. 10, No. 1, Jan. 1972, pp. 40-48.

Horstman, C.C. and Owen, F. K., (1972), "Turbulent Properties of a Compressible Boundary Layer", AIAA Journal, Vol. 10, No. 11,1972, pp.1418-1424.

Huang, H., Dabiri, D., and Gharib, M., (1997), "On Errors of Digital Particle Image Velocimetry," Measurement Science Technology, Vol. 8, pp. 1427-1440, 1997.

Humphreys, W. M. Jr., Rallo, R. A., Hunter, W. W. Jr., and Bartram, S. M., (1993), “Application of Particle Image Velocimetry to Mach 6 Flows,” SPIE Vol. 2052 Laser Anemometry Advances and Applications, 1993, pp. 519-526.

Hung, C. M. and Buning, P. G., (1984), "Simulation of Blunt-Fin Induced Shock Wave and Turbulent Boundary Layer Interaction", AIAA-84-0457, AIAA 22nd Aerospace Sciences Meeting, January 9-12, 1984 / Reno, Nevada.

Hunt, D., and Nixon, D., (1995), "A very large-eddy simulation of an unsteady shock wave/turbulent boundary layer interaction", AIAA paper 95-2212, 1995.

Johnson, D. A., (1974), "Turbulence Measurements in a Mach 2.9 Boundary Layer Using Laser Velocimetry", AIAA Journal, Vol. 12, No. 5, 1974, pp. 711-714.

Johnson, D. A. and Rose, W. C., (1975), "Laser Velocimeter and Hot-Wire Anemometer Comparison in a Supersonic Boundary Layer", AIAA Journal, Vol. 13, No. 4, April 1975, pp. 512-515.

Kompenhans, J., and Höcker, R., (1988), “Application of Particle Image Velocimetry to High Speed Flows,” von Kármán Institute Lecture Series 1988-06, Belgium, March 1988, pp. 67-83.

Kistler, A. L., (1958), "Fluctuation Measurements In Supersonic Turbulent Boundary Layers", Ballistic Research Laboratories, Rep. 1052 and Phys. Fluids 2, 1959, (CAT 5803).

Knight, D. D., Horstman, C. C., Shapey,, B. and Bogdonoff, S. M., (1987), "Structure of Supersonic Flow Pass a Sharp Fin", AIAA Journal, Vol. 25, 1987, pp. 1331-1337.

Kuntz, D. W., Amatucci, V. A. and Addy, A. L., (1987), "Turbulent Boundary-Layer Properties Downstream of the Shock- Wave / Boundary- Layer Interaction", AIAA Journal, Vol. 25, No. 5, May 1987, pp. 668-675.

Kussoy, M. I., Horstman C. C. and Acharya M., (1978), "An Experimental Documentation of Pressure Gradient and Reynolds Number Effects on Compressible Turbulent Boundary Layers", NASA TM 78 488, (CAT 7802S)

Kussoy, M.I., Brown, J.D., Brown, J.L., Lockman, W.K. and Horstman, C.C., (1987), “Fluctuations and massive separation in three-dimensional shock-wave/boundary layer interactions,” Second International Symposium on Transport Phenomena in Turbulent Flows, 1987, The University of Tokyo, Hongo Bunkyo-ku, Tokyo 113, Japan, Oct. 25-29.

Lang, N., (1998), “PIV Measurements in Sub- and Supersonic Flow over Delta Wing Configuration ELAC,” Proceedings of the 8th International Symposium on Flow Visualization, Università degli Studi di Napoli Federico II, Sorrento, Italy, Paper 205, 1998.

McClure, W.B., (1992), "An Experimental Study of the Driving Mechanism and Control of the Unsteady Shock Induced Turbulent Separation in a Mach 5 Compression Comer Flow," PhD Dissertation, Department of Aerospace Engineering and Engineering Mechanics, The University of Texas at Austin, August 1992.

Marshall, T.A. and Dolling, D. S., (1992), “Computation of Turbulent, Separated, Unswept Compression Ramp Interactions”, AIAA Journal, Vol. 30, No. 8, August 1992. pp. 2056-2065.

Melling, A., (1997), “Tracer particles and seeding for particle image velocimetry,” Meas. Sci. Technol., Vol. 8, pp. 1406-1416, 1997.

Molezzi, M. J. and Dutton, J. C., (1993), “Application of Particle Image Velocimetry in High-Speed Separated Flows,” AIAA Journal, Vol. 31, No. 3, 1993, pp. 438-446.

Morkovin, M. V., (1962), "Effects of Compressibility on Turbulent Flows", Mecanique de la Turbulence, C.N.R.S., Paris, 1962, pp. 367-380.

Muck, K. C., Andreopoulos, J., and Dussauge, J. P., (1988), "Unsteady Nature of Shock-Wave / Turbulent Boundary-Layer Interaction," ALAA Journal, Vol. 26, No. 2, February 1988, pp. 179-187.

Müller, Jürgen; Mümmler, Rainer and Staudacher, Werner, (2001), "Comparison of Some Measurement Techniques for Shock-Induced Boundary Layer Separation", Aerosp. Sci. Technol. Vol. 5, 2001, pp. 383-395.

Ong, C. and Knight, D., (1987), "Hybrid MacCormack and Implicit Beam-Warming Algorithms For a SuperSonic Compression Corner", AIAA Journal, Vol. 25, No. 3, March 1987, pp. 401-407.

Raffel, M. and Kompenhans, J., (1993), “PIV Measurements of Unsteady Transonic Flow Fields above a NACA 0012 Airfoil,” SPIE Vol. 2052, Laser Anemometry Advances and Applications, 1993, pp. 527-534.

Rizzetta, D. P. and Visbal, M. R., (2002), "Application of Large-Eddy Simulation to Supersonic Compression Ramps", AIAA Journal, Vol. 40, No. 8, August 2002, pp.1574-1581.

Rizzetta, D. P., Visbal, M. R. and Gaitonde, D. V., (2001), "Large-Eddy Simulation of Supersonic Compression-Ramp Flow by High-Order Method", AIAA Journal, Vol. 39, No. 12 December 2001, pp. 2283-2291.

Samimy, M., and Lele, S.K., (1991), “Motion of Particles with Inertia in a Compressible Free Shear Layer,” Physics of Fluids A, Vol. 3, No. 8, August 1991, pp. 1915-1923.

Samimy, M., and Wernet, M. P., (2000), “Review of Planar Multiple-Component Velocimetry in High-Speed Flows,” AIAA Journal, Vol. 38, 2000, pp. 553-574.

Selig, Michael. S., (1988), "Unsteadiness of Shock Wave/Turbulent Boundary Layer Interactions With Dynamic Control", Master Thesis, Princeton University, School of Engineering and Applied Science, Department of Mechanical and Aerospace Engineering.

Selig, M. S., Andreopoulos, J., Muck, K. C., Dussauge, J. P. and Smits, A. J., (1989), "Turbulence Structure In a Shock Wave / Turbulent Boundary - Layer Interaction", AIAA Journal, Vol. 27, pp. 862-869.

Selig, M. S., and Smits, A. J., (1991), "Effect of Periodic Blowing on Attached and Separated Supersonic Turbulent Boundary Layers," AIAA Journal, Vol. 29, No. 10, October 1991, pp. 1651-1658.

Settles, G. S., Vas, I. E., and Bogdonoff, S. M., (1976), "Details of a Shock-Separated Turbulent Boundary Layer at a Compression Comer," AIAA Journal, Vol. 14, No. 12, pp. 1709-1715, December 1976.

Settles, G. S., Fitzpatrick, T. J., and Bogdonoff, S. M., (1979), "Detailed Study of Attached and Separated Compression Corner Flowfields in High Reynolds Number Supersonic Flow," AIAA Journal, Vol. 17, No. 6, June 1979, pp. 579-585.

Settles, G. S. and Dolling, D. S., (1992), "Swept Shock-Wave/Boundary Layer Interactions", in *Tactical Missile Aerodynamics*: General Topics, AIAA Progress in Astronautics and Aeronautics, Vol. 14 1, 1992, pp. 505-574.

Smith, D. R. and Smits, A. J., (1993), "Simultaneous Measurement of Velocity and Temperature Fluctuations in the Boundary Layer of a Supersonic Flow", Experimental thermal and fluid science, October 1993, pp. 221-229.

Smits, A. J. and Dussauge, J. P., (1996), "Turbulent Shear Layers in Supersonic Flow", American Institute of Physics, ISBN 1-56396-260-8.

Smits, A. J., and Muck, K. C., (1987), "Experimental Study of Three Shock Wave Turbulent Boundary Layer Interactions," Journal of Fluid Mechanics, Vol. 182, pp. 291-314, 1987.

Smits, A. J., Spina, E. F., Alving, A. E., Smith., R. W., Fernando, E. M. and Donovan, J. F., (1989), "A Comparison of the Turbulence Structure of Subsonic and Supersonic Boundary Layers", Physics of Fluids A, Vol. 1, November 1989, pp. 1865-1875.

So, R. M. C., Gatski, T. B. and Sommer, T. P., (1998), "Morkovin Hypothesis and the Modeling of Wall-Bounded Compressible Turbulent Flows", AIAA Journal, Vol. 36, No. 9, September 1998, pp. 1583.

Spina, E. F. and Smits, A. J., (1987), "Organized Structures In A Compressible Turbulent Boundary Layer", Journal of Fluid Mechanics, Vol. 182, 1987, pp. 85-109.

Spina, E. F., Smits, A. J. and Robinson, S. K., (1994), “The Physics Of Supersonic Turbulent Boundary Layers”, Annual Review of Fluid Mechanics, Vol. 26, 1994, pp. 287-319.

Sun, C. C. and Childs, M. E., (1973), "A Modified Wall Wake Velocity Profile For Turbulent Compressible Boundary Layers", Journal of Aircraft, Vol. 10, No. 6, June 1973, pp. 381-383.

Sun, C. C. and Childs, M. E., (1976), "Wall-Wake Velocity Profile for Compressible Nonadiabatic Flows", AIAA Journal, Vol. 14, No. 6, June 1976, pp. 820-822.

Ünalmis, Ö.H., (1995), "Structure of Supersonic Boundary Layer and Its Influence on Unsteady Separation," PhD dissertation, Department of

Aerospace Engineering and Engineering Mechanics, The University of Texas at Austin.

Ünalmis, Ö.H., and Dolling, D.S., (1994), "Decay of Wall Pressure Field and Structure of a Mach 5 Adiabatic Turbulent Boundary Layer", AIAA Paper 94-2363, June 1994.

Unalmis, O. H., and Dolling, D. S., (1998), "Experimental Study of Causes of Unsteadiness of Shock-Induced Turbulent Separation" AIAA Journal, Vol. 36, No. 3, 1998, pp. 371-378.

Ünalmis, Ö. H., and Dolling, D. S., (1999), "Decay of Fluctuating Wall-Pressure Field of Mach 5 Turbulent Boundary Layer," *AIAA Journal*, Vol. 37, No. 9, Sep. 1999, pp. 1088-1096.

Ünalmis, Ö. H., Hou, Y. X., Bueno, P. C., Clemens, N. T., and Dolling, D. S., (2000), "PIV Investigation of Role of Boundary Layer Velocity Fluctuations in Unsteady Shock-Induced Separation", AIAA paper 2000-2450, June 19-22, 2000.

Urbin, G., Knight, D., and Zheltovodov, A. A., (1999), “Compressible Large Eddy Simulation using Unstructured Grid: Supersonic Turbulent Boundary Layer and Compression Corner”, AIAA paper 99-0427, Jan. 1999.

Urban, W. D., (1999), "Planar velocity measurements in compressible mixing layers", PhD dissertation, Mechanical Engineering Department, Stanford University.

Urban, W. D., and Mungal, M. G., (2001), "Planar velocity measurements in compressible mixing layers", J. Fluid Mech., Vol. 431, 2001, pp. 189-222.

Van Driest, E. R., (1956), "The Problem of Aerodynamic Heating", Aero. Engrg. Rev., Vol. 15, no. 10, 1956, pp. 26-41.

Viswanath, P. R., (1988), "Shock-Wave-Turbulent-Boundary-Layer Interaction And Its Control: A Survey of Recent Development", Sādhanā, Indian Academy of Sciences, Proceedings in Engineering Sciences, Vol. 12, pp. 45-104.

Westerweel, J., Dabiri, D., and Gharib, M., (1997), “The Effect of a Discrete Window Offset on the Accuracy of Cross-Correlation Analysis of Digital PIV Recordings,” Experiments in Fluids, Vol. 23, 1997, pp. 20-28.

Westerweel, J., (1997), “Fundamentals of Digital Particle Image Velocimetry”, Measurement Science Technology, Vol. 8, pp. 1379-1392, 1997.

Westerweel, J., (2000), “Theoretical Analysis Of The Measurement Precision In Particle Image Velocimetry”, Exp. Fluids, Vol. 29, s3-2s12.

White, F. M., (1991), "Viscous Fluid Flow", McGraw-Hill, Inc., ISBN 0-07-069712-4, pp. 550- 554.

White, F. M. and Christoph, G. H., (1972), "A Simple Theory for the Two-Dimensional Compressible Turbulent Boundary Layer", J. Basic Engrg., Vol. 94, 1972, pp. 636-642.

Wu, P and Miles, R.B., (2000), "MHz Rate Visualization of Separation Shock Wave Structure", AIAA Paper 2000-0647, Jan. 2000.

Wu, P. F., Lempert, W. R., and Miles, R. B., (2000), “Megahertz pulse-burst laser and visualization of shock-wave/boundary-layer interaction”, AIAA Journal, Vol. 38, No. 4, April 2000, pp672-679.

Yanta, W. J. and Lee, R. E., (1976), "Measurements of Mach 3 Turbulence Transport Properties on a Nozzle Wall", AIAA Journal, Vol. 14, No. 6, June 1976, pp. 725-729.

Vita

Yongxi Hou was born in XinKai, JiGuanShan, FengCheng, LiaoNing, P. R., China, on April 10, 1971, the son of Zhuogui Hou and Youmei Geng. He received the degree of Bachelor of Science from BeiHang University (BHU), Beijing, P.R.China in August 1994 and the degree of Master of Science from Nanyang Technological University (NTU), Singapore in August 1998. In January 1999 he entered the Graduate School of The University of Texas.

Permanent address: XinKai, JiGuanShan, FengCheng, LiaoNing, P. R. China, 118100

This dissertation was typed by the author.